POLITECNICO DI MILANO

Department of Chemistry, Materials and Chemical Engineering

Master Degree in Materials Engineering and Nanotechnology

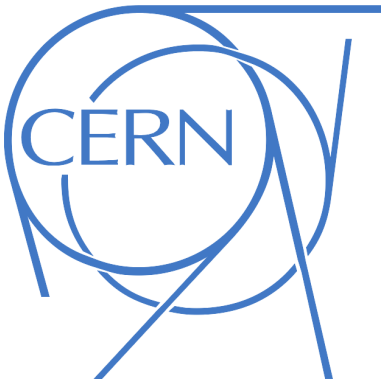

Experimental Investigation on the Electron Multipacting and the Surface Conditioning

Advisor: Massimiliano Bestetti
CERN Advisor: Mauro Taborelli

Amedeo Bellunato
Id:783670

Academic Year 2012-2013

Acknowledgments

This work is entirely dedicated to my mother, Emma, and my sister, Bianca.
Your efforts were crucial to reach this goal and won't be forgotten.
Afterwards, I would like to thanks all my friends and all the people who crossed my path during the last years and which supported me.
I would like to start from my best friends since ever: Tommaso and Whighes, probably we are not so close as before, and probably our lives will take everyday more different directions, but every time I meet you is like we have always been together.
It is fundamental to mention even Poly, Umbe, Bajes and Perri, you've been the best companions for many adventures and I can't avoid to smile whenever I think about the time spent with you.
A special remark goes to Seba and Paola: your courage in completely renewing your life, more than once, has been an inspiration for me.
I can't proceed before saying many thanks to others of my closest friends: Alby, Alessia, Luca and Raffo, you have been strong supporters of me and I love you.
Starting from the first year of university I've met many special people: Roby, Gabri and Dami, it looks like we are getting lost, but the last experience with Damiano taught me the world is small, and it's only a matter of time before we will get in touch again.
Now I can move forward to those who are the most recent friends I learnt to know, a special "thank you" goes to Giammi, Gianma, Mauro, Amani, Miriam, Sara, Marta, Lucia, Giulia and Luca, these are not all those who I am grateful to, but are those who mostly represented the funniest side of my university studies and which I will miss most thinking about the Politecnico.
Then, it is crucial to cite all my training mates and my master, often you've been the only thing I had to save my mental health.
Lastly, I would like to thank all my "CERN FRIENDS".
A brand-new, entire acknowledgments chapter would be necessary to thank you all, you've been so many and we lived so many adventures in the last year that is unfair to be constrained in few lines.
The most special remark goes to Riccardo and Elena, Marco, Damiano, Carlo, Passere', Gully, Giulio, Chiara, Tessa, Merolone, Nico, Alessandro and Dario, if the CERN experience has been so incredible it's only because of you, we built a special group and we've been very lucky to meet each other.
To conclude, I would like to thank my beloved Giulia: I would have never managed to do this without your love and dedication to us.

Abstract

The beam induced electron cloud build-up is one the major limitations for the high luminosity project of the CERN LHC (Large Hadron Collider).
The most relevant problems concerning the electron cloud inside accelerators cavities are the pressure rises, the heat loads and the beam instabilities.
The multipacting is an RF resonant electron discharge sustained by secondary electrons emission.
Inside particles accelerators, the self-field associated to the particles beam develops the resonance conditions for the cascade generation of secondary electrons.
The tendency of an accelerator cavity toward the multipacting is ruled by the beam parameters, the presence of a magnetic field and the SEY (Secondary Electron Yield, δ) of its surfaces.
In order to achieve the targets of the High-Luminosity and LHC-Injectors-Upgrade projects, it is required a reduction of the secondary yield of the beam-pipes surfaces.
A specific task within the Injector Upgrade program is the SEY reduction of the Super Proton Synchrotron MBB bending sections below the value $\delta_{max} < 1.3$.
The SEY can be reduced by surface modifications as the increased roughness, the thin films coatings and the beam scrubbing.
The amorphous carbon coatings appear to be the most promising solution for the unbaked magnetized sections of the SPS (either MBB and MBA), with an SEY$\simeq 1$.
The beam scrubbing (or beam conditioning), instead, uses the beam induced multipacting to bombard the beam-pipes surfaces with energetic electrons coming from the electron cloud.
These electrons scrub the surfaces by two main processes: the Electron Stimulated Desorption of the adsorbates, and the surface graphitization.
The combination of these two effects reduces significantly the tendency of a surface toward the multipacting, as observed during the beam scrubbing runs in the SPS with the $50ns$ beam.
The present work focuses mainly on these thematics: the influence of the magnetic field intensity on the multipacting tendency inside MBA and MBB cavities, and the possibilities of the beam scrubbing in reducing the surface SEY and, consequently, in suppressing the electron cloud development inside an RF cavity.
Two RF test-benches have been built using MBB or MBA dipole chambers crossed by a W wire, they work as coaxial resonators.
The wire is connected to an RF power supply to develop the electric field which ignites the multipacting, simulating the conditions induced by the particles beams inside the accelerators.

The multipacting is detected by the ESD pressure peaks and the perturbation of the RF resonance modes.
Moreover, one of the set-up is provided of an electron cloud monitor to measure the electron cloud current.
The multipacting intensity is correlated to the SEY of the surfaces inside the resonators.
The test-benches are automatized in order to stimulate the multipacting with a defined rate for long periods of time.
The prolonged electron bombardment is used to study the surface conditioning as a consequence of the high exposure to scrubbing electrons.
Furthermore, one of the systems has a leak valve for the injection of hydrocarbon gases.
The aim of the hydrocarbon contamination is to achieve an accelerated surface graphitization and SEY reduction, Acetyelene or Dodecane have been used.
Lastly, $a - C$ coated chambers are investigated in order to study the efficiency of low SEY surfaces in suppressing the multipacting.

Estratto

Una delle maggiori limitazioni per gli esperimenti di fisica ad alta energia nel CERN Large Hadron Collider é rappresentata dalla formazione di una densitá spaziale di elettroni causata dal passaggio di un fascio di particelle.
Questo fenomeno prende il nome di nube elettronica o electron cloud (e-cloud).
Le conseguenze piú rilevanti in un acceleratore riguardano l'aumento di pressione, il surriscaldamento e le instabilitá del fascio.
Il multipacting é una scarica elettronica in condizioni di risonanza sostenuta tramite emissione secondaria di elettroni.
Il campo elettromagnetico autoaggiunto di un fascio di particelle causa l'instaurarsi delle condizioni di risonanza per la generazione a cascata di elettroni secondari e, conseguentemente, lo sviluppo dell'electron cloud.
La propensione di una cavitá acceleratrice a stimolare multipacting il é regolata dai parametri del fascio, dalla presenza di un campo magnetico e dall'efficienza di emissione di secondari dalle superfici, SEY (Secondary Electron Yield, δ).
Per raggiungere gli obiettivi proposti dai progetti di alta luminositá (High-Luminosity) e di aggiornamento degli iniettori (LHC-Injectors-Upgrade), é necessario ridurre l'efficienza di emissione di secondari delle superfici nelle cavitá acceleratrici.
Nell'ambito dell'upgrade degli iniettori, uno degli obiettivi specifici é il raggiungimento della condizione $\delta_{max} < 1.3$ nelle cavitá MBB dei dipoli del Super Proton Synchrotron.
Il secondary electron yield puó esserre ridotto tramite trattamenti superficiali quali: l'aumento della rugositá, l'applicazione di film sottili ed il beam scrubbing.
Per quanto riguarda i film sottili, i rivestimenti di carbonio amorfo sembrano la soluzione piú promettente per le sezioni non riscaldabili del SPS (sia nelle cavitá MBA che MBB), raggiungendo un $SEY \simeq 1$.
Il beam scrubbing (o beam conditioning), invece, sfrutta il multipacting indotto dal fascio per bombardare le superfici delle cavitá acceleratrici con gli elettroni energetici provenienti dall'e-cloud.
Questi elettroni compiono un'operazione di scrubbing della superficie attraverso due meccanismi: il desorbimento elettrostimolato degli adsorbati (Electron Stimulated Desorption), e la deposizione di un layer grafitico.
La combinazione di questi processi riduce drasticamente la propensione di una supericie a sviluppare il multipacting, come giá osservato durante le prove di beam scrubbing nel SPS con fasci a $50ns$.
Questo lavoro si concentra principalmente sulle seguenti tematiche: l'influenza dell'intensitá del campo magnetico sul multipacting a paritá di SEY, e l'efficacia del beam scrubbing nel ridurre il δ di una cavitá acceleratrice.

A tal fine, sono stati costruiti due banchi di prova che funzionano come risonatori in radiofrequenza.
Questi ultimi sono ottenuti installando un cavo di tungsteno, W, in posizione coassiale alle cavitá dei dipoli MBB ed MBA.
Il cavo di tungsteno é alimentato da un generatore di potenza in radiofrequenza con l'obiettivo di sviluppare il campo elettrico necessario per stimolare il multipacting.
Il fine é la simulazione delle condizioni indotte dal fascio di particelle all'interno del Super Proton Synchrotron.
All'interno del risonatore, il multipacting viene monitorato attraverso i picchi di pressione indotti tramite ESD e le perturbazioni indotte sui modi di risonanza del sistema.
Inoltre, un electron cloud monitor é installato su uno dei banchi di prova per misurare la corrente indotta dalla nube elettronica.
L'intensitá del multipacting viene utilizzata come misura indiretta dell'efficienza di emissione di secondari nelle superfici del risonatore.
Entrambi gli apparati sperimentali possono essere automatizzati per stimolare il multipacting ad una certa cadenza per lunghi intervalli di tempo.
Il prolungato bombardamento elettronico ha la finalitá di studiare il conditioning di una superficie come conseguenza di una lunga esposizione agli elettroni di scrubbing.
In aggiunta, uno dei sistemi ha una linea di iniezione per gas idrocarburi.
La contaminazione con gas organici durante il multipacting ha la finalitá di accelerare la deposizione del layer grafitico e la riduzione del secondary electron yield, Acetilene e Dodecano sono stati utilizzati a tal fine.
Su entrambi i banchi di prova sono stati eseguiti dei test su camere rivestite con film di carbonio amorfo per studiare l'efficacia di una superficie a basso SEY nell'inibizione del multipacting.

Contents

List of Figures

List of Tables

I wanted you to see what real courage is, instead of getting the idea that courage is a man with a gun in his hand.
It's when you know you're licked before you begin, but you begin anyway and see it through no matter what.
You rarely win, but sometimes you do.

Nelle Harper Lee

Chapter 1

Introduction

The European Organization for Nuclear Research, CERN, developed a complex accelerators scheme which contains the world's largest particle accelerator: the Large Hadron Collider, LHC.
The LHC is a proton-proton collider designed to run particle beams in ultrahigh vacuum with energy up to $7TeV$.
The LHC is a $27km$ ring of superconducting magnets and accelerating structures. The particles travel inside two ultrahigh vacuum pipes and are driven by superconducting magnets kept at superconducting temperature in the order of few K degrees.
Its pipes cross each other at four points along the circuit, where the largest experiments are located: LHCb, Alice, Atlas and CMS.
Protons are separated from H atoms and travel through the LINear ACcelerator (LINAC2) and the Proton Synchrotron Booster (PS Booster), they are then injected from the Proton Synchrotron (PS) to the Super Proton Synchrotron (SPS) and lastly reach the inlet of the LHC.
During the experimental physics runs, the beams are driven to collision at the four experiments' areas, where the particles resulting from the high energy impacts are detected.
The analysis of the particles tracks lead to significant discovers, the most important concerning the Higgs' boson.
The probability, σ, of each collision to produce a physics relevant event is extremely low.
It means that a huge number of impacts is required to improve the possibilities of detecting relevant phenomena.
The final probability rate of a physics event is defined as $R = L\sigma$, where $L[cm^{-2}s^{-1}]$ is the Luminosity [39].
A particle beam is divided into batches which are further split into a series proton packages, or bunches, of density N_b.
The luminosity is proportional to the bunch density: $L \propto N_b^2 F(\nu_{bb})$, the forecast for the nominal LHC design is $L = 1.0 * 10^{-34} cm^{-2}s^{-1}$.
To gain this result, it is required to provide proton bunches in the order of $N_b \simeq 1.3 * 10^{11} protons/bunch$, $25ns$ spaced at a nominal energy of $7TeV$ [56].
Furthermore, the High Luminosity project for LHC has been started. It has the ambition of pushing forward the nominal design performances of the LHC and to

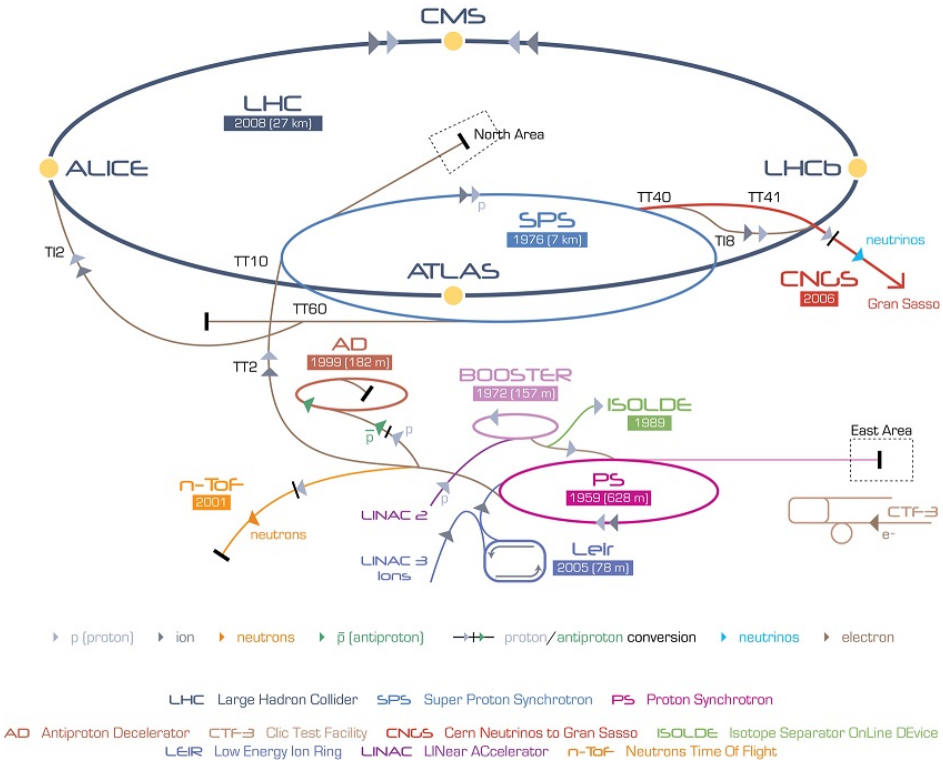

Figure 1.1: CERN Accelerators Complex

reach the goal of $L \simeq 5 * 10^{34} cm^{-2} s^{-1}$ within the 2020, with an operative life of the LHC expected to 2030.
The expected luminosity increase requires even an upgrade of the injectors complex. Starting from this requirement, CERN developed the LHC-Injectors Upgrade program: LIU.
Among the challenges of the luminosity upgrade, the electron multipacting is one of the major limitations to overcome in high energy accelerators, as the SPS and LHC.
The multipacting is a cascade generation of secondary electrons.
It is a surface process, since the emission of secondary electrons happens in the first nm of the emitting material.
Historically, the multipacting was firstly described in 1934 by Farnsworth, the word derives from "resonance of multiple electrons impact" [39].
The discovery of an electron cloud inside a particle accelerator, instead, happened in 1965 in a small proton ring in Russia, at CERN the first observations of an electron cloud development date back to 1972 inside the ISR, Intersecting Storage Ring.
Nowadays, the multipacting inside the SPS accelerator is one of the main limitations toward the high luminosity target.
Inside an accelerator, the particle beam trajectory is constrained along the ring through magnetic bending sections. The curvature of the beam trajectory causes an acceleration of the charged particles which emit a synchrotron radiation.
The radiation strength can be enough to ionize either the residual gas molecules

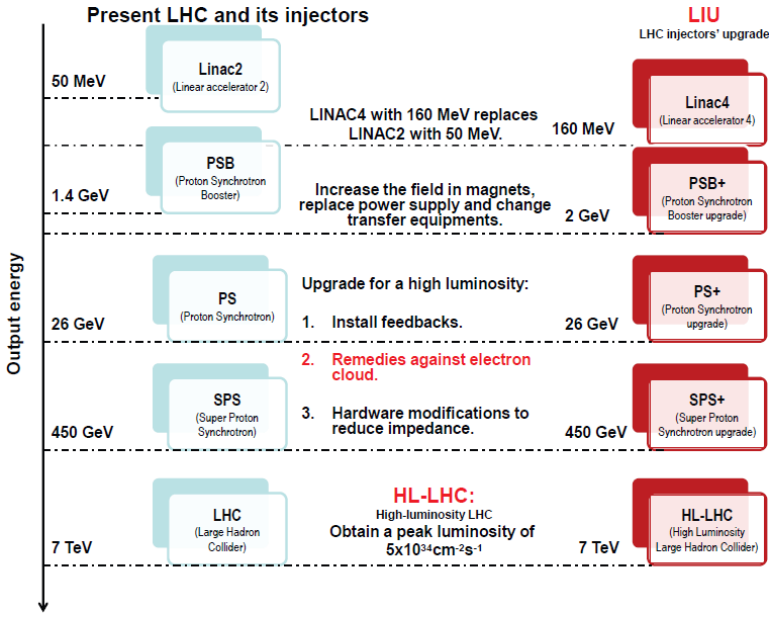

Figure 1.2: CERN LIU and HL-LHC [56]

inside the beam-pipe and the pipes' walls.
Furthermore, the residual gas molecules are affected by a second ionization mechanism: the molecules-beam collisions.
The combination of these ionization processes provides the first electrons (the seeds) for the multipacting ignition.
The collective behavior of a proton bunch is like a charged mass that runs through the beam-pipe: it emits an electric field, the self-field.
Protons are positively charged particles, it means that the self-field of a bunch is directed outwards.
Any electron that undergoes this field is accelerated by the bunch along the field lines, according the equation $\vec{F} = -e\vec{E}$.
The bunch passage accelerates the electrons which travel across the beam-pipe and hit its surfaces, the energy transfer upon impact provokes the surface emission of secondary electrons.

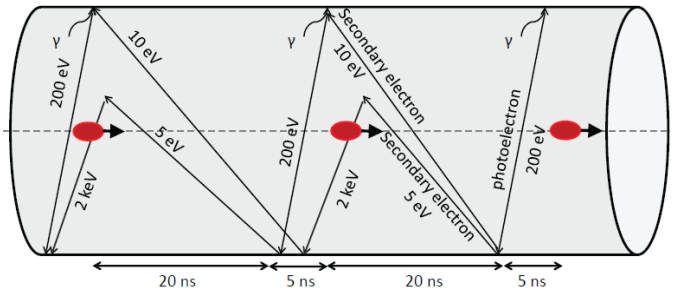

Figure 1.3: Electron cloud build up inside an LHC beam-pipe due to photo-emission [9].

As the next bunch passes, its self-field accelerates the electrons in the pipe and leads to the production of new secondaries: it is the beginning of the cascade generation of secondary electrons.
It leads to the formation of an electron cloud inside the pipe: an electron space density.
It affects the accelerators' performances either interacting with the particle beam and the beam-pipes.
The electrostatic interaction of an electron cloud with a proton bunch leads to beam instabilities and beam losses.
Moreover, the electrons impingement against the accelerator cavity provokes a local heat load. Any heat transfer in correspondence of cryogenic surfaces can induce a loss of the super-conductive properties of the bending dipoles and the interruption of their working conditions.
Lastly, the electrons impingement releases adsorbates from the pipes surfaces via ESD, Electron Stimulated Desorption.
The ESD results in the vacuum break-down which strongly affects the performances of an accelerator.
The probability of inducing multipacting inside an accelerator is dependent on three main conditions: the beam parameters, the vacuum quality and the pipes' surface status.
The beam is the principal source of energy to start the electron multipacting, since the bunch intensity is directly proportional to the self-field strength.
The bunch frequency, as well, is a key parameter for the cascade generation: if the beam frequency is low enough, the electrons are lost between each bunch and the cascade doesn't start.
The vacuum quality regulates the generation of the seeds for the multipacting, less residual gas molecules imply less ionizations events.
The role of the surface lays in its SEY, Secondary Electron Yield.
An high SEY surface has a strong probability of emitting secondary electrons. A $\delta_{max} > 1$ implies that, on the average, the surface is able to emit more than one secondary per impinging electron.
The present work focuses on the secondary emission properties of a surface.
Any metallic surface is provided of its specific SEY, usually greater than unity.
Surfaces inside accelerators are "technical surfaces" which undergo air exposure before the installation and are provided of an adsorption layer of several species which, in the case of Stainless Steel, $StSt$, are able to increase its SEY up to around two.
Among the several techniques available to reduce the secondary yield of a Stainless Steel surface, this work deals with two classes of intervention: the surface conditioning and the thin films.
Experiments show that a Stainless Steel pipe exposed to the particle beam undergoes a reduction of its SEY via the so called beam scrubbing.
It is the combination of two mechanisms which modify the surface status: the ESD and the conditioning by means of the surface graphitiazion.
The first process, as told above, removes the adsorbates leading to the cleaning of the surface, which gains its original SEY without the influence of the adsorption layer.

Further, the surface graphitization builds an amorphous graphite thin layer which reduces the SEY. The amorphous carbon has a yield almost equal to unity.
The scrubbing efficiency determines the beam ability in reducing the multipacting. More in detail, the graphitization degree regulates the SEY reduction of the surface.
The experiments performed during the present work study the conditioning of *StSt* surfaces exposed to multipacting and the effect of the introduction of hydrocarbon gases on the graphitization degree of the surface.
The aim is to determine the efficiency of the multipacting in conditioning a surface up to $\delta_{max} < 1,3$ or completely suppressing the multipacting.
Lastly, the results obtained on the Stainless Steel surfaces will be compared to those obtained on carbon coated chambers.
The experimental work focuses mainly on the conditioning possibilities of the uncoated *StSt* SPS bending sections.
Since these chambers can't be baked, thin films like NEG can't be applied and the only possibility to suppress the multipacting seems to be the carbon coatings.
The goal is to verify the conditioning efficiency of the electron cloud and the chances of the beam conditioning as an alternative solution to suppress the multipacting inside the accelerators cavities.

Chapter 2

The Secondary Electron Yield

When an electrically charged particle, with enough kinetic energy, strikes the surface of a solid body, the latter can emit electrons.
Those electrons are defined as "Secondary".
If the impinging particles are electrons themselves, these are known as "Primary".
Historically this effect was discovered by Austin and Starke in the 1922 [7], starting from their studies on the reflection of cathodic rays against a metal surface, they noticed the electrons coming from the target were higher in number than the bombarding ones.
It was the proof that primaries are able to extract other electrons, the secondaries, from the target.

2.1 Fundamentals

A particle that travels through a medium looses its energy along its path, the energy loss per unit path length is known as the stopping power $S = -\frac{1}{\rho}\frac{dE}{dx}$.
Several mechanisms are involved, the main contribution is the collisional term between the traveling particle and the medium atoms. It is referred to as LET, Linear Energy Transfer.
Neglecting the possibility of induced nuclear reactions, the second contributor is the emission of radiation, respectively Cerenkov and Bremsstrahlung radiations [33].
The Bremsstrahlung radiation represents the emission associated to the fast acceleration of a charged particle induced by its electrostatic interaction with the protons and the electrons of the surrounding matter.
The Cerenkov effect is typical of charged particles that, inside certain media, are able to travel faster than light.
It is worth to say that, according to the relativistic physics, any particle can't travel faster than light in vacuum, but it is possible inside a medium where the propagation of light is ruled by its refraction index $v_{light} = \frac{c}{n}$, where n is the refraction index of the medium and c the speed of light.
The motion of the fast charged particle induces the formation of temporary dipoles between the electrons and protons of the body that, relaxing, emits radiation.

The stopping power, then, can be divided in two terms:

$$S = S_{collisional} + S_{radiation} = \frac{-1}{\rho}\frac{dE}{dx} \tag{2.1}$$

Considering the case of a primary electron beam bombarding a solid surface, with energy below 10MeV, the collisional term is predominant and leads to a simplified equation for the stopping power that neglects the radiative component [19].

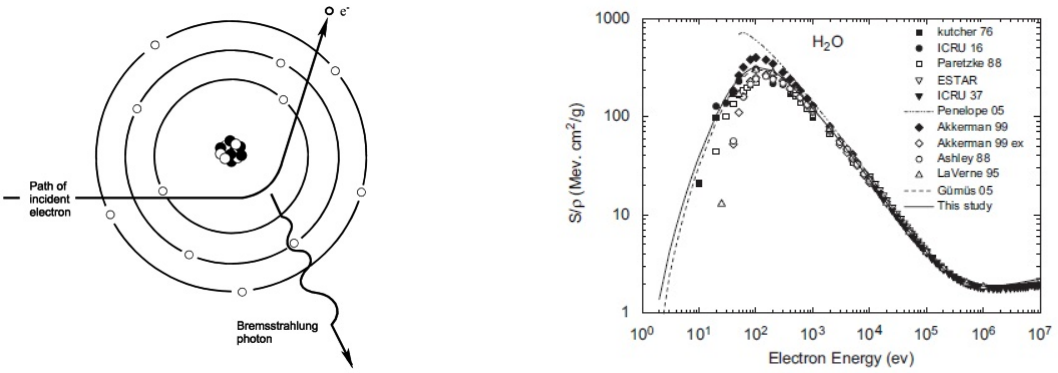

(a) Bremsstrahlung

(b) Stopping Power

Figure 2.1: Left: a representation of the Bremsstrahlung emission model. Right: the comparison of the Stopping power between different evaluation models [19].

A consequence of the collisions between the primaries and the target is the generation of secondary electrons, which are generally considered as all the electrons emitted from the surface of the body.
There are four principal classes of secondary electrons:

- True Secondary Electrons: the collisional energy transfer between the primaries and the atoms of the target is enough to ionize the material.
  Generally all those electrons with energy below 50eV are classified as true secondaries.

- Inelastically Backscattered Electrons: are primary electrons which undergo inelastic collisions that reverse their direction toward the surface.
  The energy loss during an inelastic collision can be enough to ionize the atom and extract a further electron.

- Elastically Backscattered Electrons: are those which undergo elastic diffusion processes until they're reflected toward the surface.
  Are those few electrons which manage to escape the surface with the same energy of the primaries.

- Auger Electrons: an atom ionization leaves an unfilled state in its electronic shell, it can induce a further electron emission by means of the Auger effect.
  The Auger electrons are those extracted from an atom thanks to the energy given by the relaxation of another electron of its atomic shell from an higher

to a lower energy level.
The kinetic energy of the emitted Auger electron is equal to the difference between the one received from the relaxation process and its ionization energy, $E_k = \Delta E_{relax.} - E_{ion}$.

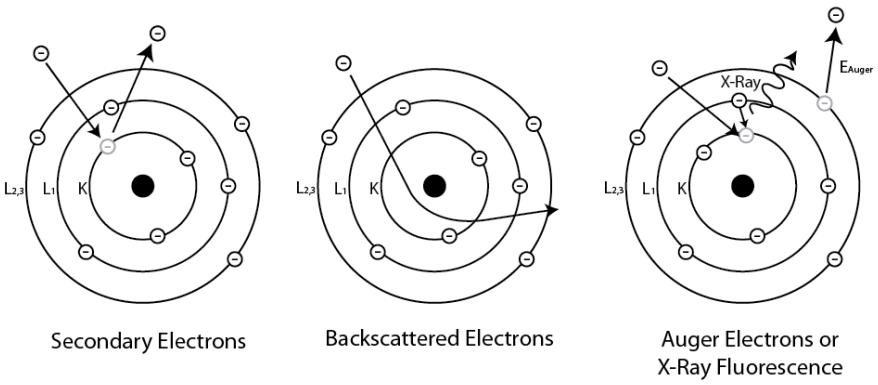

Figure 2.2: Secondaries generation processes [16]

To define these categories it was necessary to study the numerical and energetic distributions of the electrons emitted by a surface.
The combination of a retarding potential V_{ret} and of hemispherical electrostatic lenses allows to define how many electrons escape the target with energy between E and $E + dE$ and to design the secondaries energy distribution [48], figure 2.3.

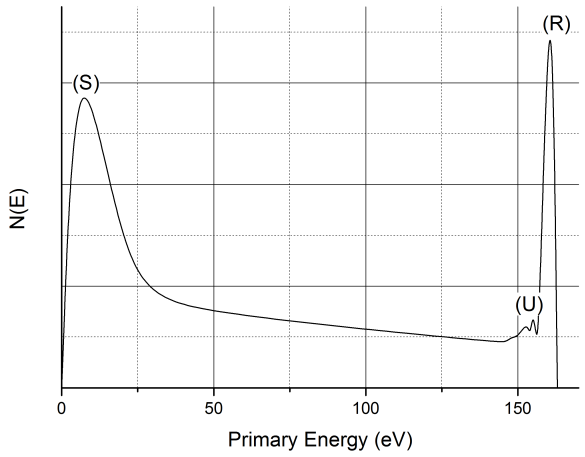

Figure 2.3: Secondary electrons energy distribution [7].

As any charged particle, even the secondaries traveling trough a body loose their energy. Since they are less energetic than the primaries it implies they can travel shorter distances before getting adsorbed.
Monte-Carlo simulations provide the statistical description for the primary path

inside a body and the depth of generation of the different species of secondaries.
The secondaries generation energy determines their escaping depth, highly energy electrons can travel longer through the medium.
The average escaping distances vary from few Å to few nm for the most energetic electrons, as the elastically backscattered secondaries, figure 2.4.

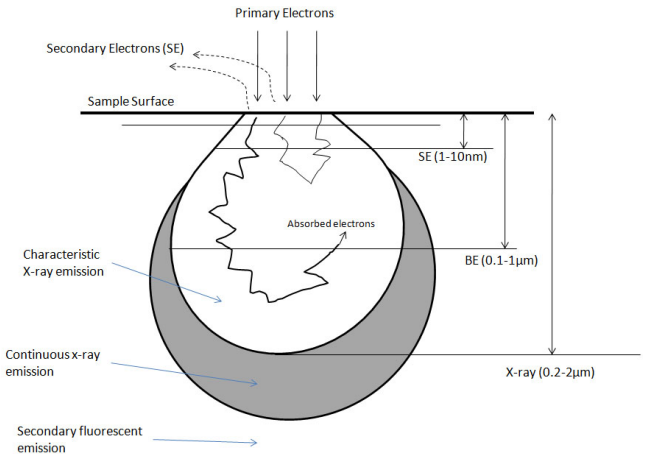

Figure 2.4: Secondary electrons generation depth

When a primary electron strikes a target body, the ratio between the amount of incident electrons and the emitted ones is defined as Secondary Electron Yield, δ.

$$\delta = \frac{i_{emitted}}{i_{primary}} \tag{2.2}$$

Considering this relation the secondaries are defined as the total amount of electrons coming from the surface, without any distinction.
The factor δ defines the primaries efficiency in extracting electrons from the target surface.
It is possible to describe the energy transfer from the incoming primaries either by means of the classic physics and by quantum mechanics.
In the Drude-Sommerfeld theory of conduction, a metal is described as an ordered lattice of atoms surrounded by an "ideal gas of free and non-interacting" electrons of conduction. The valence electrons, instead, are bounded around the lattice atoms' positions.
A primary electron that travels through the target is supposed to interact only with the lattice and excite the valence electrons, its energy loss through the material is assumed [4, 7, 15, 48]:

$$E^n(X) = E_0^n - Anx \tag{2.3}$$

Where A is a constant of the material.
The amount of secondaries generated by the passage of a primary is defined as $n(x)$

and is proportional to the primary energy loss along its path through the material and to the average energy required to produce a secondary electron, ϵ.

$$n(x, E) = -\frac{1}{\epsilon}\frac{dE}{dx} \tag{2.4}$$

Once a bunch of secondaries is produced, it is worth to take into account that part of them will be lost along their run toward the surface, for sake of simplicity their adsorption is considered as an exponential function of the depth.
Lastly, those secondaries which reach the edge of the body are required to overcome the work-function ϕ of the surface, so part of them will be reflected into the material and absorbed.
It implies that each secondary has an escape probability $f(x)$ which reduces exponentially with the generation depth x.

$$f(x) = Be^{-\frac{x}{\lambda}} \tag{2.5}$$

Where $B < 1$ implies that at any generation depth the escape probability is always less than 1.
The secondary electron yield becomes:

$$\delta = \int n(x, E)f(x)dx \tag{2.6}$$

The total SEY has to be evaluated between the surface edge and the maximum penetration depth, d, of primaries at energy E.
The maximum penetration depth is reached when $E = 0$.

$$d = \frac{E_0^n}{An} \tag{2.7}$$

A further approximation considers the amount of produced secondaries as constant per unit path through the material:

$$n(x, E_0) = -\frac{1}{\epsilon}\frac{E_0}{d} \tag{2.8}$$

Introducing equations 2.3 and 2.7 in 2.6 results:

$$\delta = -(\frac{B}{\epsilon})\int_0^d (An)^{\frac{1}{n}} d^{\frac{1-n}{n}} e^{-\frac{x}{\lambda}} dx \tag{2.9}$$

The closed form solution is:

$$\delta = -\frac{B}{\epsilon}(An)^{\frac{1}{}}(\frac{d}{\lambda})^{\frac{(1-n}{n)}}(1 - e^{-\frac{x}{\lambda}}) \tag{2.10}$$

The final equation for the SEY is strictly dependent on the material and its constants.
Along the years several different approximations were introduced to estimate the SEY curve of metals, starting from the work of Bruining to the more recent papers of Dekker and Seiler.
Pictures 2.5 and 2.6 show the improvements related to the corrections introduced

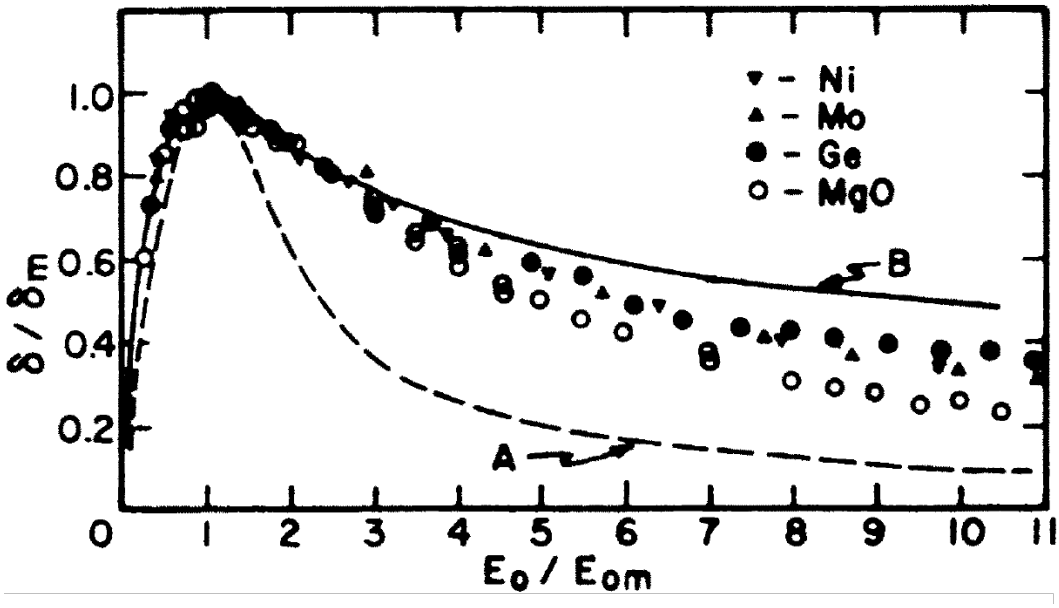

Figure 2.5: The picture compares the experimental results for the SEY with the models of Baroody, dashed line, and Dekker, continuous line [15].

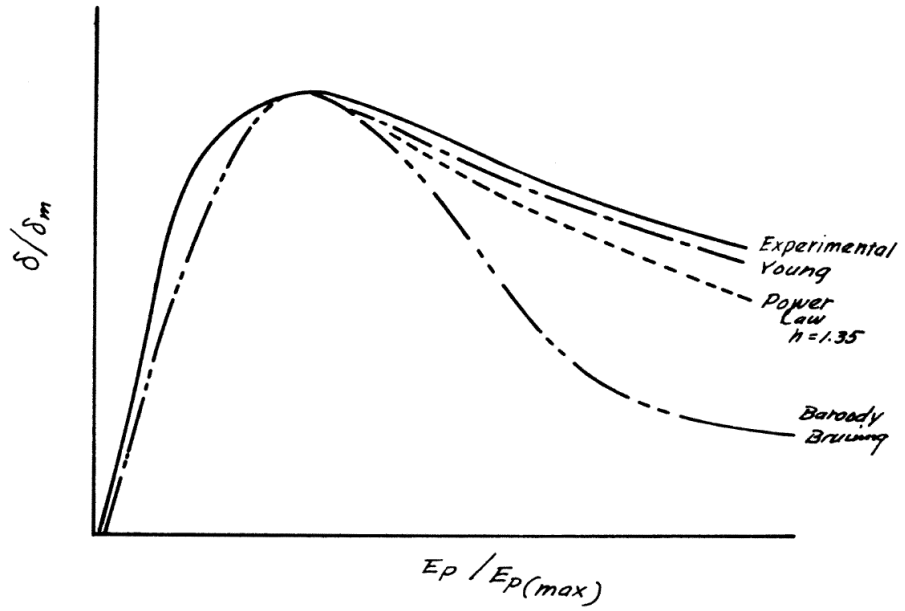

Figure 2.6: The picture compares the experimental results with the different theoretical models proposed along the years for the secondary electron emission [8].

by Young, who added the scattering effect of the primary electrons inside the material [8].
The second possibility to evaluate the interaction between charged particles and matter is the quantum mechanics approach. The mathematical formalism explains all the possible channels of energy loss of the particles and correlates the further secondary generation efficiency directly to the stopping power of the material.
A first approximation uses the Bethe formula that is one of the most famous models for particles interaction with matter, it won't be discussed since it is not valid for the primary electrons, but rather for fast heavy charged particles.
The nature of the interactions between the primaries and the lattice electrons complicates the model that has to take into account the same mass of the incoming particles and the electrons of the lattice structure, it implies more difficulties in the application of a perturbative model.
Modified versions of the original formula exist, as the one proposed by Gumus for primary electrons [19]. For practical reasons this work considers the general validity of the classical model to provide a simplified understanding of the generation of secondary electrons.

2.2 SEY Measurement

A charged particles beam is focused on a target surface to stimulate the emission of secondary electrons. Practically a sample is bombarded by a primary electrons beam to measure its SEY, the value of δ_{max} is of primary relevance to determine the tendency of a material in developing an electron cloud.
The measurement scheme consists of an electron gun able to provide PE, Primary Electrons, in a range from few eV to some keV focused along the normal to the surface of the sample, figure 2.7.
The sample is negatively biased in the order of $-10V$ to $-20V$ to repel all the emitted secondary electrons. Aside of the target is placed a positively biased collector, about $+50V$, able to catch all the electrons impinging on it [50].
The two currents a recorded simultaneously by mean of amplifiers :

- I_s, between the sample and the ground.
- I_c, between the collector and the ground.

The total secondary electron current is defined without any distinction between the secondary classes, equation 2.11.

$$\delta = \frac{I_s}{I_p} = \frac{I_s}{I_s + I_c} \tag{2.11}$$

The amount of PE that strike the surface determine the accumulated electron dose, it means the number of electrons per unit surface that the target receives expressed as $D[\frac{C}{mm^2}]$. It is of primary importance to control the exposure of the target to the primary electrons, since they affects the δ_{max} inducing surface chemical modifications.

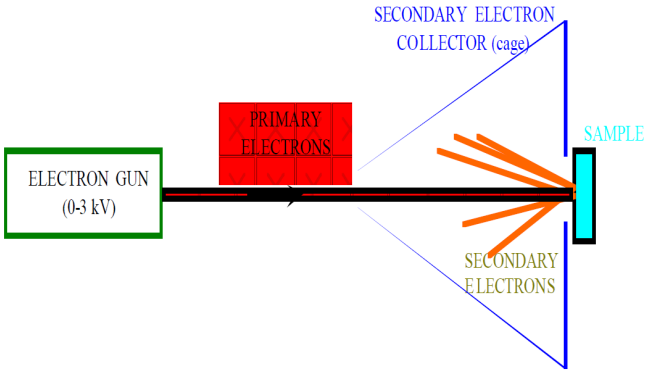

Figure 2.7: SEY Measurement Scheme [3].

2.3 SEY of a technical material

The status of a surface determines the SEY of the specimen, the simple air exposure till the hydrocarbons contamination can influence the chemical composition of the surface modifying its secondary emissivity.
For this reason it is worth to introduce the term of "technical materials" to define those components different from the ideal and laboratory samples.
Technical surfaces are provided of a non-ideal roughness and their composition is modified by the interaction with the environment.

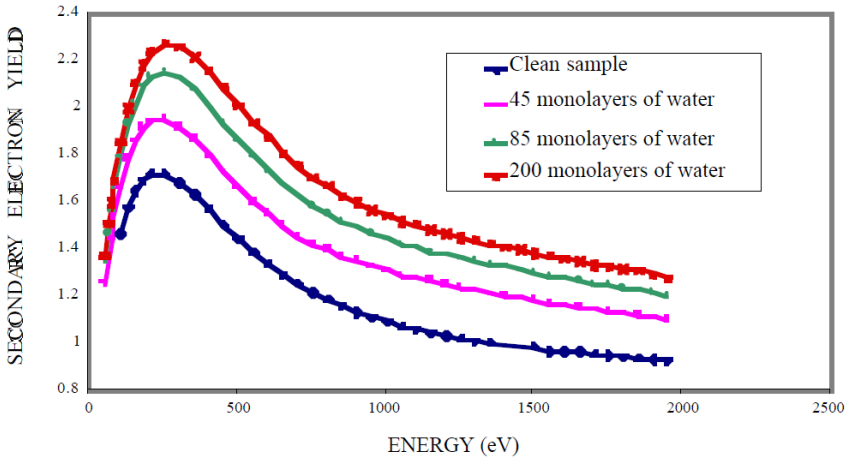

Figure 2.8: Variation of the SEY as a function of the adsorbed water and the PE energy of Copper [3].

An interesting example is the variation of the secondary electron yield of Cu as a function of the adsorbed water layers, as shown in figure 2.8.
The SEY variation of a surface can be firstly ascribed to its variation in the work function, a decrease of ϕ means the electrons require less energy to overcome the potential difference between the edge of the material and the environment, it implies that even those low energy secondaries generated far from the surface are able to escape.

As a result the peak of maximum emission, δ_{max}, shifts to higher E_{PE} along the secondary yield curve.
Another mechanism to modify the SEY is the formation of an adsorbed layer on the surface of the material.
In the latter case the superficial layer thickness regulates the δ_{max} variation. If the adsorbates layer is thick enough, it becomes the only responsible of the secondaries generation.
Reducing its height it increases the probability of electrons to escape from the substrate: the resulting SEY would be an intermediate between the SEY of substrate and of the adsorbates layer.
A pure metal has an high surface energy, γ_s, and once is exposed to a reactive environment the tendency is to reduce it.
In the common practice, it is necessary to consider the exposure to air.
The first immediate reaction is the formation of a $Me{-}Oxide$ layer with a thickness that is usually higher than the escape depth of the electrons of the pure material.
The presence of H_2O and organic contaminants leads to the formation of a first hydroxide compound by reaction with water.
Further, the organic contaminants will deposit on the first oxide layer and will trap water molecules by hydrogen bonds.
Generally, the SEY of a metal exposed to air is considered to increase. To know the influence on its SEY it is necessary to consider the composition of the contamination.
For the $Me - Oxides$ is necessary to distinguish between insulator and semiconductor oxides, the firsts have a great escape distance and a high SEY, the seconds show often a lower SEY as in the case of the CuO_2 [47].
A semiconductor oxide has a lower yield than the pure metal, but once exposed to air its δ_{max} increases as a consequence of the environmental contamination layer.
An "as received" surface is generally provided of a contamination layer which δ_{max} is modified proportionally to the layer thickness.
In the latter case the resulting SEY is affected by the contribution of either the contamination layer and the clean surface. Experimentally the resulting SEY is achieved, but it is impossible to distinguish between the two contribution terms.
The contamination layer suffers the temperature variations.
Increasing the temperature, the molecules adsorbed on the surface are thermally excited and desorb: the SEY is influenced by the contaminants, and so by the temperature and the exposure time, figure 2.9.

2.4 Surface electron conditioning

The properties of a technical metal material are affected, even, by the primary electrons bombardment.
The superficial oxide and contamination layers interact with the energetic primaries and change the chemical composition of the surface.
A possible consequence is the SEY reduction.
The technique that uses an electron beam to reduce the SEY of a surface is known as "electron conditioning" or "electron scrubbing" [30].

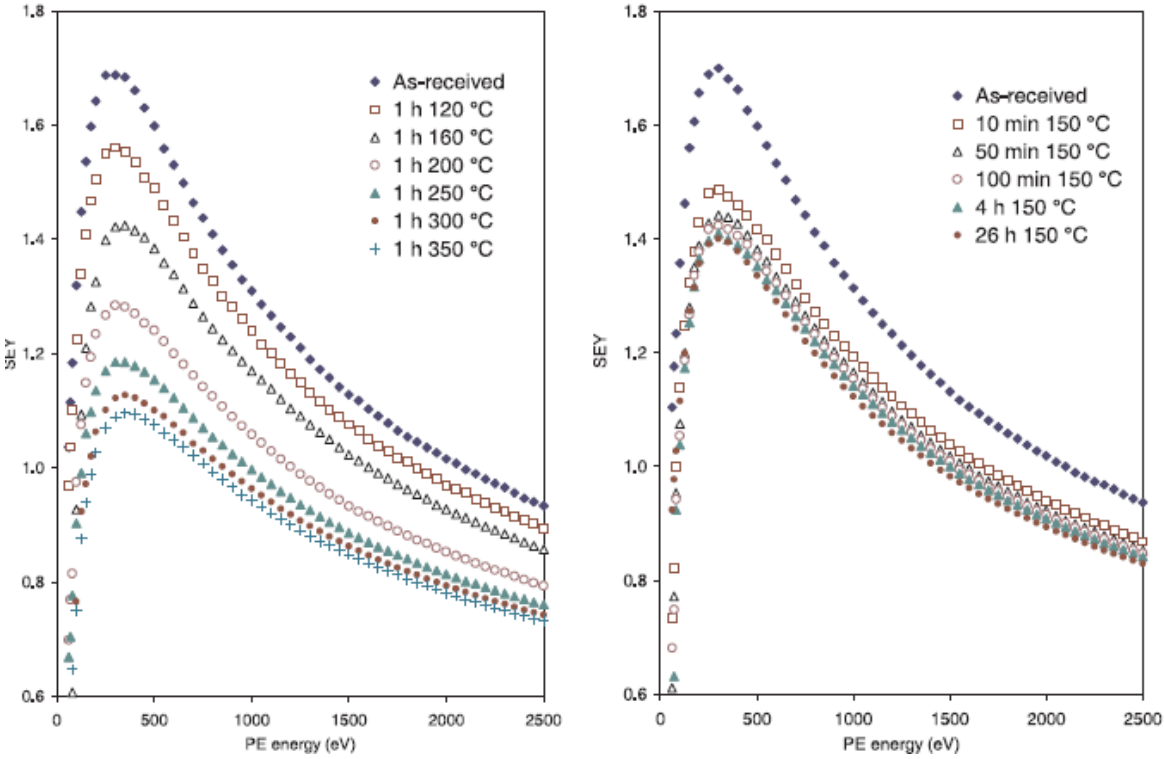

Figure 2.9: SEY as function of the heating T [47].

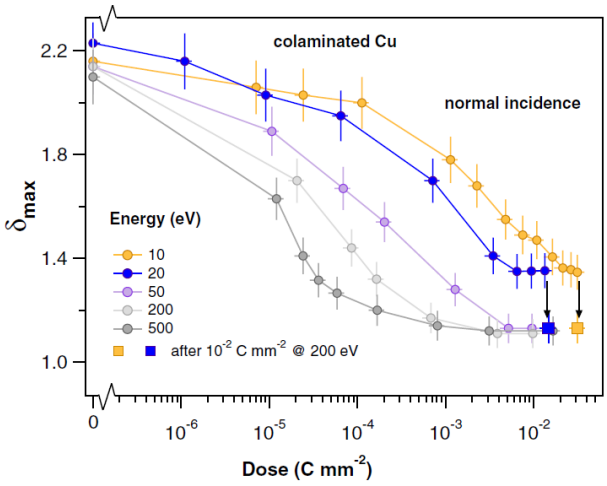

Figure 2.10: δ_{max} as a function of the dose for different impinging electron energies at normal incidence on colaminated Cu of the LHC beam screen [30].

The reduction of the yield is a function of the cumulative dose and the energy of the electrons, less energetic primaries are less effective in the surface modifications of the sample and require an higher dose, figure 2.10.

2.4.1 Electron stimulated desorption

Energetic electrons may provoke the gas molecules desorption from the surface of the target.
The energy transfer induces the adsorbed molecule to gain a repulsive excited state and a certain probability of escaping from the surface before relaxing.
The qualitative theory able to give a simple understanding of this phenomenon is the Menzel-Gomer-Redhead model.
The theory proposes a desorption model via a Frank-Condon electronic transition, the result is the achievement of a repulsive state.
The main difference with the gas phase electron stimulated reactions are the numerous decaying channels available to relax the excitation energy thanks to the presence of the substrate.
The model considers a single bonding level between the molecule and the substrate, it avoids to consider any further energetic variation induced by the substrate excitation. It assumes the relaxation to imply a re-adsorption if the quenching time is faster than the kinetic energy gain of the excited molecule.
According to this model, the escaping yield is directly proportional to the excitation cross-section times the probability not to activate a fast quenching mechanism.

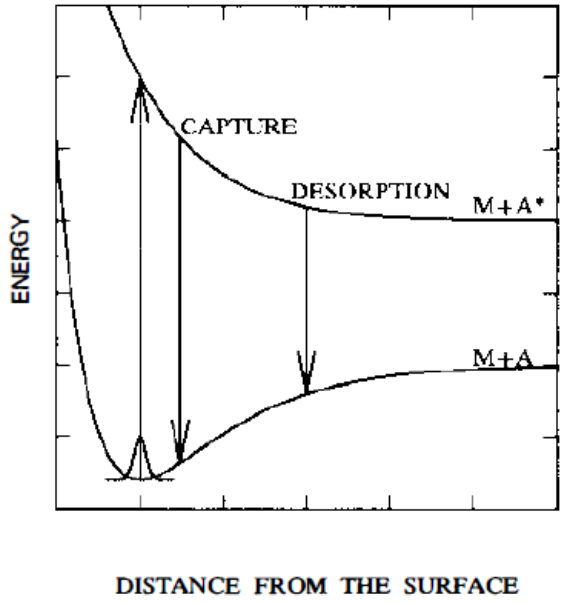

Figure 2.11: M-G-R model: scheme of desorption [2].

As shown in figure 2.11 the desorption along the excited energy level is possible only in absence of any quenching mechanism.
The nature of the repulsive state is not specified in the model and is possible to release either neutrals or ions.

The process involves the target electrons through valence electrons excitations or ionizations, the first is the less effective mechanism and releases neutrals.
The second mechanism is usually the most probable and can release either ions or neutrals, in principle the ionized state corresponds to a repulsive energetic level, but for physisorbed molecules it is, instead, an attractive configuration.
The desorption happens only if the molecule keeps enough kinetic energy after its neutralization.
Actually, Antoniewicz evidenced this latter mechanism is not possible through a single ionization process but requires multiple ionizations [2].
Once an electron strikes the surface it is able to free only those molecules to which can provide enough energy to allow the energetic jump between the ground and the excited states.
Are defined: σ_{d,E_0} the surface coverage of the molecules that can be liberated by an electron impinging with energy E_0, Q the total desorption cross section, J the electronic current density and e the elementary charge.
The desorption rate becomes [41]:

$$-\frac{d\sigma_d}{dt} = \frac{\sigma_d Q J}{e} \tag{2.12}$$

When multipacting develops inside a vacuum chamber the pressure of the system rises, ESD is one of the most relevant factors in the pressure increase, figure 2.12.

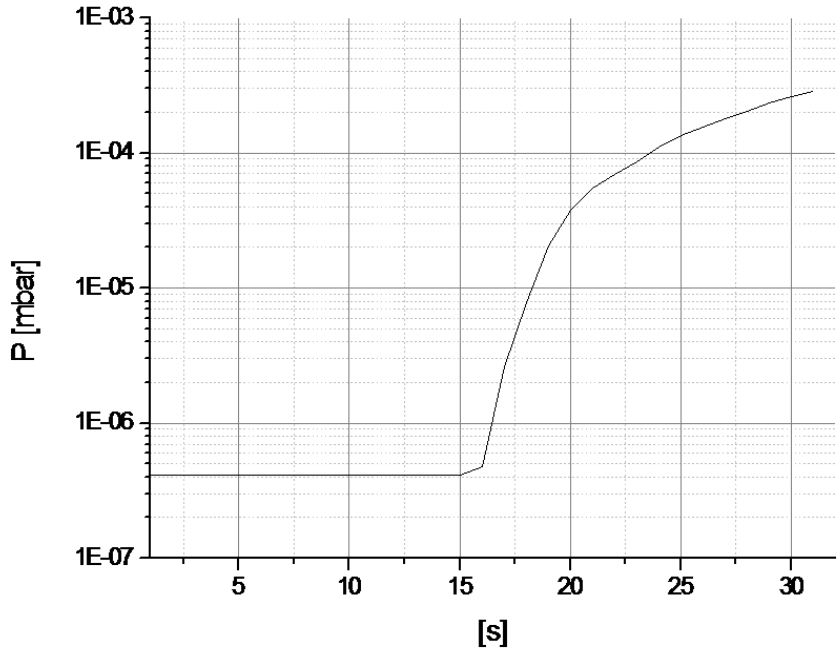

Figure 2.12: Pressure rise during induced multipacting

Integrating the equation it is possible to find the molecules coverage decrease in

time, $\theta_{\sigma_d}(t)$, proportional to the pressure rise in the vacuum chamber.

$$\theta_{\sigma_d} = e^{-\frac{tJQ}{e}} \tag{2.13}$$

It should be necessary to consider even the re-adsorptions, they can slow down the ESD till an equilibrium is reached between the species that leave the surface and those that stick on it.
The result is a surface cleaning from the adsorption layer, which is reflected in a variation of the SEY toward the real value of the uncontaminated surface.

2.4.2 Graphitic film growth

The second possible effect of the electron bombardment of technical materials is the graphitic film growth.
The origin of the carbon source for the film growth is not fully clear.
Technical surfaces are covered by organic species that, once exposed to the electron irradiation, tend to partially decompose and rearrange in a graphitic like structure.
As a consequence this process is well known in all the environments where surfaces contaminated by organic molecules are irradiated by high energy electrons, like microscopy, litography and synchrotron beam lines.
In the cases above the organic molecules are heavy hydrocarbons from the residual gas.
On the other hand the graphitization is observed even on sputter-cleaned surfaces uncovered of heavy organic contaminants.
The residual gas dissociation is not enough to justify the large amount of carbon graphitization on the surface.
The first attempts to explain the film growth consider the dissociation of the $C-H$ and $C-O$ bonds of the adsorbates. It induces the formation of volatiles which leave the surface, in the meanwhile part of the C atoms left rearrange in $C-C$ bonds with the typical honeycomb structure of the graphite, due to the transition from the sp^3 to the sp^2 hybridization state [30], figure 2.14.
Figure 2.13 shows how the final SEY of a conditioned Cu surface results to be independent of the residual gas composition: it allows to assume the source for the carbon film growth is even the surface material itself.
The graphite is one of the possible allotropic states of carbon, the amorphous graphite is made of an high ratio of sp^2/sp^3 hybridized atoms. It has a layered, planar structure connected by strong intra-layers σ bonds and weak Van Der Waals attraction forces across layers.
The π orbitals can weakly bond to the first neighbor atoms [43].
The most recent studies on these process use a focused electron beam to induce the graphitization of the sample surface [12, 30, 50], the efficiency is strictly related to the energy of the primary electrons.
A surface is fully scrubbed once its SEY doesn't reduce further under the exposure of the primary electrons, it means that reached a cumulative dose above which the graphitization becomes ineffective.
There are two different energy regions for scrubbing: it is possible to distinguish between the scrubbing ascribed to the electrons with energy below $20eV$ or above

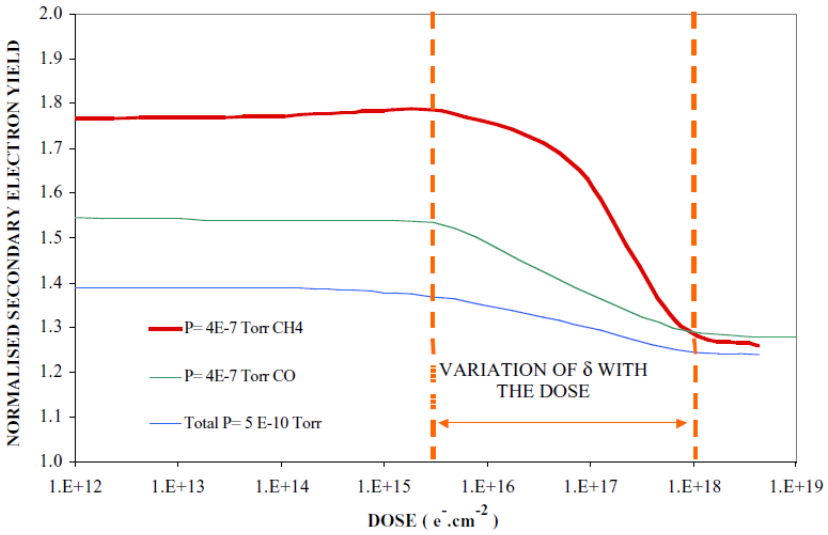

Figure 2.13: SEY variation with electron dose and different residual gas compositions [20].

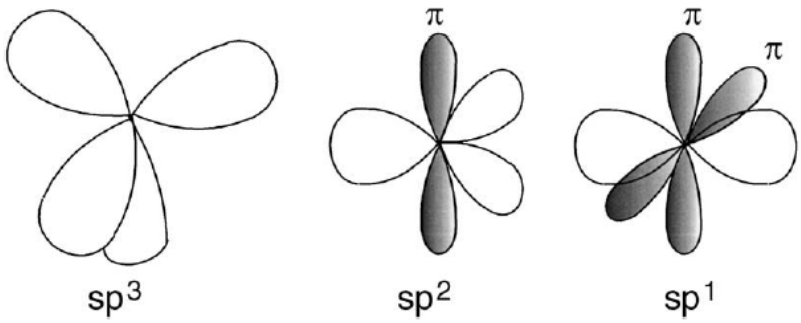

Figure 2.14: C atoms hybridization orbitals. the white orbitals are the σ, the black ones the π [43].

$50eV$.
In the first case, the maximum SEY that can be reached is $\delta_{max} = 1.35$ after a long beam exposure, this value can be further reduced only if the sample afterwards is irradiated by electrons with energy above $200eV$, at least.
For the specimen treated with energies above $50eV$ the minimum SEY is $\delta_{max} = 1.1$, the dose required to reach this level decreases in a way proportionally inverse to the electrons energy [12, 30].

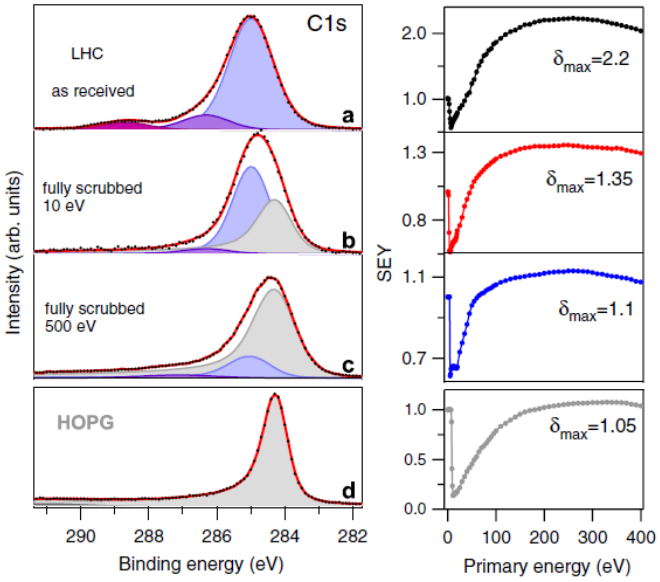

Figure 2.15: C 1s XPS spectra and SEY curves measured on the LHC Cu sample: (a) as received, (b) after a dose of $3 * 10^2$ C/mm^2 at $10eV$, (c) after a dose of $3 * 10^2$ C/mm^2 at $500eV$, and (d) on a freshly cleaved HOPG surface [12].

The characterization of the sample surface status and composition is obtained acquiring the XPS spectra during the scrubbing.
As shown in the left part of the picture 2.15, the scrubbing induces a shift of the $C1S$ core levels to lower binding energies, characteristic of the sp^2 hybridization.
Going forward with the scrubbing, the relative composition of the $C1S$ peak is moved in favor of an higher percentage of graphite atoms on the surface.
When the specimen is fully scrubbed, it is possible to notice that, where a lower SEY is reached, the component of the $C1S$ peak at a binding energy of $284.3eV$ is higher.
For low energy electrons, the fully scrubbed surfaces show the lowest percentage of sp^2 conversion and, consequently, the lowest degree of graphitization with a $C1S$ peak still rich in the $285.1eV$ $C1_{sp^3}$ component.
In addiction, the XPS plot of the fully scrubbed surface lacks of the the $288.1eV$ weaker peak characteristic of the $C - H$ and $C - O$ bonds [30].
It is necessary to underline that exists an exception to the validity of the electron scrubbing: air exposed Al shows an increase of the SEY after the beam scrubbing and has no evidences of any graphite film growth, the behavior is ascribed to the high O reactivity to form alumina, Al_2O_3 [12].

The data coming from Stainless Steel, Cu and TiN show that the graphitic film growth could be the main process behind the δ_{max} reduction through scrubbing, whenever the energy of the electrons is greater than a certain threshold defined by the minimum desired secondary yield. For the the SPS bending sections it is desired a $\delta_{max} < 1.3$, for this purpose are required electrons above $20eV$.

Chapter 3

The e-Cloud

The exposure of a surface to an oscillating electro-magnetic field can provoke a cascade generation of electrons: the multipacting.
The RF field accelerates the primary electrons against the surface and if its SEY is greater than one, the electrons number increases by secondary emission and starts the cascade generation. The key parameter of the multipacting is the δ_{max} of the surface.
The ensemble of electrons coming from the surface at each field oscillation contributes to build up an electron cloud: the e-cloud, EC.

3.1 e-Cloud build-up in particle accelerators

High energy accelerators generate charged particles beams that run inside their beampipes, the passage of particles bunches creates the oscillating field which accelerates the primary electrons (the seeds for the multipacting) against the pipes walls.
This phenomenon is stronger in positively charged particle accelerators consisting of protons and positrons [9], where the generation of the first electrons happens mainly by means of two processes:

- Synchrotron radiation stimulated electron photoemission.
- Ionization of the residual gas molecules.

The particles in the accelerators are grouped in bunches, or packages, and separated by an interval of time which defines the frequency of the oscillating field that accelerates the electrons: the self-field.
The particles of the first bunch hit the residual gas molecules causing ionizations which add electrons to those already present in the system, generated by the synchrotron radiation and the cosmic rays.
Then, the bunch self-field accelerates the electrons against the surface of the pipe that releases secondary electrons, if the frequency of the bunches is fast enough these secondaries can be accelerated once again increasing their number, few bunches are sufficient to start the cascade process and the e-cloud development.

At CERN the e-cloud build up is a relevant problem for the expected runs with bunches at $50ns$ and $25ns$ and full working intensities either in the LHC, Large Hadron Collider, and in the SPS, Super Proton Synchrotron.
First of all, inside an accelerator the multipacting is associated to an ESD induced pressure rise that reduces the vacuum quality of the pipes.
Vacuum is required to maintain the beam shape and stability.
Any pressure increase results in the diffraction of the beam particles that hit the gas molecules, close to the detectors it can give a background to the relevant proton-proton collisions.
Moreover, the collisional induced ionizations provide further electrons to expand the cloud.

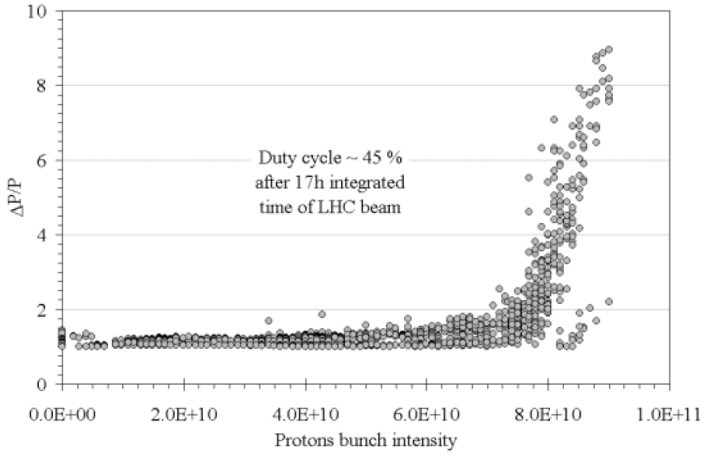

(a) Field free region

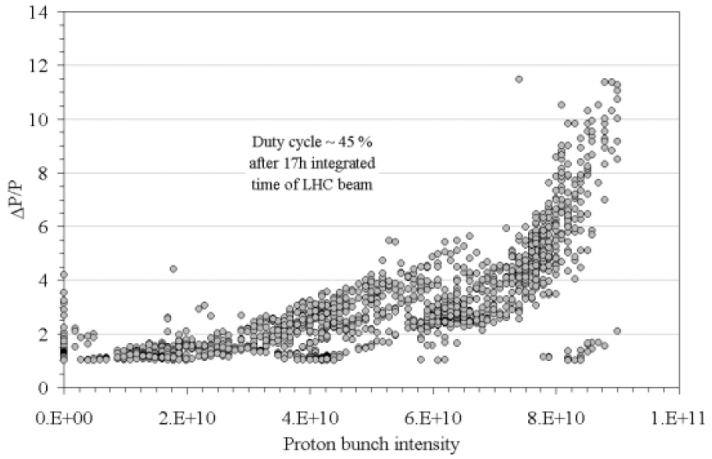

(b) Field region

Figure 3.1: Pressure rise induced by the multipacting [1]. Left: outside the field region. Right: inside the field region.

The uncontrolled development of the electrons number continues until the space charge limits arise, in these conditions the combined effect of the ESD and the electrical interaction between the high electron charge density and the beam particle brings to a catastrophic loss of the beam [39].

Lastly, both the electrons and the gas molecules striking the surfaces exchange energy with the pipe walls leading to an heat load.
On the cryogenic sections of the LHC magnets it induces a shift from a superconductive condition to a normal-conductive one, it implies the loss of the bending properties of the magnets that are no more able to keep the trajectory of the beam.
Figure 3.1 shows the pressure rise due to the ESD in two different sections of the SPS, the pressure development and the intensity threshold for the multipacting in function of the bunch intensity are different between field free and field-filled regions, this mismatch is due to the effect of the magnetic field, $\vec{B}$, on the trajectories of the electrons.
The Lorentz force $\vec{F_L} = q(\vec{E} + \vec{v} \times \vec{B})$ constrains an electron to travel along the electric field direction and around the magnetic field lines on circular orbits.
The time an electron requires to travel around its orbital is the cyclotron frequency, an AC electric field $E(\nu)$ will provide the highest acceleration to the particle if it's combined to a magnetic field of value $B(\nu)$ [52].

$$|B(\nu)| = \frac{\nu 2\pi m}{q} \tag{3.1}$$

Where ν is the frequency of the electric field.
The energy gain induced by the cyclotron condition results in a more effective multipacting, hence the bunch intensity threshold for its activation is lower in a dipole section [57].
A set of basic equations can derive the threshold conditions which the beam must fulfill to induce the multipacting.
The simplest model considers a magnetic field free, straight, circular pipe. The electric field of the beam is:

$$E(r) = \frac{\lambda}{2\pi\epsilon_0 r} = \frac{eN_b}{c\tau}\frac{1}{2\pi\epsilon_0 r} \tag{3.2}$$

Where λ is the line charge induced by a bunch of N_b particles and long $c\tau$, with c as the speed of light.
The momentum transfer Δp to an electron of charge $e^- is$:

$$\Delta p = eE(r)\tau = \frac{e^2 N_b}{2\pi\epsilon_0 cr} \tag{3.3}$$

Introducing the classical definition of electron radius $r_e = \frac{1}{4\pi\epsilon 0 r^2}\frac{e^2}{m_e c}$ in 3.3, it is derived the velocity increment of the electron as:

$$\Delta v = 2cr_e\frac{N_b}{r} \tag{3.4}$$

The kicked electron must cross the pipe's radius, r_p, in synchronism with the bunch passage and before the next, positively charged, bunch coming.

$$\frac{\Delta v}{2r_p} < \nu_{bb} \tag{3.5}$$

The number of particles in a bunch to start the multipacting is directly proportional to the bunch frequency ν_{bb} and r_p [18].

$$N_b = \frac{r_p^2 \nu_{bb}}{r_e c} \tag{3.6}$$

Equation 3.5 is the first condition for the beam induced multipacting. The second condition requires the accelerated electrons to extract secondaries during the impingement against the surface.
In conclusion, once the beam parameters are defined, the e-cloud builds up only if $\delta_{max} > \delta_{th.}$, where $\delta_{th.}$ is an SEY threshold dependent on the beam characteristics, the geometry of the beam pipe and the field value in the magnetic sections.
So, in the CERN accelerators complex the SEY requirements at the nominal intensity $25ns$ beam vary according to the pipe materials, the geometry of the sections and the magnetic field.
For the LHC , in the field free, straight sections the multipacting is avoided for $\delta_{max} < 1.4$ [39].
The e-cloud is a serious problem especially in the SPS where it can limit the characteristics of the bunches and affect the maximum luminosity of the LHC.
The SPS is made of vacuum chambers that compose the straight field free sections and the field filled bending ones, figure 3.2.

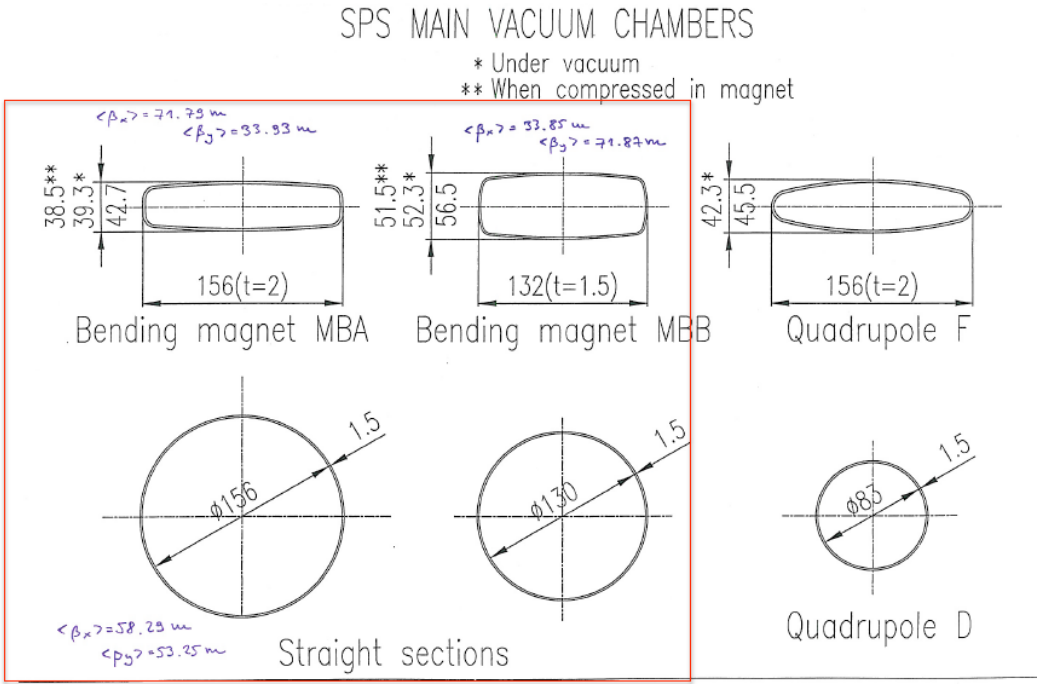

Figure 3.2: SPS pipe sections [46].

Simulations give a threshold for multipacting $\delta_{max} < 1.5$, for either the straight sections and the MBA chambers. It results lower in the MBB where the condition to avoid the e-cloud build up is $\delta_{max} < 1.3$ [46].

3.2 Mitigation

Since the LHC requires the highest luminosity as possible, it means that even the beam frequency and its intensity must be the highest as well.
To reach this goal, it is necessary to reduce the electron-cloud development without affecting the beam parameters.
For this reason, it is of primary importance to reduce the SEY of the beam pipes. The emission of secondary electrons is a surface mechanism, to reduce the yield there are several surface treatments that operate according to different principles. A low SEY material is the starting point of each technique.
Pure metal materials have generally a low yield, figure 3.3, technical surfaces increase their SEY because of air exposure and working processes. Concerning the environmental contamination, it is necessary to underline that often technical materials of the same specie have different initial SEY for the same exposure time to air.
An example can be the clean Cu that increases its δ_{max} from 1.2 to 2 for air exposure lasting respectively few minutes and few days [47].

Element	δ_{max}	$V_{p(max)}$	*Fig. No.*	*Ref.*
Ag	1·5	800	3.1	137
Al	1·0	300	3.2	167
Au	1·46	750	3.3	137
B	1·2	150	3.4	298
Ba	0·83	400	3.5	167
Bi	1·15	550	3.6	262
Be	0·53	200	3.7	167
C	1·0	300	3.8	171
Cd	1·1	400	3.9	284
Co	1·2	700	3.10	213
Cs	0·72	400	3.11	167
Cu	1·3	600	3.12	137
Fe	1·3	350	3.13	137
Ge	1·2	400	3.14	298
K	0·75	200	3.15	144
Li	0·5	85	3.16	167
Mg	0·95	300	3.17	167
Mo	1·25	375	3.18	137
Nb	1·2	375	3.19	137
Ni	1·3	550	3.20	137
Pb	1·1	500	3.21	262
Pd	>1·3*	>250*	3.22	41
Pt	1·8	800	3.23	83
Rb	0·9	350	3.24	144
Si	1·1	250	3.25	298
Sn	1·35	500	3.26	262
Ti	0·9	280	3.27	170
W	1·4	700	3.28	51
Zr	1·1	350	3.29	170

* $\delta = 1{\cdot}3$ at $V_p = 250$ V is not maximum value of δ.

Figure 3.3: SEY of pure metals [7].

It is important even to notice that a low work-function doesn't correspond to the highest δ_{max}. That's not in fully accordance with the classic theory of secondary emission, actually ϕ seems to play a secondary role with respect other physical properties, in particular the density [7].

3.3 The effect of the surface structure

A rough surface has a lower SEY than a smooth one. The principle that lays at the basis of this difference is the re-adsorption of secondary electrons in complex structures.

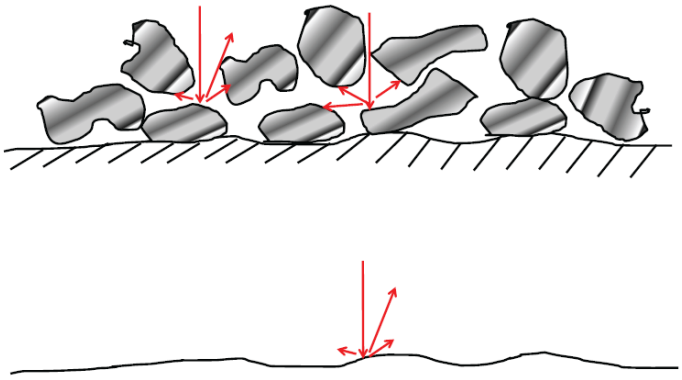

Figure 3.4: Secondary electrons escape trajectories from a rough surface [59].

.

When a primary impinges on a surfaces, it emits secondary electrons which probability of crossing again another section of material is proportional to their emission angle, figure 3.4.
A secondary can be re-adsorbed when hits the surface roughness or generates other secondaries, known as "second-generation secondaries" [40], going further on the "higher-generation secondaries" their energy reduces each step until the re-adsorption of the emitted electrons.
The SEY of a smooth surface is higher since an emitted electron has an almost null probability of crossing again the material and being adsorbed.

3.3.1 Grooved surfaces

Triangular and rectangular grooved surfaces were studied, the probability of re-adsorption is determined by the secondaries emission angle and by the number of emitted secondaries in function of the primaries incidence angle. The sharpness of a groove affects the SEY: rounded edges corresponds to an higher average SEY [40].
Grooves were studied at CERN on Cu and $StSt$ samples, the first difficulty met was the hardness of the stainless steel which limited the grooves sharpness.
Al samples where produced at SLAC and investigated at CERN, in all cases the measured SEY appeared higher than the measured threshold for the SPS applications [40, 56]. The presence of a magnetic field deflects the motion of the elctrons, figure 3.5, and should further reduce the yield of the grooved surface [58].
The experimental results in the dipole sections of the SPS show a reduction of the multipacting intensity of a factor 1/2 on the $StSt$ liner of the SPS, nevertheless an unacceptable level of multipacting develops under the exposure to nominal intensity $25ns$ LHC beams.

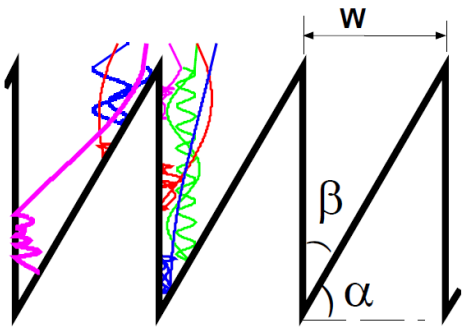

Figure 3.5: Effect of a magnetic field on a grooved surface [58].
The picture shows the relevance of the groove geometry on the secondary electrons confinement.

The surface caused re-adsorption of secondaries is improved on samples with an increased roughness, e.g. where a dendritic structure is obtained by chemical reaction or layer deposition, figure 3.6-a.
An example is the high temperature oxidation of Cu, the fast formation of an oxide film leads to internal stresses and cracks development.
The cracked surface enhances the roughness up to a dendritic texture.
Moreover, the Cu_2O has a lower yield, as most of the semiconductor Me-oxides.
The dendritic surface of picture 3.6-a has a $\delta_{max} < 1$, that is preserved even after more than 24 hours of air exposure.
The main problem of this technique is the applicability on large scales as in the accelerators [3].

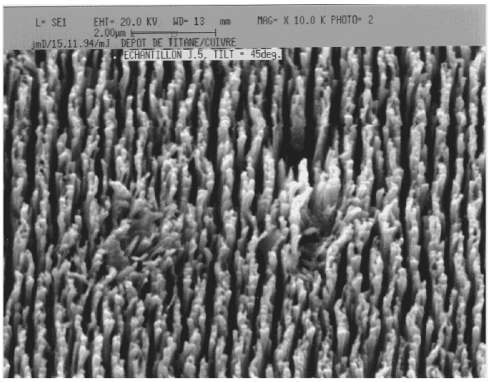

(a) Cu_2O

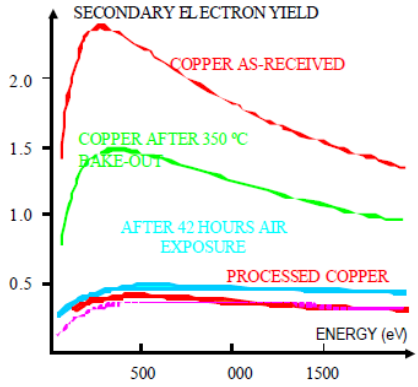

(b) SEY

Figure 3.6: Figure a: Dendritic Cu_2O structure. Figure b: SEY variation [3].

3.3.2 Magnetic roughness

Fine permanent magnets are located underneath smooth, very conductive surfaces to build the magnetic roughness. The prepared samples can have a configuration

either orthogonal or parallel to the surface, the orientation of the magnetic domains is anti-parallel with respect their neighbors.
An Al smooth cover is placed over the magnets frame at a distance which can be modulated by $StSt$ spacers.

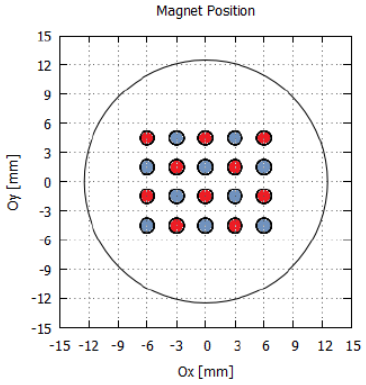

Figure 3.7: Magnetic rough sample, colors underline the anti-parallel structure with the magnets oriented normal to the surface [32].

Three different orientations were tested, the one in picture 3.7 shows the highest SEY reduction starting from the center of the magnets array and integrated over an area of 4 magnets beneath the Al smooth plate [32].
Moving the sample under the e-beam of the SEY measurement test-bench, with primary energies between $200eV$ and $800eV$, it results that the area with the lowest SEY are those within the magnets patterns, precisely those along the magnets axis. The yield reduction is ascribed to the deflection of the secondaries escaping from the surface, meanwhile the primaries are not affected by the magnetic field. An important role is played by the thickness of the plate, or more generally by the distance between the edge of the magnets and the measured surface.
The reduction of δ_{max} is less effective increasing the distance.
One great advantage of the magnetic surfaces is the insensitivity to air exposure and the lower RF losses of geometrically smooth surfaces.
This kind of application can work on waveguide filters, satellites and especially on insulators, which are known for having a huge SEY.

3.4 Thin films coatings

To suppress the electron multipacting it is necessary to reduce the SEY of a surface itself or it is possible to coat it with a thin film of a low SEY material.
The e-cloud mitigation is an hard technological challenge for the CERN accelerators complex, since each part of any accelerator requires to be treated specifically. Thin films are an effective way in reducing the multipacting, the principal realities at CERN are the $TiZrV$ NEG, Non Evaporable Getter, and the C coatings.
NEG is tailored for long straight bakeable beam pipes, since shows a $\delta_{max} = 1.1$ if heated at least at 180℃for 24 hours.
Non bakeable sections, as the bending dipoles of the SPS, could be coated with

aC-coatings.

3.4.1 $TiZrV$ NEG coatings

The most outstanding property of a getter material is its ability of transforming a vacuum surface in a pumping one.
A getter is a surface able to chemisorb and pump by diffusion the several gas species that stick on it. It requires to be thermally activated to dissolve its oxide layer that forms after air exposure, the temperature of activation is a crucial point in accelerators technologies where the maximum allowed temperature for UHV chambers is below 400℃, 250℃ and 200℃ for $StSt$, Cu and Al alloys respectively [11].
Many elements show good getter properties, but only those of the IVb group of the periodic table of elements have an oxygen solubility limit above 10% in the allowed temperature ranges [6].
CERN studies between 1995 and 2002 started from the binary compositions of Ti and Zr, the further addition of V showed an increase in the properties of the getter starting from a reduction of about 50℃ of the activation temperature, figure 3.8.
$TiZrV$ NEG is activated at 180℃ after 24 hours heating, this characteristic is kept for large variety of composition percentages.

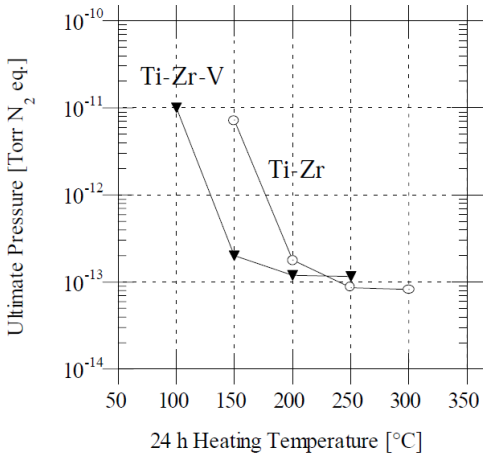

Figure 3.8: Ultimate pressures obtained after 24 h baking cycles, without intermediate air venting, on chambers coated with TiZr and TiZrV.Chambers 2m, diameter 10cm [6].

The activation procedure allows the diffusion of the oxide in the solid phase through the bulk of the material, the temperature is the energy supplier to make this process spontaneous.
The diffusion rate inside a getter material can be enhanced through two mechanisms: the addition of an element that enlarges the lattice space of the compound, or an increase of the grain boundaries number.
$TiZrV$ NEG is characterized by a very effective boundary diffusion due to its

nanometric grains size, between $3nm$ and $5nm$.
These properties are attained as long as the Ti content is lower than 45%.
Getter thin films are used as pumps, they don't absorb noble gases and their pumping speed is inversely proportional to the coverage of the gas molecules.
The pumping speed of species like CO is ruled by the maximum coverage on the surface, species like H_2, instead, can dissociate and diffuse inside the film, their pumping rate decrease in time is much slower.
Roughness heightens the surface sites available for adsorption and the molecules sticking probability thanks to multiple surface impingements.
The dissolution of the *oxide*-layer is the responsible for the low $TiZrV$ NEG SEY.

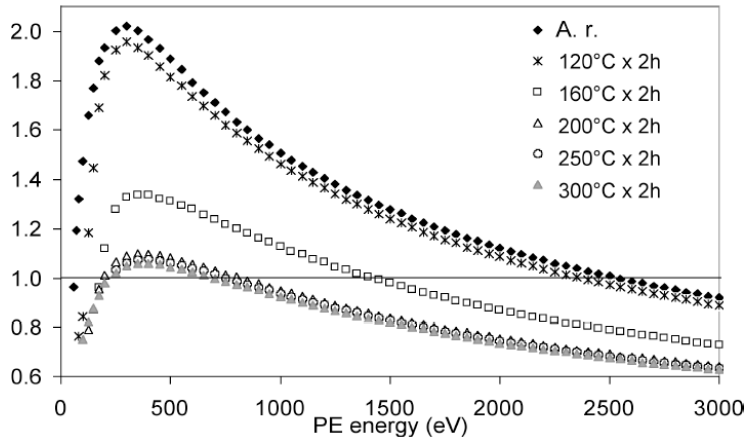

Figure 3.9: $TiZrV$ NEG SEY as a function of the activation temperature [45]. "A.r.", As Received.

Figure 3.9 shows the reduction of δ_{max} of the getter as a function of the activation temperature, the full activation is crucial for the highest reduction of the secondary yield [45].
Inside an accelerator, the e-cloud build up leads to a pressure rise, the NEG activation results firstly in the oxide layer dissolution and consequently in the pumping of the contaminants as CO and CO_2.
It reduces the pressure increase during the beam runs, either if induced by electrons or by photons and ions impingement [11].
The electron stimulated desorption of NEG is at least 10 times lower than $StSt$ for H_2 and CO, if baked at the same temperature [11].
The properties of the film aren't affected by the substrate material, but by its morphology and the deposition temperature.
A film on smooth $StSt$ is smooth and compact, on Al and Be forms a cauliflower structure. A substrate temperature above 200℃ improves the roughness and the sticking probability, but is necessary to keep it below 300℃ to avoid the grain growth and a reduction of the oxide diffusion speed.
The low SEY, the reduced ESD and the pumping skills tail the NEG materials as the best solution for many applications in particles accelerators.
At CERN the long straight sections, LSS, of the LHC have been coated by $TiZrV$ NEG thin films with a standard thickness of $2\mu m$, activated at 180℃ for 24

hours [14].
The $\delta_{max} = 1.1$ is far below the multipacting activation threshold and makes NEG the best solution for the bakeable sections either in LHC and SPS accelerators. To coat the 1200 LSS chambers of the LHC (over $5km$ length), a special facility was built at CERN made of three $8m$ solenoids able to provide up to $300G$ and pumping systems to allow the coating of $7.5m$ maximum length and $60cm$ diameter chambers.
Operating two units in parallel it was possible a weekly production of 20 standard $7m$ long, $80cm\phi$ LSS chambers.
The assembly allows the cylindrical magnetron sputtering of chambers which substrates consisting of $StSt$, Be, Al and Cu.
The chemical pre-treatment of the chambers is fundamental before the coating to improve the film performances. The cathode is made by three elemental rods of Ti, Zr and V twisted together, the simplest cylindrical geometry is provided of one cathode and the DC magnetron sputtered compound has an atomic composition $Ti_{30}Zr_{30}V_{40}$.
The main drawback of NEG is the limited number of activation cycles it can sustain, the basic mechanism is the saturation of the oxigen as a consequence of the oxide dissolution. Even the C accumulation on the surface can decrease the film performances, as this element requires an higher temperature activation to be dissolved in the bulk.

3.4.2 Carbon Coatings

The thermal activation of the $TiZrV$ NEG coatings is a limitation for the non bakeable bending sections of the SPS accelerator. The beam is bent through a magnetic field generated by normal conducting dipoles.
To overcome this limitation, it was necessary to look for other coating technologies. Different coatings were proposed, like TiN which unfortunately is too reactive with oxygen to maintain its low δ_{max}.
As introduced in chapter 2 the formation of a graphite layer is considered the responsible for the yield reduction of the vacuum chambers under electron scrubbing, so carbon was studied as coating material.
The first attempts tried to coat vacuum chambers through Magnetron Sputtering and Plasma Enhanced Physical Vapor Deposition on different geometries and with different thickness, the SEY value is used as a criterion to decide which method is more appropriate.
The sputtered coatings have thickness between 50 and 600 nm, done with graphite cathodes immersed in a $150G$ magnetic field. Ar and Ne nijected as inert gas to develop the plasma, while the temperature of the substrate is free to vary.
A precise description of the coating techniques is reported in [51].
All the samples are subjected to XPS and SEY analysis.
The δ_{max} plot in figure 3.10 shows the results of the SEY measurements, the first conclusion is that the PECVD coatings are inappropriate for the CERN accelerators expectations, the SPS bending sections require surfaces which $\delta_{max} < 1.3$.
All the sample are compared to HOPG, Higly Oriented Pyrolytic Graphite, which has a yield greater than the sputtered carbon.

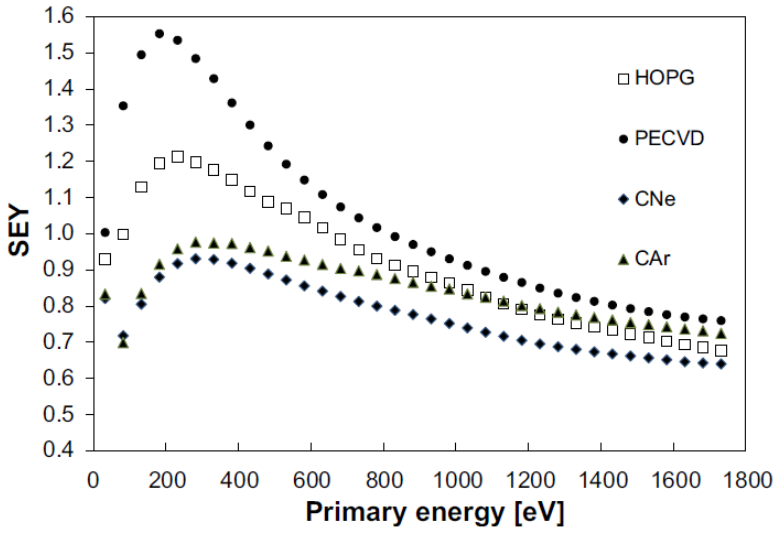

Figure 3.10: PECVD and MS SEY comparison. CAr and CNe refer to carbon coatings made with Ar and Ne inter gases. [51]

To understand the origin of these differences is necessary to consider either the XPS and NRA (Nuclear Reaction Analysis) measurements to discover the composition and the atomic hybridizations of the carbon coatings.
The XPS $C1s$ intensity peak of PECVD and HOPG are compared in figure 3.11, the PECVD peak is shifted to higher binding energies and is wider.

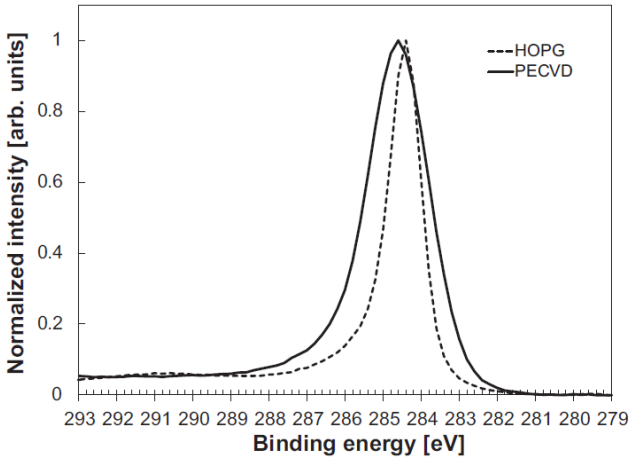

Figure 3.11: PECVD coating $C1s$ peak [51].

The main reason for this behavior is ascribed to the higher presence of H and a different sp^2/sp^3 hybridizations ratio. It is known that the increase in H content leads to a higher tendency to sp^3 bonds as shown in in figure 3.12.
The higher number of sp^3 hybridizations induces a more diamond-like carbon structure. The DLC is a semiconductor and is characterized by an higher SEY.
The enhancement of the sp^3 hybridizations implies the formation of an energy gap in the band structure of the material, it favors the tunneling of the low energy

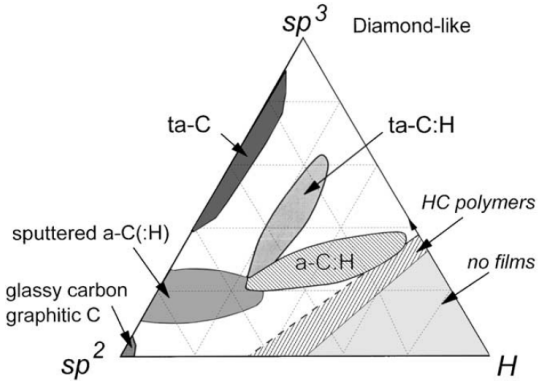

Figure 3.12: $a-CH$ alloys ternary phase diagram of bonding [43].

electrons and reduces the probability of electron-electron collisions dumping, which implies an higher secondaries diffusion length and an increased δ_{max} [42].
The MS samples, instead, show a wider $C1S$ peak than HOPG, it is due to a certain degree of sp^3 hybridizations, as shown in 3.12, and to the possible formation chemical bonds like $C-H$. What is expected, so, is the MS carbon coatings to have an higher δ_{max}, in contradiction with the experimental results 3.10.
Actually it is difficult to relate directly the XPS results to the electron yield of the film, but the surface morphology and the film density can help in understanding the discrepancy between the expected results and the experimental ones.
The sputtered carbon shows an higher roughness with respect the pyrolityc graphite, figure 3.13.
In the previous sections it was introduced the effect of the roughness on the yield of a surface, briefly a rougher material shows a lower δ_{max} with an higher E_{max}.
Furthermore the density of the samples plays a key role in the secondary emission theories, lower densities imply a lower yield. Low density carbon films aren't uncommon in magnetron depositions. If the C coating is treated as an uniform body, the lower density than HOPG can be ascribed to different bonds lengths, internal stresses and dislocations.
In a real case the body can't be uniform and the density varies depending on inclusions, voids and imperfections.
In this case, the scattering of secondaries through defects and pores would limit their free path and escaping ability, reducing δ_{max} [51].
Lastly, the searched coating requires to preserve its properties even after prolonged air exposure. The C coatings were tested in a polystyrene box, in Al foils and in static vacuum.
The latter two storage conditions show a negligible increase of the δ_{max} after one year, and the coating allows a very simple storage method during shutdowns, vacuum breaking and storage, all situations typically faced during accelerators maintenance procedures.
The SEY of the air exposed samples rises because of either the O propensity to form COO chemical species, water contamination and hydroxyl groups formation, which are the typical components of the contamination layers.
CERN developed $a-C$ sputtered coatings with δ_{max} around 1 and robust enough

under long lasting air exposure [13].

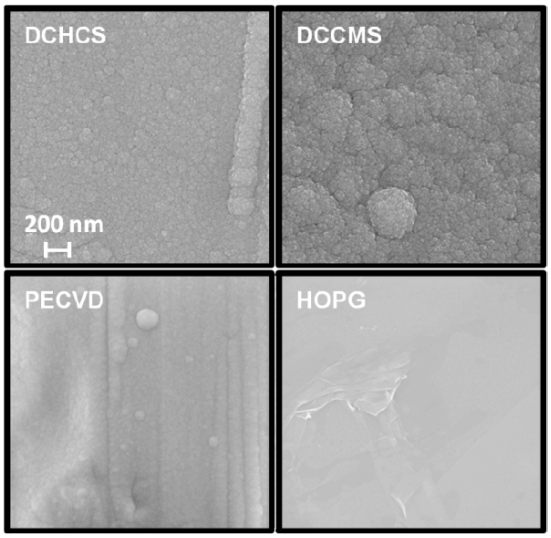

Figure 3.13: SEM of sputtered $a-C$ coatings [13].

Among the possible sputtering configurations, the Direct Current Cylindrical Magnetron Sputtering and the Direct Current Hollow Cathode Sputtering were chosen. The DCHCS is applied on the MBB and MBA dipoles chambers of the SPS.
Previous studies [59] describe the distribution of the e-cloud inside the $StSt$ dipoles of the SPS: the SEY analysis shows how the beam scrubbing is more effective along a central strip on both the beampipe faces, it means the electrons discharge is stronger on the central region of the pipe, figure 3.14.

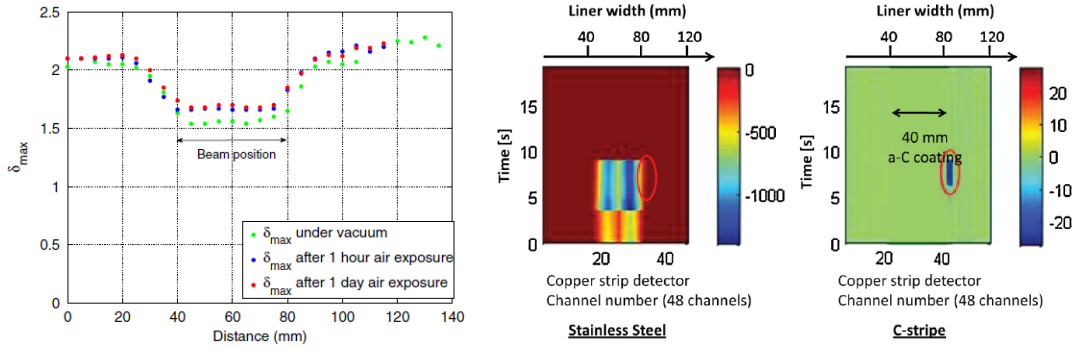

(a) δ_{max} of an SPS chamber after the multipacting

(b) spatial distribution of the e-cloud

Figure 3.14: Left: δ_{max} of an $StSt$ strip from the SPS. Right: e-cloud current signal in the SPS [59].

For this reason, the C sputtered is deposited on the chamber along a central strip $60mm$ wide.
The hollow cathode configuration permits to coat the pipe without disassembling the chamber from the SPS dipole. The cathode is made by a series of electrically

connected, hollow carbon squares, figure 3.15-a.
The shape of the cathodes results in a longer confinement of the electrons into the plasma, every face of the cathode is biased as a cathode's sheath and the electrons are reflected several times between the biased faces before escaping toward the anode's surface, enhancing the local inert gas ionization [**?**].
The cathode squares are installed in a frame provided of wheels to slide inside the dipole, a programmed actuator moves the frame backward and forward during the sputtering to ensure the best thickness uniformity.
In the MBB and MBA chambers the sputtering is operated in Ar, the power supply is set at $3A$ at $600V$ to attain a deposition rate up to $30nm/h$ [13].

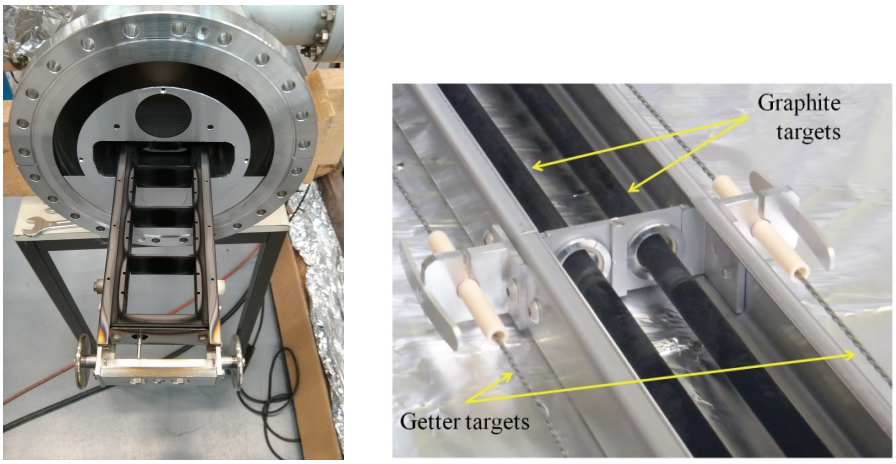

(a) DCHCS (b) DCCMS

Figure 3.15: Left: DCHCS cathode. Right: DCCMS cathode [13].

The DCCMS configurations is preferred to coat other parts of the SPS as the beam-pipes for the quadrupoles.
Figure 3.15-b refers to a trial test on MBB and MBA chambers during development coatings.
Generally speaking, a cylindrical magnetron sputtering is one of the simplest configuration as possible, the chamber is under vacuum, an inert gas is injected and the plasma is ignited under the effect of an external magnetic field.
The CERN facility used the $8m$ solenoids to DCCMS coat the MBA, MBB chambers which were previously baked at 300 ℃ for 24 hours. After, the Ne was injected as inert gas for the sputtering process.
Picture 3.15-b illustrates a DCCMS cathode composed by a double graphite target inserted in a $StSt$ frame with two $TiZrV$-NEG rods aside.
The $StSt$ frame is used to confine the sputtering and coat only a central strip of the chamber, the NEG rods, instead, are used to co-deposit NEG which will act as a distributed pump to reduce the H partial pressure during the plasma deposition.
For power up to $2kW$, with a substrate temperature up to 250℃, the deposition rate can reach $100nm/h$ on the MBA chambers [13].
The aging of the sputtered coatings respects what stated above, the conservation of the SEY can be simply done by wrapping the chamber in Al foils. It is worth to

say that even if the aging mechanism is not fully understood, the preservation of the sample properties in *Al* allows an easy storage of the coated chambers, figure 3.16.

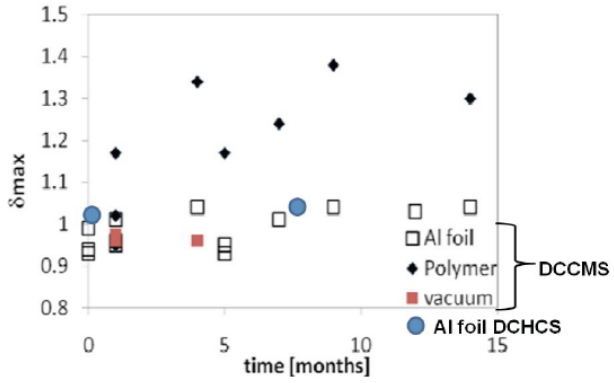

Figure 3.16: Aging of sputtered coatings [13].

3.5 Beam scrubbing

The alternative to reduce the SEY of an accelerator pipe surface is the beam scrubbing.
The self-field of a particles beam accelerates the electrons against the beam-pipe walls and scrubs the pipe surfaces reducing their SEY.
The surface conditioning elicited by an accelerator beam is known as "beam scrubbing".
Usually an accelerator can't inject directly a continuous beam of particles, it is divided in batches. One batch itself is subdivided into bunches, or subgroups, of several particles with a defined time and spatial separation between each bunch. The sequential injection of batches builds the beam.
In high energy accelerators the speed of particles is high enough to be comparable to the speed of light, due to the "Lorentz factor", $\gamma_{v(p)\simeq c} >> 1$, the relativistic contraction leads to an electric field orientation orthogonal to the bunch direction. Since the bunches are even spaced in time, the behavior of self-field can be roughly approximated to an RF TE-wave with the same frequency of the bunch time separation [23, 37].
The wave frequency is a key parameter for the electron cloud build-up: for a defined bunch intensity, if the intra-bunch spacing is too high, the secondary electrons generated by the passage of the previous bunches are lost, the wave is not fast enough to sustain the cascade generation [28].
Then, to sustain the e-cloud, the electrons must survive the interval that separates the passage of two consecutive batches.
Inside the accelerators complex at CERN, the high intensity LHC beams are limited by the e-cloud build up inside the SPS injection line for bunch intensities above $6.0 * 10^{10} protons/bunch$ at $25ns$ spacings [28].

In the early 2000 the first injection of $25ns$ bunches confirmed the limitations either of the SPS and LHC due to the EC.
The SPS has been scrubbed almost every year from 2002 with $25ns$ beams, which allowed to attain a good control of the build-up with a limited pressure rise and a good beam quality [26].
The studies driven along the last ten years inside the SPS take advantage of strip detectors to intercept the electrons and determine both the spatial and energetic distribution of the multipacting, the pressure gauges are involved in the measurement of the ESD pressure rises, figure 3.17.

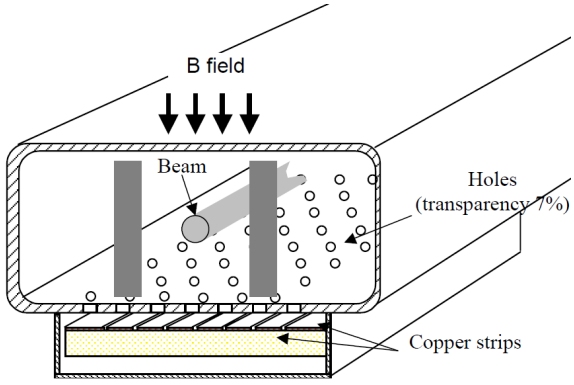

Figure 3.17: Schematic of a strip detector [28].

A strip detector is made of 48 or $36Cu$ wires installed on an insulating sheath of Kapton and placed beneath a beam-pipe provided of holes over the 7% of the total surface, the aim is the electrons extraction without affecting the e-cloud distribution.
The motion of the electrons is influenced even by the presence of a magnetic field, $\vec{B}$, which constrains them along circular orbits around its lines.
The revolution speed of an electron around $\vec{B}$ can be coupled to the oscillations of the bunch self-field and result in an enhanced electron acceleration toward the pipe walls.
As a result, the combined effect of the RF self-field and the magnetic field influences the electron-cloud distribution inside the SPS dipoles.
The different e-cloud shapes between the dipoles bending sections and the non-magnetized straight ones results in a reduction of the bunch intensity threshold for the ignition of the multipacting, which passes from $5.5 * 10^{10} protons/bunch$ to $3.3 * 10^{10} protons/bunch$, $figure 3.18$.
Inside the dipoles, then, the threshold is dependent even on the magnetic field intensity: below $20G$ the e-cloud appears to behave like in a field free region, this behavior could be influenced by the acceptance of the chamber's holes in relation to the dimension of the electrons cyclotron radius inside low field regions [28].
Inside the SPS, the energy distribution of the electrons within the e-cloud varies from field-free to field-filled sections, in the first case the energy peak is around $80eV$ and rises up to $180eV$, $200eV$ in the latter.
It is worth to mention that the strip detector, or electron cloud monitor, isn't able to measure the electrons with energy below $20eV$. The influence of this limitation

should be low since the component of electrons under that energy should have an impact $< 20\%$ on both the pressure rise and the heat load [28].

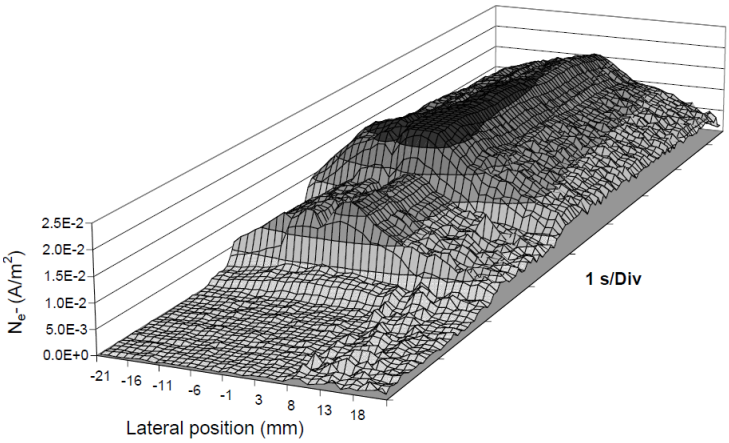

(a) EC dipole free section

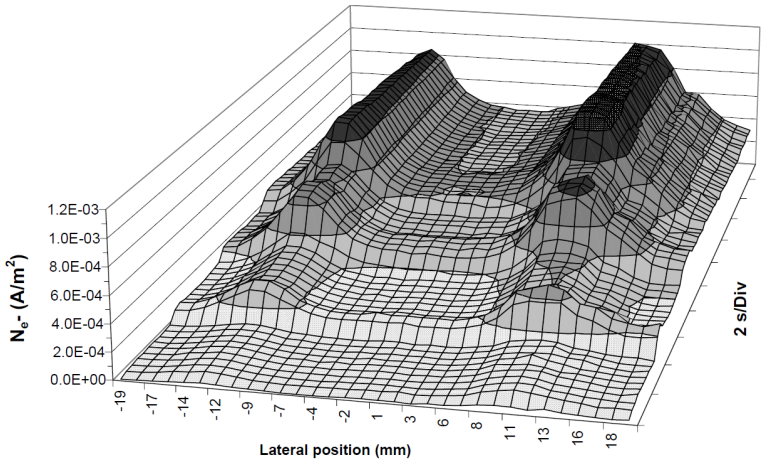

(b) EC dipole section

Figure 3.18: Upper: spread EC distribution in absence of dipole field. Lower: constrained of EC along dipole field lines [28].

A long lasting exposure to the beam can modify the conditions for the multipacting activation: the beam passage stimulates the multipacting which electrons strike the beampipes that get conditioned.
As long as a surface is conditioned it is less prone to emit secondary electrons for the same beam intensity.
The evidences of the beam scrubbing are clear along almost all the SPS where the intensity threshold for the e-cloud build-up increases to $1.0 * 10^{11} protons/bunch$ in the field-filled dipoles sections, and to more than $1.3 * 10^{11} protons/bunch$ in the field-free ones.
The proof of the surface conditioning is evident even in the gauges readings, the pressure rise decreases during the beam runs, figure 3.19-a.

The in situ SEY analysis confirms the reduction of the δ_{max}, figure 3.19-b.
Figure 3.19-b is referred to a measure taken on a second scrubbing run after a venting procedure successive to a first scrubbing test: the SEY appears to lower faster during the second runs, showing a sort of memory effect.
The ultimate δ_{max} reached is 1.5 after four days of beam runs with the LHC beam conditions.

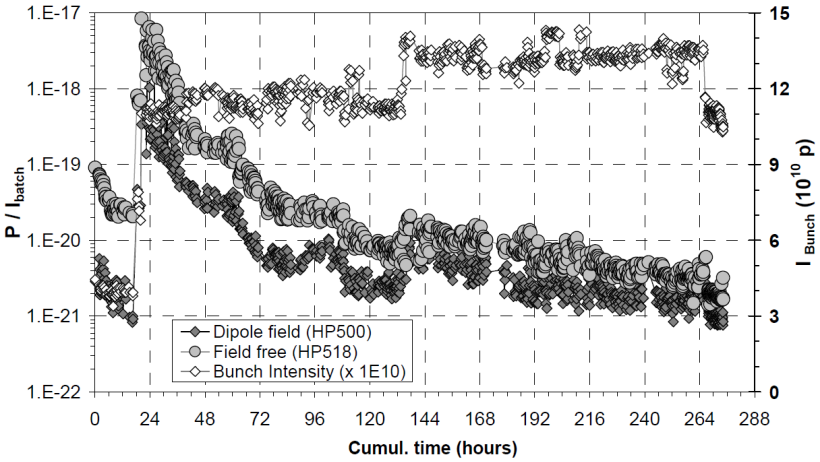

(a) Gauges readings

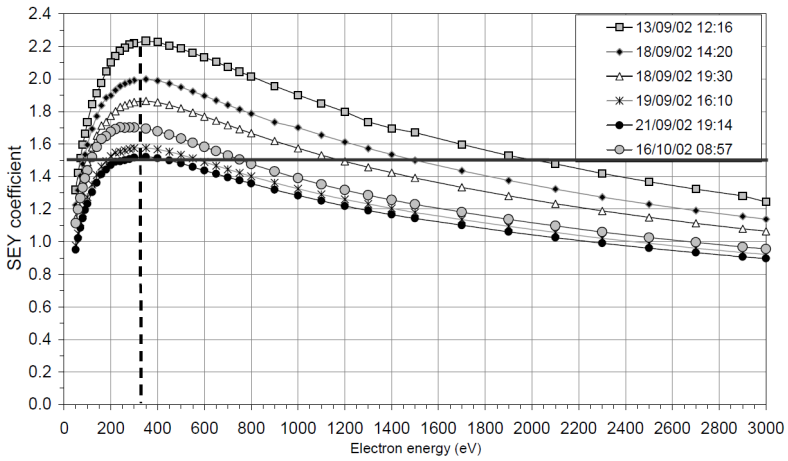

(b) In situ SEY analysis

Figure 3.19: Upper: gauges readings normalized to the bunch intensity. Lower: SEY analysis of the second beam scrubbing runs after venting [28].

In 2011 started a conditioning campaign with $50ns$ beams that efficiently suppressed the EC build-up.
Even the LHC dipoles have been scrubbed: $50ns$ spaced bunches reduced the surface SEY from about 2.3 to slightly below 2.2, this value is enough to allow working in an electron-cloud free environment within an energy range from $450eV$ to $3.5TeV$ [25].
Severe e-cloud problems remain with $25ns$ bunches.
The scrubbing procedure lead along several years inside the SPS allows the storage

of four batches of 72 bunches with $1.15 * 10^{11} protons/bunches$ at nominal intensity, which can be injected inside the LHC without any beam loss.
When the bunch intensity is increased, the multipacting threshold is overcome and the performances of the beam are compromised, figure 3.20.

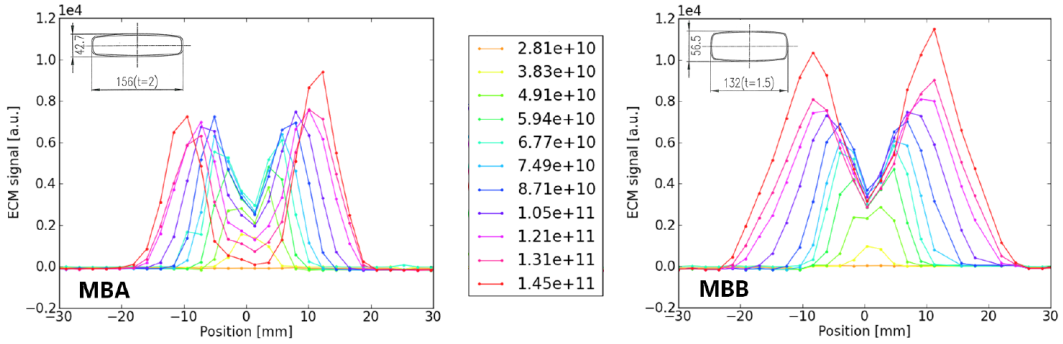

Figure 3.20: Strip detector readings of the SPS MBA and MBB chambers at high intensities bunches [26].

To attain the full intensity beam transfer through the SPS, it is required a deeper scrubbing of the beam-pipes.
The goal is to reach the intensity of $1.7 * 10^{11} protons/bunch$ at $25ns$ and to inject 1 to 4 batches made of 72 bunches every $225ns$ [28].
Simulations propose a "doublet" beam scrubbing as a possible solution for the full conditioning of the beam-pipes. The beam is composed by $25ns$ bunches and each one is made of two sub-bunches $5ns$ spaced.
The shorter distance between the particles bunches should increase the electrons of the EC and rise the scrubbing electron dose, fastening the conditioning.
The experimental runs seem to confirm the simulations, but with some technical problems.
The first challenge is the production of such a beam in the PS and its further transfer to the SPS, neither the direct production in the SPS seems to be easier.
Then, the doublet beam develops an electron cloud which doesn't cover the whole region to be scrubbed, it implies a periodic displacement of the beam to fully condition the beam-pipes [26].
The production of a $25ns$ physics remains critical for the LHC accelerator, the scrubbing test showed a reduction of the yield δ_{max} to an estimated value of 1.52, where the instability of the beam is greatly reduced, but the heat loading and the bunch energy loss clearly indicate there is still multipacting.
In conclusion, the beam scrubbing is a very efficient technique in the reduction of the SEY, but appears to be insufficient to gain the conditions required for the nominal beam intensity and to attain the full luminosity.
One of the key points is the time behavior, the conditioning is very fast and effective in the first hours or days. Further, the reduction of the EC build-up and the decrease of the electrons in the cloud lower either the dose and the energy necessary to condition the surfaces.
As a result the same beam, along time, passes from a fast conditioning to an

insufficient scrubbing.
As for the $50ns$ physics, it looks like a faster and more intense beam is necessary to run through the accelerator to condition the surfaces enough to be able to work with the $25ns$ physics.
The dynamics of the EC development is really complex and not fully clear. The behavior inside an accelerator seems not to fully agree with the simulations and it can be ascribed to the lack of knowledge about low energy electrons and to the possibility of a displacement of the e-cloud from a conditioned region to another one with an higher SEY.

Chapter 4

Hydrocarbon Gas and Surface Interaction

When a molecule adsorbs on a surface it can be bound through either chemical and physical interactions.
The rise of the binding forces in physisorption is ascribed to the sum of a double potential: a long range attractive branch due to Van der Waals forces and a short range repulsive potential due to the electronic shell overlap between the adsorbate and the adsorbant [29].
The Van der Waals forces arise between molecules, atoms and surfaces.
The attractive force is due to the interactions between permanent, fluctuating and induced dipoles.
The repulsive ones are due to the Pauli exclusion principle.

$$V_{VdW}(r) = V_{rep.}(r^{-3}) + V_{att.}(r^{-6}) \tag{4.1}$$

Adsorption can be simply represented through the Lennard-jones potential, figure 4.1.
Since the nature of physisorption is not a chemical bonding, it has no requirements of directionality and its bonds are generally weaker but widespread on the surface.
Chemisorption implies an high perturbation of the electronic state of the molecule which shares its electrons with the adsorbant to build a chemical bond, the molecule is chemisorbed.
It is an highly directional bond as all the chemical ones, it develops on specific sites and is highly dependent on on the exact position and orientation with respect the substrate.
The total potential can have an activation barrier: an energetic step the molecules have to overcome to chemisorb on the surface.
A typical case of chemisorption is the oxidation of metal surfaces.
Oxigen is highly reactive with many metals as Fe, Cu or Al and the degree of reactivity is so high that the chemisorption leads to the formation of new compounds like Me-oxides. The strong tendency of the O_2 in reacting with the metal surfaces is at the basis of the passivation layer formation .
This chapter focuses on the heavy hydrocarbons contamination of an unbaked $StSt$ surface in vacuum.
Technical $StSt$ is typically a passivated surface, because of the exposure to the

ambient environment.
The reduced reactivity of the sorption layer on this kind of surface induces to consider the sticked hydrocarbons as physisorbed.

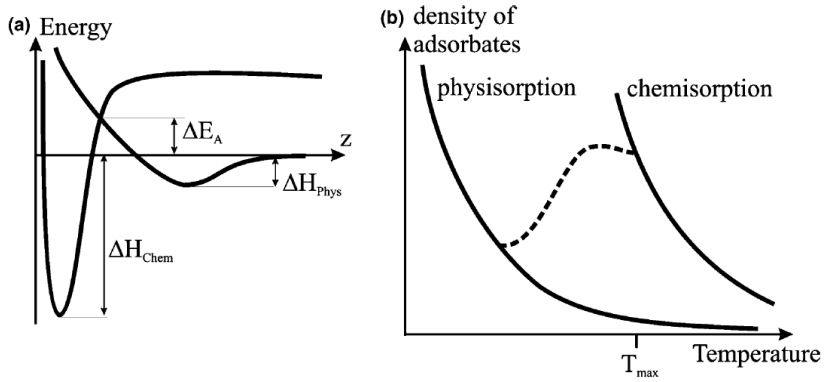

Figure 4.1: Lennard-Jones potential [5].

4.1 The model of interaction

The goal is to study the enhanced electron induced C deposition through the injection and the surface dissociation of hydrocarbon gases.
Experimentally a leak valve injects acetylene, C_2H_2, or dodecane, $C_{12}H_{26}$.
The multicpacting should provide the energetic electrons for the molecules cracking, which generate reactive fragments highly prone to interact with the surface and to be chemisorbed [22].
In the best scenario, the continuous stimulation of this process would lead to a C network formation, a sort of cross-linking, and the deposition of a thin carbon layer with a certain degree of H which will determine the final SEY of the coating.
Once a small volume of gas is injected in a vacuum chamber, the low pressure allows to consider the molecules interacting principally with the chamber's walls, their mean free path results much higher than the dimensions of the system: $\lambda = \frac{K_B T}{\sigma T}$ [36].
Once a molecule hits the surface it is characterized by a sticking coefficient, s, which determines its probability of being adsorbed or reflected.
For sake of simplicity, the present work considers s equal to unity (either for dodecane and acetylene), it means that each molecule that impinges on the surface is assumed to be adsorbed.
Further it is necessary to consider that the system is kept at the environmental temperature $T_{amb} \simeq 293K$ and each molecule is provided of an average thermal energy $\frac{3}{2}K_B T = \frac{1}{2}mv^2$, the thermal excitation is the cause of the spontaneous molecular desorption.
So, each molecule that sticks on a surface lays on it for an average interval of time τ known as "sojourn time".
The thermal excitation of the sticked molecules is dependent on the system tem-

perature, the sojourn time reduces when T increases [29].

$$\tau = \tau_0 e^{\frac{-E_{des.}}{RT}} \tag{4.2}$$

The term τ_0 in equation 4.2 is referred as the vibrational term of the molecules and is generally set as $10^{-13}s$ [22], actually τ_0 is a rather complex factor that arises from the transition state theory. For long molecules it can be tricky, since it is a function of all the possible binding energies and configurations of a molecule on a surface.
From the "Conventional Transition State Theory" the desorption rate can be treated as the rate of a chemical reaction, where the reaction rate K_r of $A+BC \rightarrow AB+C$ is a function of the intermediate transition states, which are points on the multicurve potential difference between the reactants and the products [31].

$$K_{A \rightarrow AB} = (\frac{K_B T}{h})[\frac{q^{tr.}}{q_A q_{BC}}]e^{\frac{-\Delta U_{tr.}}{K_B T}} \tag{4.3}$$

In case of molecular desorption the activated complex of the transition state is the one that leads to desorption [38].

$$K_{des} = (\frac{K_B T}{h})[\frac{q^{des}}{q_{ads.}}]e^{\frac{-\Delta E_{des.}}{K_B T}} \tag{4.4}$$

Where h is the Planck's constant.
In the case of short alkanes and short hydrocarbons like the acetylene, the molecules are approximated as straight chains which desorption from a surface can be represented in the simplest way as a vertical translation from the adsorbed linear state to a desorbed one.
The only variable would be the translation along the coordinate normal to the surface, in this approximation $\tau_0 = 10^{-13}s$.
For long chain alkanes, like dodecane, this statement is not true [38], the desorption follows tortuous paths along several states of binding with different rotational chain configurations and molecular coverages, figure 4.2.
It means that a long chain molecule can even partially desorb and rotate along its gauche and trans configurations, affecting the desorption energy and frequency.
The introduction of a non linear desorption model modifies the values of either τ_0 and $\Delta E_{des.}$.
The desorption energy of an alkane follows a linear trend for short chains molecules, where $\Delta E_{des.} = \Delta E_{des.,0} * N$, for long chain alkanes this model is no more valid.
From Temperature Programmed Desorption tests, the escape energy of a molecule is better approximated by the non linear trend expressed in equation 4.5 [17, 38], figure 4.3.

$$\Delta E_{des.} = -29 + 42 n^{\frac{1}{2}} \frac{kJ}{mole} \tag{4.5}$$

The considerations about the intermediate steps of desorption of long chain alkanes leads to a shift in the value of τ_0 that moves from $10^{-13}s$ to $10^{-19}s$.
The further step is the studying concerning the electron induced dissociation.
The multipacting provides the energetic electrons which would hit the physisorbed

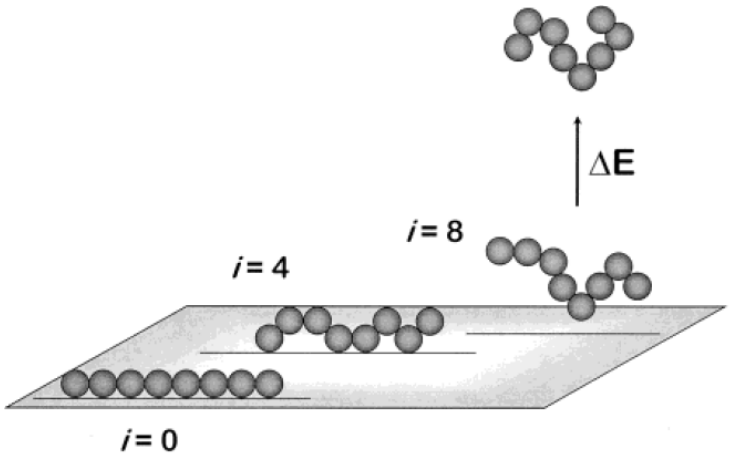

Figure 4.2: Long chain alkane desorption from a surface [17].

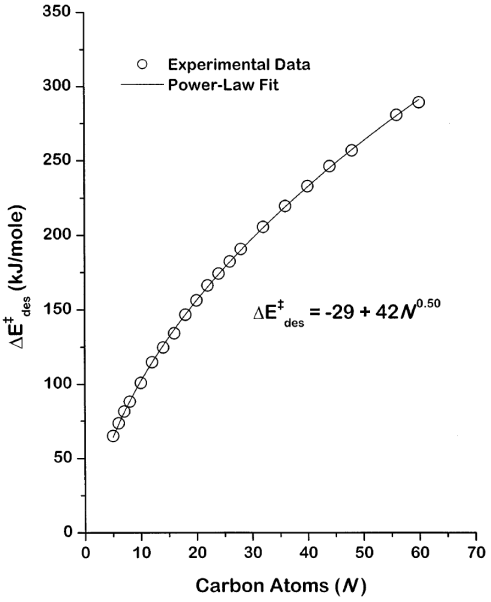

Figure 4.3: Alkanes desorption energy exponential law [17]. The white dots are the experimental results from the TPD, the black line is the exponential law with $\tau_0 = 10^{-19}s$.

layer of hydrocarbons, the simplest model neglects the gas molecules cracking which can improve the number of reactive radicals in vacuum able to react with the chamber surfaces.
The probability of molecule cracking or ionization upon the electrons impact is defined as the electronic dissociation cross section σ_{SE}. SE refers to the accelerated secondary electrons emitted from the unscrubbed surface.
The analytical model takes its steps from the studies Hollensead about the radiation induced carbon contamination of optical surfaces [22].
Consider the injection of an hydrocarbon gas inside a vacuum chamber, the gas molecules travel inside the volume and hit the surface with a frequency Γ with sticking probability s, the number of physisorbed molecules in time is $N_{ad}(t)$.
If we consider a single layer contamination, part of the impinging molecules will be reflected whenever impinge on a site already occupied. In the meanwhile part of the adsorbed molecules will desorb thanks to the thermal excitation and another fraction is dissociated by the electrons impact.
The dissociated molecules can chemisorb on the surface and build the carbon layer.

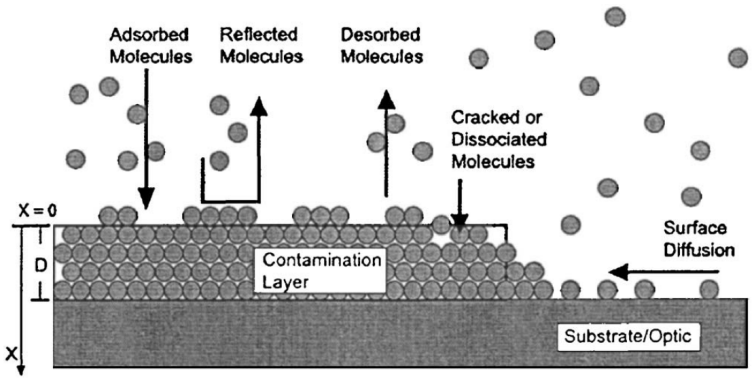

Figure 4.4: General scheme of contamination with gas molecules [22].

The molecular physisorption rate is expressed in equation 4.6.

$$\frac{dN_{ad}(t)}{dt} = s\Gamma - N_{ad}t[\frac{s\Gamma}{N_{ad,max}} + \frac{1}{\tau} + \sigma_{SE}I] \tag{4.6}$$

For sake of simplicity the values of τ and $N_{ad,max}$ are considered constant, it means they are considered coverage independent.
In the present work is taken into account a starting point where the gas is injected before the multipacting development, it mean that at $I(t = 0) = 0$.
The impingement rate of the gas molecules with a vacuum chambers at a maximum pressure in the order of $10^{-5}mbar$ can be described by the kinetic theory of ideal gases, where the molecules are considered as non interacting instead of elastically scattered each others [22].

$$\Gamma = \frac{1}{4}\frac{P}{K_BT}(\frac{8K_BT}{\pi M})^{\frac{1}{2}} \tag{4.7}$$

The molecular weight of dodecane is $M = 170g/mol$, inserting this value in equation 4.7 results $\Gamma = 1.95 * 10^{(-5)}moles/m^2s$.

Equation 4.8 evaluates the volume filled by one molecule starting from its density ρ.

$$\mathrm{V}_M = \frac{M}{\rho N_{av}} \tag{4.8}$$

Where V_M is the molecular volume and N_{av} is the Avogadro's number.
The maximum adsorption sites $N_{ad,max}$ are roughly estimated as the maximum number of allocable molecules per unity of surface: $V_M^{-\frac{2}{3}}$.
The dodecane, for example, has a molecular volume $V_M = 3.6 * 10^{(-25)} L = 3.6 * 10^{-28} m^3$, its $N_{ad,max} = 1.97 * 10^{18} molecules/m^2$.
If the gas is injected before the multipacting tests, its molecules will reach an equilibrium condition between physisorptions and spontaneous desorptions.
Referring to equations 4.2 and 4.5, the sojourn time of a physisorbed molecule of dodecane at ambient temperature, $298K$, is between $2s$ and $6s$.
The equilibrium condition is shown in equation 4.9.

$$\frac{dN_{ad}}{dt} = 0 \tag{4.9}$$

Inserting the condition 4.9 in the equation 4.6, results:

$$N_{ad}(t=0) = \frac{s\Gamma}{(\frac{1}{\tau} + \frac{s\tau}{N_{ad,max}})} \tag{4.10}$$

Which is the initial coverage of molecules in absence of any dissociation phenomena. Once the elctron cloud builds up, the energetic electrons hit the physisorbed molecules modifying the equilibrium conditions: $\frac{dN_{ad}}{dt} \neq 0$.
The system becomes a first order differential equation with an initial condition of expressed in 4.9.

$$\begin{cases} \dot{X} = A - BX & (4.11) \\ X(0) = C & (4.12) \end{cases}$$

Which solution is in the form:

$$X(t) = Ce^{-Bt} + \frac{A}{B}(1 - e^{-Bt}) \tag{4.13}$$

Where B represents the ensemble of the reflection, dissociation and desorption events.
Considering Γ, τ, s and $N_{ad,max}$ as constants, the rate of physisorption and consequently the graphitization of the surface are dependent on σ_{SE}.

4.2 Electron impact dissociation cross section

Finding the right value of σ_{SE} isn't trivial since the cross section varies with the energy of the electrons. It means that to have a good estimation of the C deposition rate is necessary to know the energetic distribution and the number of electrons

generated during the multipacting.
A further problem arises: the superficial carbon layer leads to a reduction of the secondary electron yield and a reduction of the number of electrons generated during the multipacting, it implies that their energetics and number change along the carbon deposition.
Lastly it is necessary to consider the statistic of the fragments obtained by dissociation and their reactivity with the surface: the tendency can vary from $StSt$ to graphite.
Even the energies of physisorption are different according the substrate, $E_{ad,C} \neq E_{ad,SS}$, it implies a variation of the sojourn time, τ, and the shift of the equilibrium conditions and the dissociation rate.
For sake's of simplicity the model considers all the parameters as constants and is used to evaluate the feasibility of the surface contamination through the hydrocarbons dissociation.
From the data collected in the NIST database, National Institute of Standards and Technologies, it is possible to collect the cross section only of the acetylene which is about $4,24\mathring{A}^2$ for $100eV$ electrons, for the dodecane no data are available and is considered in the order of few $\mathring{A}^2$, figure 4.5 .

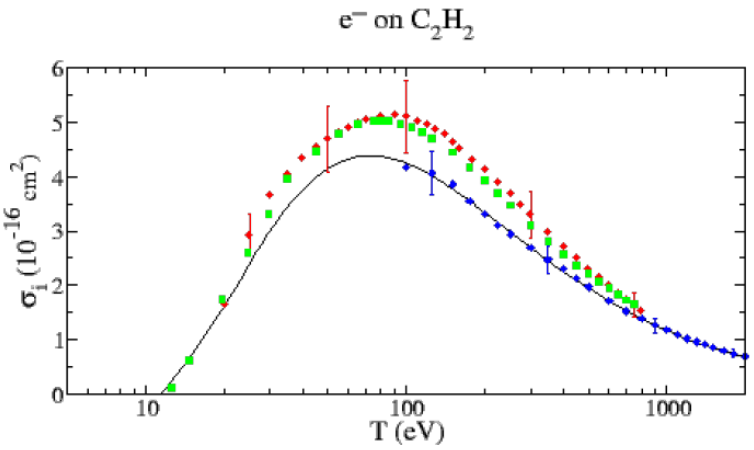

Figure 4.5: C_2H_2 electron dissociation cross section [24].

4.3 Numerical results

The vertical development of the film is considered in terms of single layers build up.
In high vacuum conditions at ambient temperature, one physisorbed monolayer requires less than one second to develop, since the number of impinging molecules per second is higher than $N_{ad,max}$, equation 4.7.
It should be necessary to consider that the effective sticky coefficient is less than 1, but to reduce the complexity of the calculations it is assumed as unitary.

The equilibrium conditions imply that at $t = 0$ the molecular coverage is $N_{ad}(t = 0) \simeq 2 * 10^{18} molecules/m^2$.
In figure 4.6 is shown the typical dose for the *StSt* conditioning under irradiation of an electron gun, a full scrubbing is performed with electron doses about $10^{-3} C/mm^2$, it means a dose of about $1.6 * 10^{22} electrons/m^2$.

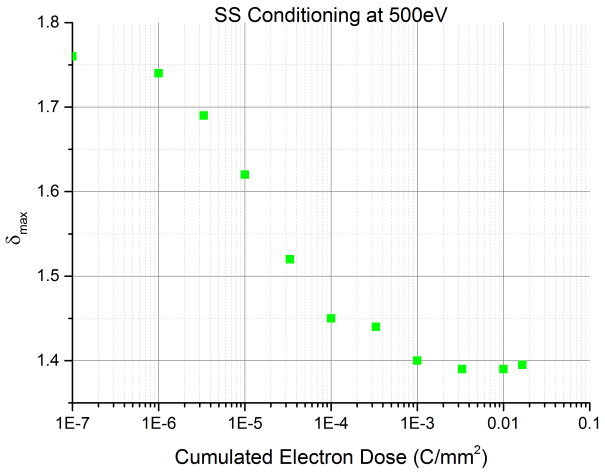

Figure 4.6: Electron gun induced conditioning. The picture refers to the conditioning and the graphitization of a surface exposed to an electron gun at constant energy without the injection of any contaminant. [53]

The cross section of a molecule is in the order of few $\mathring{A}$ at its maximum, for $100eV$ electrons and is approximated as constant across the possible electron energies.
The instantaneous rate of dissociation is $-N(t) * \sigma_{SE} I$, considering an electron current in the order of mA the rate of conversion is high enough to cause a dissociation of a monolayer, which has a thickness of few $\mathring{A}$.
Applying the above considerations for the dodecane injected in the range of $10^{-6} mbar$, the development of an energetic electron cloud should be enough to build a carbon layer in the order of few nm upon an electron dose expected above $10^{-3} C/mm^2$.
The main problem lays in the energetics of the electrons developed inside the e-cloud.
The dissociation cross-section is a bell curve, only the electron energies around the peak have a relevant probability of dissociating the adsorbed molecules and promote the carbon layer development.
If we consider a bell distribution even for the secondary electrons energies, it could be possible to obtain a rough estimation of the effective dose necessary to build a carbon layer on the surface.
The time required for the surface conditioning with the injection of a contamination gas, should follow a decreasing exponential trend.
Unfortunately the experiments performed during this work can't provide the energy curve of the secondary electrons, and the experimental results on conditioning demonstrate how a cumulative electron dose of $10^{-3} C/mm^2$ is not enough to build a graphite layer efficient in suppressing the multipacting.

Moreover, the conditioning of the surface decreases its ability of emitting electrons along time. It results in a weaker multipacting in time which would provide less and less electrons to dissociate the adsorbed molecules.

4.4 Which gas shall we use?

The model proposed has many limitations since the dynamics of the electrons and hydrocarbons interaction is rather complex.
The idea is to be able to find the best contaminant hydrocarbon to study the experimental possibilities of this conditioning procedure.
From a thermodynamical point of view, the only requirements is to have a sojourn time long enough to increase the probability of surface dissociations, it means that heavy long chains hydrocarbons are the perfect candidates for the gas sustained conditioning. On the other hand the sojourn time shouldn't be too long to avoid a permanent contamination of the chamber during the experimental phases.
It would be necessary even to provide a molecules with an high ionization cross-section for the energy of multipacting electrons (up to date unknown).
From the SEY experimental analysis, the most relevant factor choosing the right hydrocarbon is the $C : H$ ratio.
From the picture 3.12 in chapter 3 is possible to argue that an higher percentage of H molecules in the system increases the number of sp^3 hybridized carbon atoms. The result is a more C-diamond-like structure with an higher SEY.
For this reason the best option would be alkyne gases like C_4H_2 butadyine, which unluckily hasn't been provided during the experiments.

Chapter 5

Experimental Set-Up

The "multipacting test-bench" is the experimental set-up developed at CERN for the laboratory studies about the electron cloud build-up inside an RF vacuum cavity and the surface conditioning.
Briefly, it is a coaxial resonator for RF-TE waves, the cavity can be shaped as an MMB or MBA chamber coaxial to a W-wire.
A VNA, Vector Network Analyzer, connected to an amplifier works as an AC power supply coupled to the W wire.
Transversal waves are stimulated inside the test-bench to simulate the RF waves induced by an accelerator beam.
When the right frequency and power conditions are reached, the multipacting can be ignited.
Actually, two RF systems have been developed, both composed by a pre-chamber and a principal chamber, figure 5.1.
In both systems the pre-chamber contains the pumping group, the pressure gauge, the RGA (Residual Gas Analyzer) and a frame to fix the W wire.
The first set-up connects the pre-chamber to an SPS dipole. It is provided of a $6.4m$ MBB or MBA chamber and a DC power supply connected to the dipole to induce the magnetic field.
The second set-up, built along the present year, connects the pre-chamber to a short cylindrical chamber surrounded by a MDHW bending dipole, which length is around $1.5m$ and connected to a DC power supply.
Within the short cylindrical chamber is inserted a $StSt$ liner: an MBB profiled pipe used to achieve the right geometry for the resonator.
The liner is equipped with e-cloud monitor, composed by a strip detector which collects part of the electrons developed during the multipacting, its signal is sent to a DAQ, Data Acquisition system, and processed by a computer.
The cylindrical chamber is also provided of an injection line for the study of the conditioning behavior in presence of injected gases.
Both the systems are equipped with an RGA to monitor the composition of the residual gas.
The VNA is used in both the test-benches to manage the RF coupling and to supply the power for the multipacting development.
Some samples have been introduced in the MDHW test-bench. SEY and XPS measurements studied the yield variation and the superficial composition after the

conditioning.

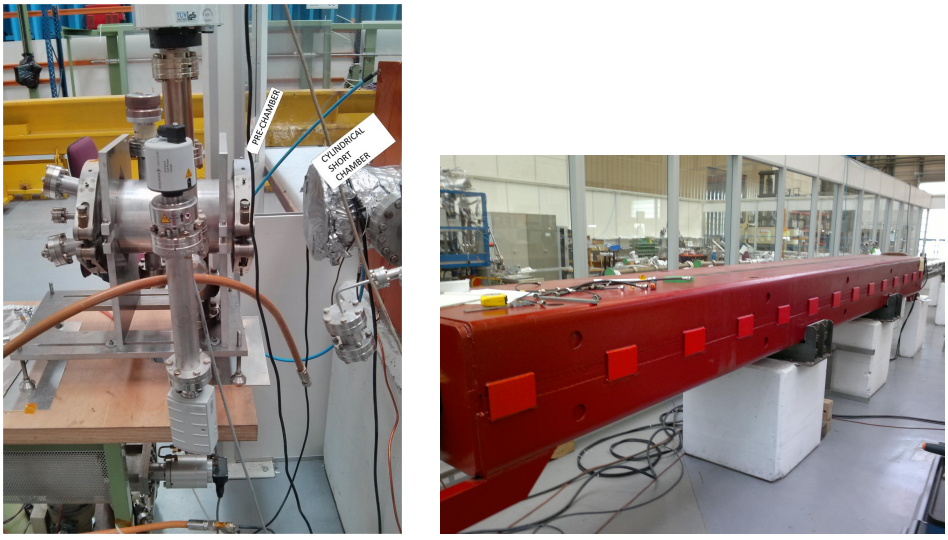

(a) Test-Bench front (b) Test-Bench side

Figure 5.1: The multipacting test-benches. a: Side view of the pre-chamber next to the MDHW bending section. b:The SPS dipole.

5.1 The Vacuum System

Vacuum is a fundamental characteristic of particles accelerators, the pressure reduction is a key factor for the beam quality.
The low pressure implies a reduced number of molecules inside a vacuum chamber, as $PV = nRT$.
If n reduces the molecular mean free path λ increases, on the contrary the probability of collisions between the beam bunch and the gas molecules decreases, enhancing the beam stability.
The multipacting is affected by the pressure since the reduced probability of gas and beam collisions results in a smaller number of gas molecules ionization events, which electrons feed the multipacting and can even cause a plasma discharge.
In a coaxial RF system the very first primary electrons are usually generated by cosmic rays or field emission, those electrons are accelerated by the AC field against the chamber surfaces which have a certain SEY and emit secondary electrons.
It is the beginning of the cascade generation of electrons that leads to the e-cloud formation.
Both the multipacting test-benches share the same pre-chamber, which is provided of a primary and a turbo molecular pumps.
The primay pump is a mechanical rotary one which works compressing the incoming gas by means of a geometrical variation of the volume that contains its rotor, the compressed air is pushed toward the outlet where is ejected through a filter, figure 5.2.
The primary pump is lubricated by heavy hydrocarbon oils which can represent a

serious contamination source, for this reason it is of primary importance to avoid any pressure unbalance between the system and the primary pump.
If the pressure in the system results lower than the inlet of the pump, oil vapors can be sucked and contaminate the system.

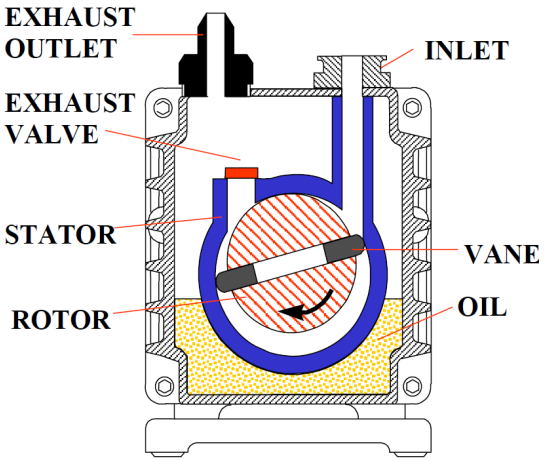

Figure 5.2: Scheme of a primary pump [10].

To further reduce the risk of oil contaminations the inlet of the primary pump is provided of an electro-mechanical valve which closes the connecting bellow between the primary and the turbomolecular pumps.
Mechanical primary pumps reach low vacuum around $10^{-3}mbar$.
The system is also provided of a turbomolecular pump to reach HV or UHV down to $10^{-8}mbar$.
A turbomolecular pump consists of a series of rotors which increase the gas compression ratio at each stage of the series, the molecules are pumped by momentum transfer with the rotating blades.
The effective compression ratio per each kind of gas is a factor proportional to either the speed of the rotors and the molecular weight of the gas species: bigger molecules are heavier and pumped better, H_2 has a low compression ratio and is hardly pumped.
The turbomolecular pump is connected to the pre-chamber by means of a gate-valve which can insulate the system from the pumping group to prevent any contamination.
A "compact full range gauge" monitors the pressure of the test-benches.
The gauge works either in a Pirani and a cold cathode modes, respectively for low and high vacuum in a range between $1bar$ and $5.0 * 10^{-9}mbar$, with an accuracy $\simeq 30\%$ kept down to $1.0 * 10^{-8}mbar$ [54].
In a Pirani gauge a metal filament is heated by a precise current up to a steady temperature, the resistance of the filament varies upon the heat transfer with the impinging gas molecules.
In the range between $1mbar$ and $10^{-4}mbar$ the temperature variation of the filament is linearly proportional to the gas pressure, figure 5.4.
Below $10^{-4}mbar$ the heat transfer method looses of linearity and ionizations gauges can be used.

Figure 5.3: The old damaged turbomolecular pump of the pre-chamber. The blades are scratched, it influenced the pump performances and required to be changed.

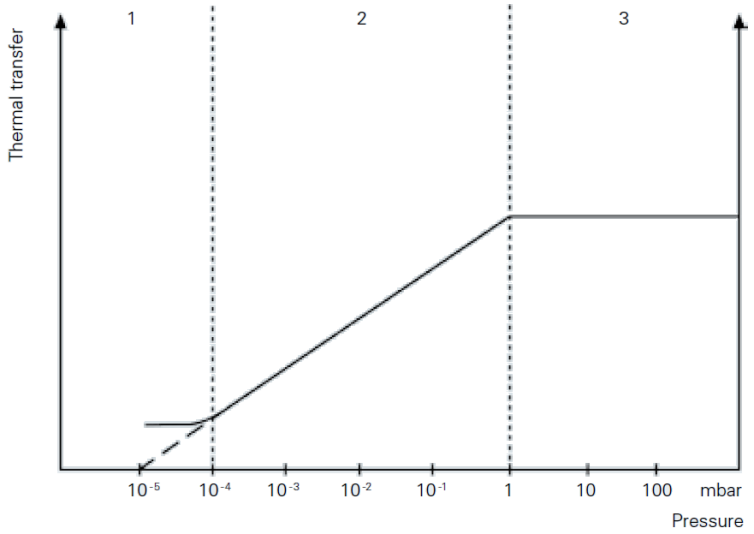

Figure 5.4: The linear heat transfer behaviour in low vacuum conditions [55]

.

Cold cathode gauges are ionization gauges with electrodes charged at few kV potential difference. The cathode emits electrons, these travel towards the anode and ionize the gas molecules which are attracted by the negatively charged cathode.
The gauge is provided of a magnetic field which constrains the electrons along circular trajectories, it increases their path between the electrodes and the probability of ionizing the gas molecules, figure 5.5.
The registered ion current is proportional to the gas pressure.

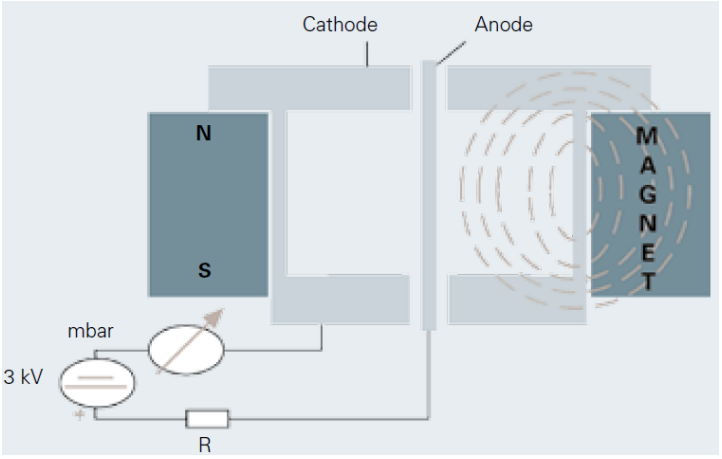

Figure 5.5: Scheme of a cold cathode gauge [55].

The compact full range gauge is connected to an external controller which indicates the pressure of the system.
The controller itself is connected to the computer through an $RS232$ serial port, the pressure readings are acquired during the multipacting tests by means of a specific LabVIEW® program written for the electron-cloud tests.
The pressure rise is one of the first advices of the multipacting development, as a consequence of the ESD.
The maximum pressure reached is an indicator of the electron cloud intensity and the status of the surface.

5.2 The injection line

The injection of a gas is a key factor of the tests about the surface conditioning.
In case of an hydrocarbon gas, it is expected to fill the vacuum chamber and adsorb on its surfaces, the electron-cloud would provide the electrons for the molecule cracking and the carbon deposition.
A gas injection line is installed on the side of the MDHW test-bench principal chamber. Different gases have been used during the experiments and the injection line required to be adapted.
Basically, the line is composed of a gas source, either in liquid or gaseous states, and a mechanical leak valve connected to the system.
The injection pressure inside the chamber is controlled through the gauge and is maintained below $10^{-4} mbar$.

The first trials have been conduced with the acetylene, C_2H_2, which is gaseous in ambient conditions. The injection line required only to connect the bottle to the mechanical leak valve.
The same scheme has been adopted for the injection of Ar.
The dodecane, instead, is an heavy hydrocarbon, liquid at standard conditions.
Its line has been studied to vaporize the hydrocarbon before the injection. This task has been achieved installing a pump on the line before the mechanical valve.
The vapor pressure of the dodecane is $0.2mbar$ at standard conditions, it is enough a primary mechanical pump to vaporize the hydrocarbon before the injection through the leak valve, figure 5.6.

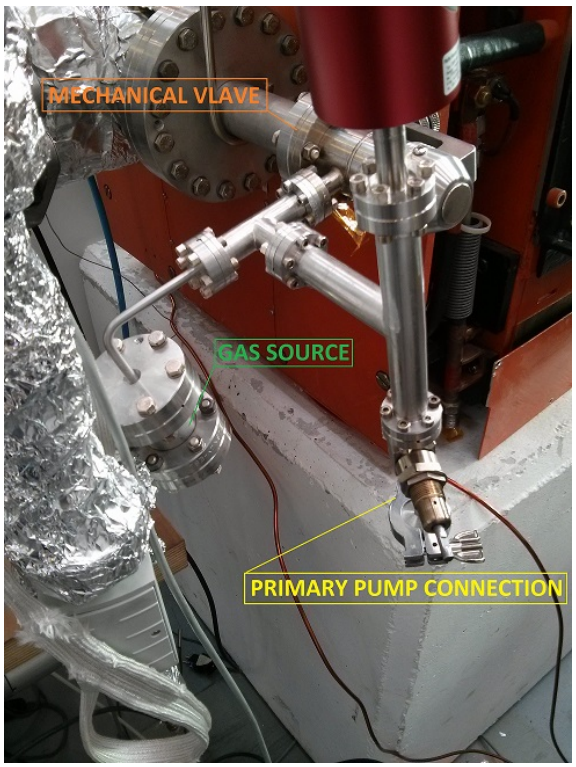

Figure 5.6: The gas injection line.

5.3 The RGA

The pre-chamber of the test-benches is provided of an RGA, Residual Gas Analyzer, to determine the composition of the gases inside the vacuum chamber.
This instrument is fundamental for the control of the vacuum quality in any vacuum system, it allows to check the presence of contaminants in the residual gas and can be used for the leak detection in absence of a dedicated instrument.
During the present work the RGA has been used even to check the hydrocarbon gases flow through the injection line.
The RGA is a mass spectrometer which works detecting the gas species on the

basis of their *mass/charge* ratio.
The basic scheme shown in figure 5.7.

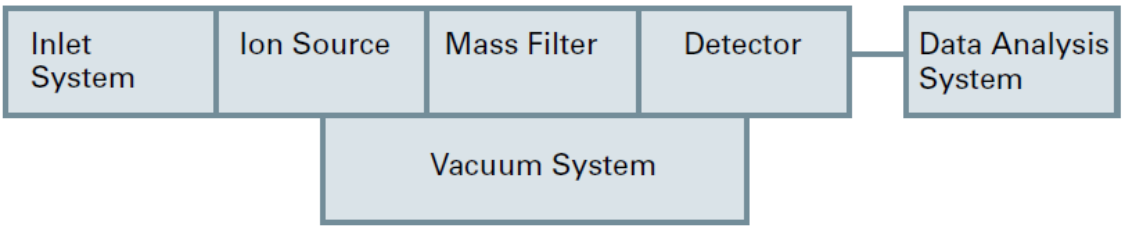

Figure 5.7: RGA block diagram [55].

The neutral molecules inside the vacuum system reach the RGA inlet, where they're ionized by electron impacts.
Inside the RGA of the present system the electron source is a W filament negatively biased, the electrons are thermoelectrically generated and further accelerated from the cathode.
The electron impact ionization cross-sections defines first the probability of ionizing a gas species and further the obtained ions, in fact each molecule has more than one possible ionization scheme, or cracking pattern.
It means that, for any molecule, there is more than one *mass charge* possible ratio, each one with a certain probability.
The ions are then accelerated toward the mass spectrometer which is an electrical quadrupole biased by a non-null DC field plus an AC voltage: $U_T = U + V(\omega t)$.
The quadrupole is made by four rods biased by pairs, figure 5.8, and works as a filter: only the species with a limited *mass charge* ratio can pass through the filter.
The scan of all the species is possible by modifying the voltage of the quadrupole and consequently the accepted ratios.

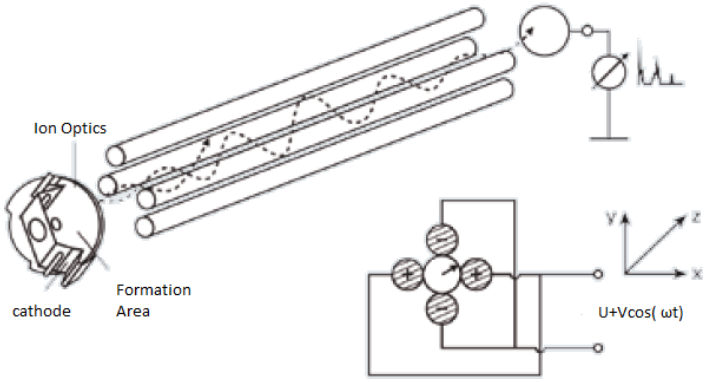

Figure 5.8: RGA quadrupole mass spectrometer [55].

The ions that pass through the spectrometer reach the detectors.
The RGA installed for the experiments uses two detecting systems: a Faraday cup

for the direct detection of the ions current and a SEM, Secondary Electron Multiplier, for the amplification of low ions currents.
In the first case the ions hit the Faraday collector on which develops a current proportional to their relative pressure. By means of a capacitor and a resistor the signal current is converted to a voltage which is read by the RGA acquisition system.
At very low pressures the ions current is very low and the$current/noise$ ratio is so high that an amplification of the signal is required.
In these conditions the SEM is activated, it develops a secondary electrons cascade through its biased dynodes that amplifies the original ions signal.
The SEM is more sensitive than the Faraday cup, but requires to work strictly below $10^{-5}mbar$ to avoid any risk of damaging or accelerated ageing.
In any case the RGA requires to work at low pressure, at most in the range of $10^{-6}mbar$, since an higher pressure can induce a gas discharge inside the electronics of the RGA damaging it, [55].
The units are the ions currents and the amu, atomic mass units, the height and width of one peak of the scan is often associated to more than one species with the same $mass/charge$ ratio. It is necessary to know all the cracking patterns of the species and their relative abundance to be able to distinguish their presence in the gas composition.
Some examples of the processes that can occur upon the electron impact are reported in table 5.1, the cracking pattern indicates either the possibility of ionization and breaking of the gas molecules.

$ABC^{+} + 2e^{-}$
$ABC^{++} + 3e^{-}$
$AB^{+} + C + 2e^{-}$
$BC^{+} + A + 2e^{-}$
$A^{+} + BC + 2e^{-}$
$C^{+} + AB + 2e^{-}$
$B^{+} + A + C + 2e^{-}$

Table 5.1: Many types of ions are formed when ionizing complex molecules. Fractal ions occur in addition to single and multiple charge molecules ions [55].

For heavy hydrocarbons like the dodecane, which molecular mass is $170g/mol$, the cracking products have high atomic masses, in such cases it is possible to control their presence in the system making a scan before and after the injection, controlling the variations of the masses above about $50amu$.
An example of RGA mass scan is shown in figure 5.9.
The result of the dodecane injection, in this case is visible on the peaks around 55, 70 and 85.
Once the gas composition is known, it is possible to set the RGA to control the behavior of defined species along time, this feature is extremely useful during the multipacting to follow the partial pressure profile of the species typically released as a consequence of the ESD, figure 5.10.
During the hydrocarbons experiments it is used to identify the trend of the contaminant gas consumption.

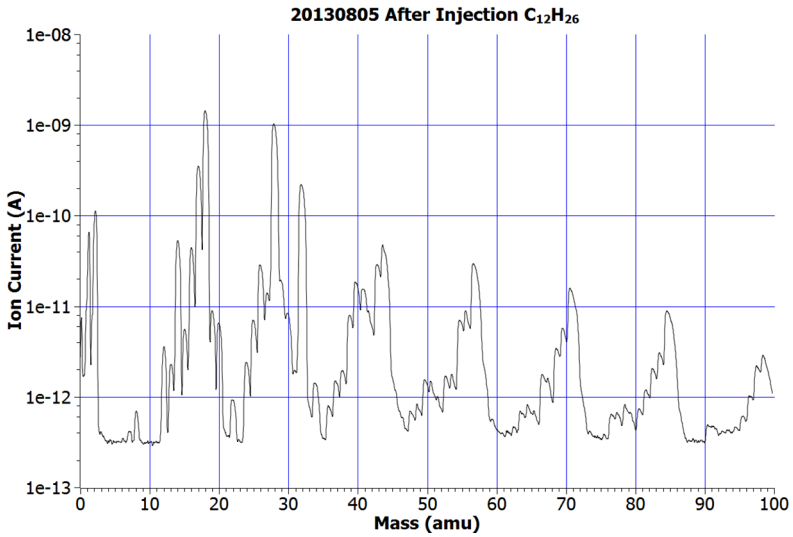

Figure 5.9: RGA mass scan. The measurement has been taken after the dodecane injection. Generally, the high peaks at masses above 50 amu indicate heavy hydrocarbons contaminants.

The aim is to detect traces of hydrocarbons consumption as a consequence of the surface adsorption and decomposition to build the carbon layer which should reduce the SEY of the surface.

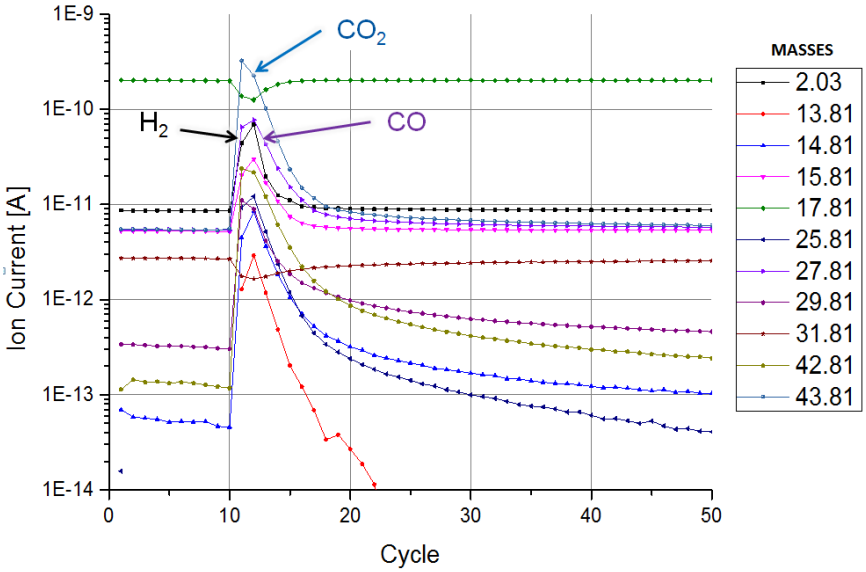

Figure 5.10: Example of masses followed by the RGA during the ESD induced by multipacting.Cycles are the equivalent of time.

5.4 The RF system

An electric field is generated within the test-benches.
The AC field accelerates the primary electrons against the chamber walls, as a consequence secondary electrons are emitted from the surface.
The multipacting test-benches themselves are RF systems which provide the accelerating field for the primary electrons.
The vacuum chambers are crossed by a W wire connected to an external RF generator, the VNA, on one side and short-circuited to the chambers on the opposite extremity of the systems, figure 5.11.
Both the MDHW and SPS dipoles benches are elliptical resonators.
The W was chosen as conducting wire for its thermal properties: an extremely high melting point and a very low thermal expansion coefficient.
The main drawback is a lower conductivity with respect other thermally less stable metals, it means that a greater part of the input power is dissipated as resistive heat instead of generating a stronger electric field.
According the geometry of the system (MBB or MBA profiles) only determined frequencies can build the "wave-modes" which can propagate inside the resonator, those are the resonant frequencies of the system, all the others can't propagate inside and are reflected at the RF input.

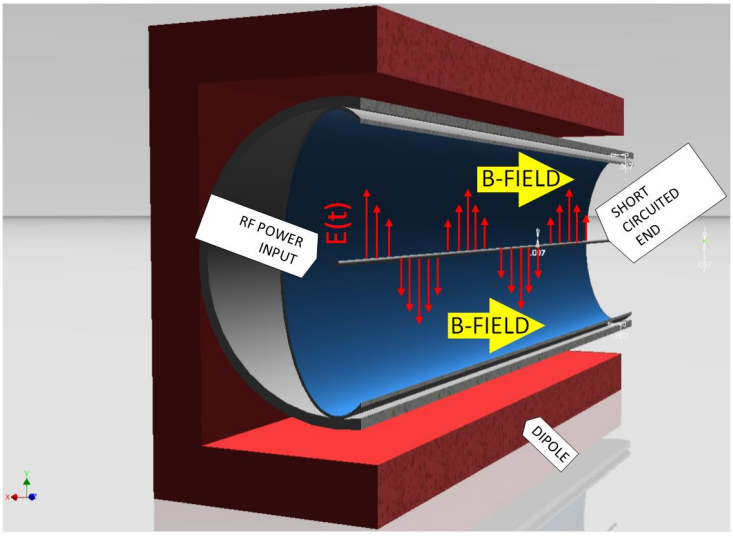

Figure 5.11: Drawing section of the MDHW bending dipole system resonator.

Inside an RF resonator the modes of the cavity are influenced by the geometry of the system. Once the geometry of the chamber is fixed, the geometrical stability of the wire plays a key role in the stability of the resonating modes.
The W is thermally stable, then it remains necessary to keep its geometrical stability: the wire must be fixed and stretched, no bends or curves are allowed which can vary during the experiments changing the frequency coupling of the system.
Both the multipacting test-benches are provided of the same pre-chamber which contains the frame to stretch the W wire.
The stretching frame is a disc made of ceramic, the W wire is connected to a

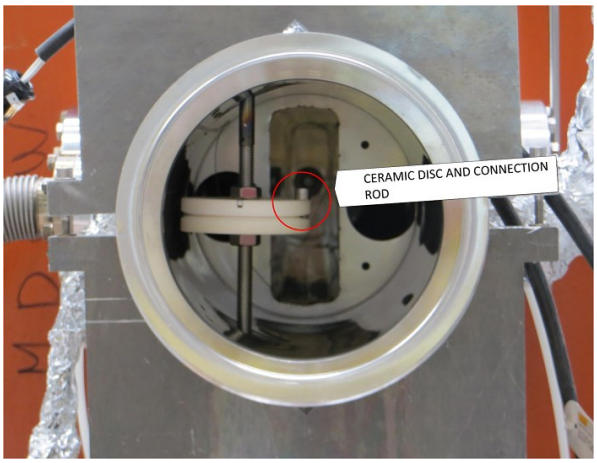

Figure 5.12: The pre-chamber section and the frame to stretch the W wire.

metallic rod which crosses vertically the ceramic disc, figure 5.12.
The rod has a small screw which touches and constrains the conductive wire, from the bottom of the rod starts a short Cu wire covered with ceramic pearls, it is the electrical connection between the external RF power input and the W wire.
At the other extremity of the systems, the W wire is fixed into the rear closing flange, the electrical contact between the system and the conductive wire develops the grounded short-circuit to build the resonator.
Once the W is installed and the system is put under UH vacuum, it is necessary to provide the power to develop the electric field inside the test-bench.
Both the SPS and the MDHW dipole systems are connected to an RF pulse generator: the Rohde & Schwarz® ZNB4 VNA.
The VNA is firstly used to scan the frequency coupling of the resonator at very low power, in other words the modes able to stand inside the chamber. Then, it is used to provide the power ramps to induce the multipacting at the chosen frequency.
For this purpose the RF connections between the VNA and the system plays a key role.
Both the systems can have the same profile, but the different lengths modify the frequencies of the wave modes inside them.
The SPS dipole can have either an MBA or MBB chamber, it affects slightly the frequency of the test-bench. To obtain almost the same working frequency for both the systems, it was necessary to modify the RF connections scheme.
Since the study of the RF fields distributions inside the chambers is rather complex, the modifications on the connections were tested empirically.

5.4.1 The SPS Dipole RF set-up

In the SPS dipole the VNA output is connected firstly to a power amplifier and then to a directional coupler.
The directional coupler drives the "input wave" toward a diplexer (a two channels signal transducer), which high frequency end is filled with a 50Ω resistor and the other is connected to the input of the system.

The directional coupler has 6 ends: one receives the input wave from the amplifier, then transmitted to the diplexer, three are filled with 50Ω resistors to avoid any unwanted loss and one is connected to the input of the VNA to collect the reflected power, figure 5.13.
The intermediate steps between the amplifier and the system input has the role of matching the VNA output signal with the resonator to build the resonant modes of the system.

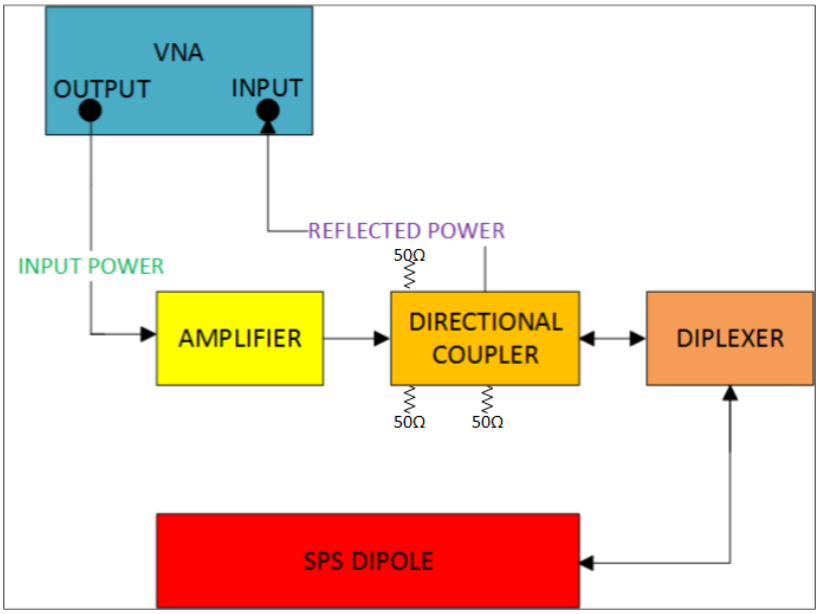

Figure 5.13: Block diagram of the SPS RF coupling system

The VNA output spans the resonance frequencies between $20MHz$ and $220MHz$ with a low power signal along steps of $20kHz$. The range is determined by the stability interval of the power amplifier.
When a frequency represents a mode of the resonator, great part of the input power is transmitted inside the chamber through the wire, the remaining is reflected to the VNA_{input}.
If, instead, a frequency can't stand inside the resonator, it is almost fully reflected. The ratio between the transmitted and the reflected power is read by the VNA and builds the frequency diagram of the system, figure 5.14.
The VNA has a low power output, its signal is enhanced by the power amplifier, so the reflected power at the VNA input is defined as $VNA_{output} * Amplification - Tramsmission$.
The higher the transmitted power, the higher the ratio and deeper the resonance peaks, figure 5.14.

$$dB_{measured} = -20Log(\frac{VNA_{output}}{VNA_{input}}) \tag{5.1}$$

The resonant mode chosen for the tests on the SPS is usually one between $140MHz$ and $150MHz$, figure 5.15.

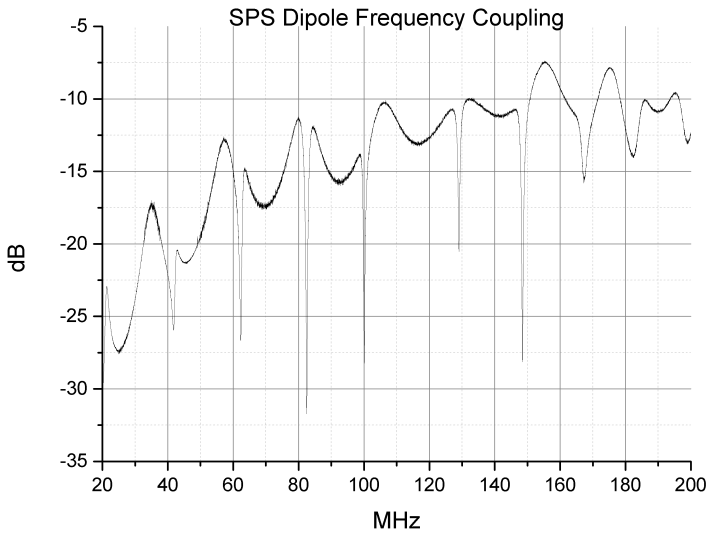

Figure 5.14: SPS test-bench frequency scan. The valleys represent the modes of the resonator.

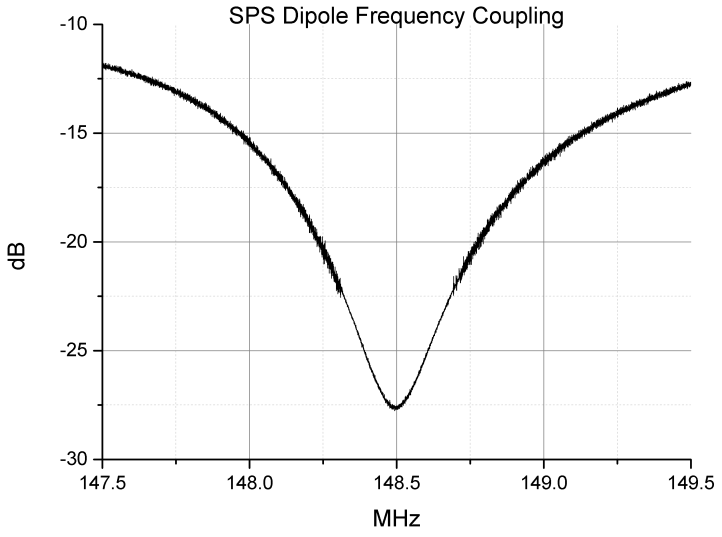

Figure 5.15: Expample of one SPS transmission peak used for the tests.

5.4.2 MDHW Bending Dipole RF set-up

In the second test-bench the RF connections avoid the diplexer and substitute it with a t-junction connected, on one terminal, to a short cable open circuited, and to the input of the system on the other terminal, figure 5.16.
The resonator is built inserting the MBB profiled liner inside the short cylindrical chamber.
Even in this case, the RF transmission cabling has the goal of matching the resonant modes inside the resonator.
For this test-bench two different power amplifiers were used, since the first one (the same used previously on the SPS system) broke during the measurements.

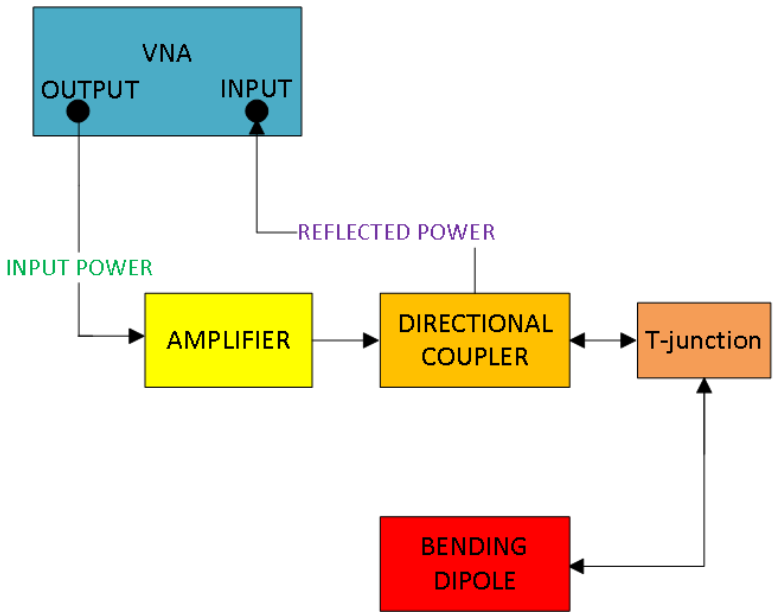

Figure 5.16: Block diagram of the MDHW bending dipole RF coupling system

Both amplifiers have the same range of stability in frequency, so the VNA spans in a range between $20MHz$ and $220MHz$, 5.17.
Going to higher or lower frequencies means overcoming the linearity range of the amplifier, resulting in a distortion in the ratio between the input and the output power.

5.5 The magnetic field

The bending sections of a particles accelerator are built with very large radii of curvature to slightly bend the beam trajectory along their direction.
The bending field is stimulated by a DC current flowing through the coils of the magnets.
Any DC-current induced magnetic field, $\vec{B}$, is characterized by a cyclotron frequency.

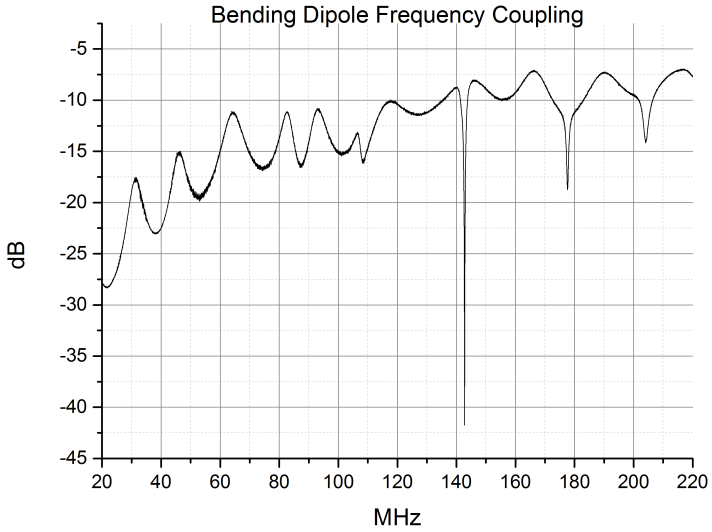

Figure 5.17: MDHW Bending dipole frequency scan.

It means that exists a frequency, ν, of the electric field that perfectly couples with the motion induced by the circular trajectories along which the electrons are constrained during their paths in the magnetic field.
In this case, any electron traveling along the cyclotron trajectories around the $\vec{B}$ liner, receives the strongest acceleration kick by the electric field components $\vec{E(\nu)} \perp \vec{B}$.
The cyclotron resonance condition enhances the efficiency of primary electrons in extracting secondaries.
It implies that is necessary to provide less energy to the system to start the multipacting.
In both the test-benches the dipoles are connected to a DC power supply working in "current-control" mode.
Since $B \propto I_{powersupplier}$ it is crucial to keep $I_{powersupplier}$ constant.
As $I_{powersupplier} = \frac{V}{R_{dipole}}$ and $R_{dipole} = R(T)$, the "current control" varies the output tension to keep the current fixed.
The magnetic field of the MDHW dipole is controlled by means of a gaussmeter provided of a transversal probe.
In the SPS dipole is not possible to insert a magnetic probe, the value kept as reference is the current density of the DC power supply.
Its necessary to check frequently the value of the field since the dipole coils can be affected by heating induced variations and shift their field up to $1G$.
The Rf systems generates an electric field of frequency ν, which cyclotron resonant magnetic field is $B = \frac{e\nu}{2\pi m}$.
Any variation of the magnetic field value would lead to a shift from the cyclotron coupling, as a consequence the system would require more power to develop the multipacting.

5.6 The e-cloud monitor

Multipacting is a cascade generation of secondary electrons.
Their amount inside the MDHW test-bench can be monitored through an electronic device: the e-cloud monitor.
It returns an electrical signal dependent on the number of electrons that hit the liner surface.
It is composed by a strip detector made of 47 Cu stripes connected to a weak positive potential, which prevents the secondary emission from the Cu surface upon e-cloud electrons impingement.
The Cu stripes are installed on a *kapton* sheet which insulates one stripe from the others and from the system.
The stripes are $2mm$ wide and separated by $0.17mm$ of kapton, figure 5.18

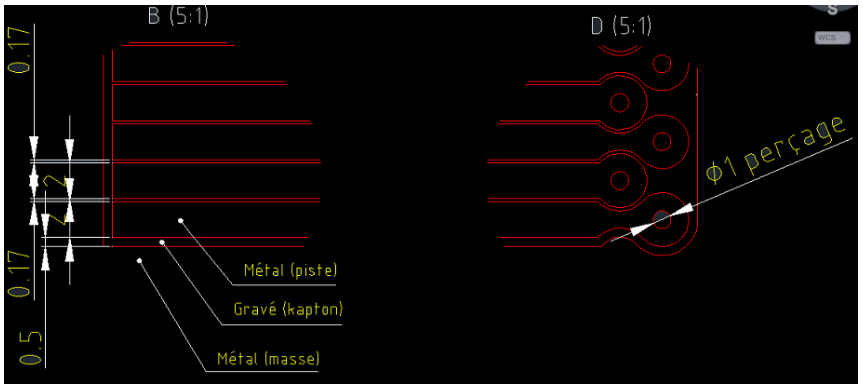

Figure 5.18: e-cloud monitor stripes, technical scheme.

The kapton sheet is put on the stainless steel liner which is inserted inside the MDHW vacuum chamber, figure 5.19.
The liner is a $StSt$ frame of hippodrome-like cross-section with the same profile of an MBB dipole chamber, aside of the holes is provided of small rods used to fix the strip detector, figure 5.20.

The liner is characterized by a series of holes that allow the electrons to escape the chamber and reach the Cu stripes of the kapton sheet, the total transparency of the liner is 7%.
It means that the amount of electrons impinging on the monitor is only a small fraction of the total number of electrons generated inside the liner, figure 5.20-a.
From each Cu strip of the kapton sheet develops a wire which ends in a $DB50$ port installed into a flange on the side of the vacuum system, figures 5.19.
The port is provided of 50 electrical pins, 47 are connected to the strip detector, 1 is grounded to the $StSt$ liner and 2 are unused.
The 47 pins are grouped in 16 channels, it means that the Cu stripes of the detector are electrically grouped by 3 in the first 15 channels, the 16^{th} contains the remaining 2 stripes, figure 5.20-b.
Each channel is connected to a battery box containing $9V$ batteries which provide the weak potential to avoid any secondary emission from the monitor.

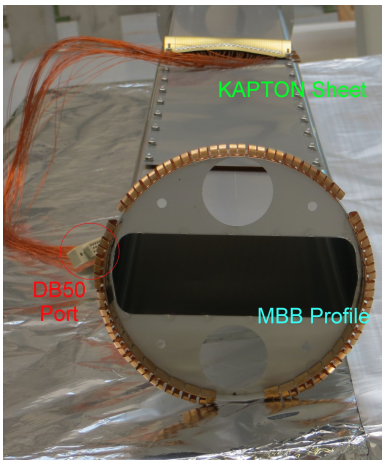

Figure 5.19: Strip detector installed on the *StSt* liner.

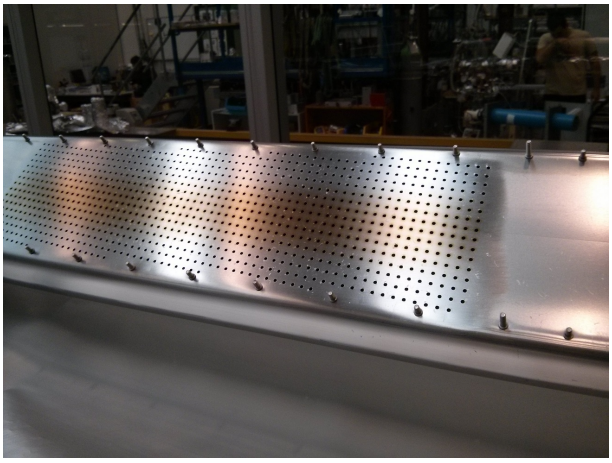

(a) liner

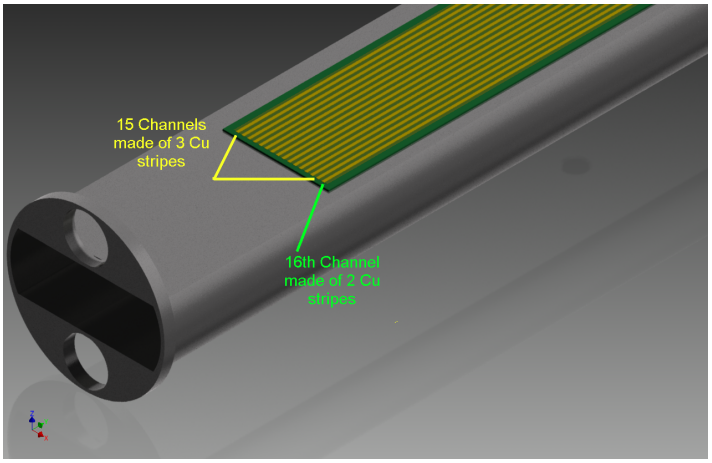

(b) electron cloud monitor channels

Figure 5.20: *StSt* liner. Figure a: It is possible to see the holes for the electrons extraction, and the small rods to fix the kapton sheet of the e-cloud monitor. Figure b: section drawing of the e-cloud monitor channels distribution.

The 16 channels continue beyond the battery box toward the *DAQ*, figure 5.22.
The acquisition system is a National Instruments® USB 6221, single amplifier.
It returns a voltage difference proportional to the resistor installed on its terminals, $V_{DAQ} = R_{DAQ} I_{DAQ}$.
The equivalent electrical circuit, per each channel, is shown in figure 5.21 -b.

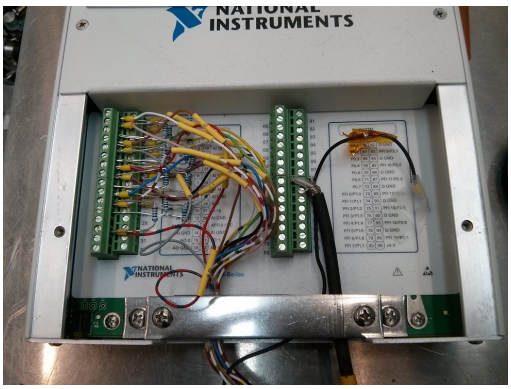

(a) NI USB 6221

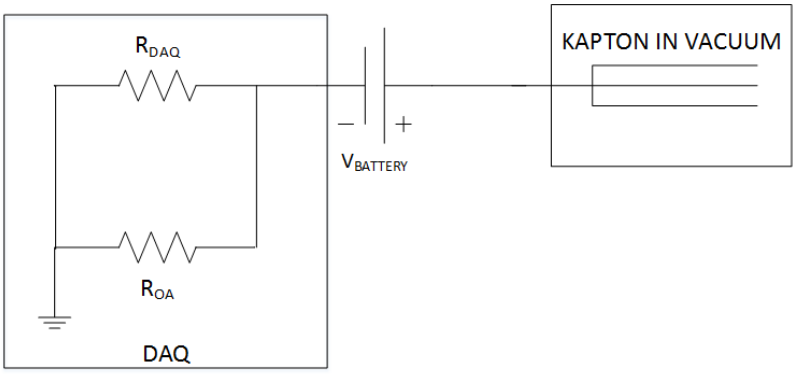

(b) Electrical Scheme

Figure 5.21: a: DAQ used during the experiments. b: Electrical scheme of an EC-monitor channel, R_{DAQ} is the resistor on which flows the multipacting current and R_{OA} is the resistor of the operational amplifier of the DAQ.

The parallel resistors in figure 5.21 -b are R_{DAQ} and R_{OA}, respectively the resistance on which flows the current induced by the multipacting electrons and the impedance of the operational amplifier.
To obtain reliable results, it is necessary $R_{DAQ} << R_{OA}$, this condition implies that $I_{multipacting}$ tends to flow mainly on R_{DAQ} with minimal losses, equation 5.3.

$$I_{DAQ} = \frac{I_{multipacting}}{(1 - \frac{R_{DAQ}}{R_{OA}})} \tag{5.2}$$

$$V_{DAQ} = R_{DAQ} \frac{I_{multipacting}}{(1 - \frac{R_{DAQ}}{R_{OA}})} = V_{OA} \tag{5.3}$$

If the condition above is respected, $I_{DAQ} \simeq I_{multipacting}$, 5.2.
Since the two resistors are parallel, $V_{DAQ} = V_{OA}$ and the the second term of the

equation is the signal reported by the operational amplifier of the DAQ and sent to the computer, figure 5.22.

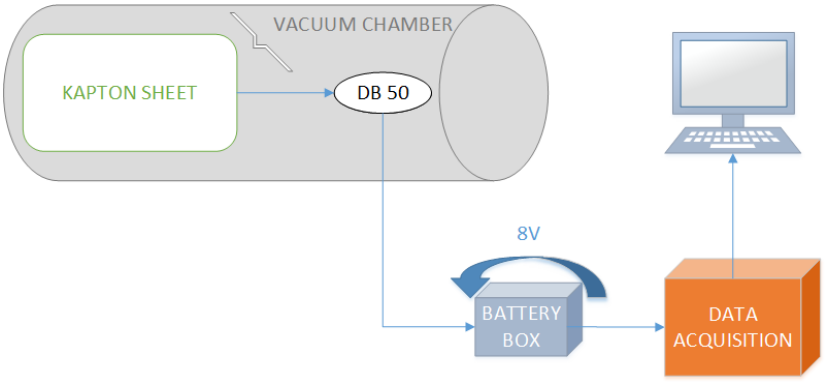

Figure 5.22: The block scheme reproduces the data acquisition procedure of the multipacting current in the MDHW dipole test-bench. The kapton strip detector attracts the electrons and induces a potential difference on the resistors of the DAQ. The potential reading is sent to the computer for the analysis.

The computer receives the potential signal from the DAQ and acquires it through the LabVIEW® program for the multipacting.
It is necessary to underline that the DAQ operational amplifier sequentially acquires the signals across the channels.
This sequential acquisition procedure introduces a second requirement: the acquisition rate must be slow enough to allow the discharge of the amplifier before starting acquiring the next channel.
If this condition is not fulfilled the readings are characterized by the channel-ghosting, which induces a false potential reading on the adjacent channels.
During the experimental tests the acquisition rate is $1Hz$ over all the 16 channels, the reading switches between two adjacent channels is $1/16Hz$, low enough for the stability of the operational amplifier.
The voltage readings of the computer can be related to the multipacting current, since $I_{DAQ} = \frac{V_{DAQ}}{R_{DAQ}} \simeq I_{multipacting}$.
Usually $R_{DAQ} = 1k\Omega$ and $1V$ in the acquisition data corresponds to $1mA$ flowing through one channel of the e-cloud monitor.
Consider an acquisition interval of length Δt with an acquisition rate t_i^{-1}, it is valid the relation $\Delta t = \sum_i t_i$.
Then, approximate the current between two acquisition points t_i and t_{i+1} as constant and equal to $I_{multipacting}(t_i)$.
From these assumption is possible to estimate the number of Coulombs flowing trough a channel "n" of the kapton sheet, equation 5.4.

$$C_n(\Delta t) = \sum_i I_n(t_i) * t_i \tag{5.4}$$

With I_n expressed in Ampere, A, and t_i in seconds, s.
The acquisition channels are composed by groups of Cu stripes of the e-cloud

monitor, considering the geometry of each stripe it is possible to extrapolate the electron dose, $D_{monitor}$ (C/mm^2), that impinges on the monitor during an acquisition interval Δt, as expressed in relation 5.5.

$$D_{monitor} = \sum_{n} \frac{C_n(\Delta t)}{A_n} \tag{5.5}$$

A_n is the conductive surface of a generic channel n, equal to the sum of the surfaces of the Cu stripes that compose the channel, it means:

$$D_{monitor} = (\sum_{m=1}^{m=15} \frac{C_m}{[(3 * w) * L]}) + \frac{C_{16}}{[(2 * w) * L]} \tag{5.6}$$

Where w and L are the width and the length of a Cu stripe.
Further, consider that the electrons impinging on the kapton sheet are only a small fraction of the ones generated by the electron cloud within the liner during the multipacting.
Since the liner has a transparency of 7%, the relation 5.7 expresses the dose received by the liner surfaces.

$$D_{liner} = D_{monitor} * \frac{1}{0.07} \tag{5.7}$$

The e-cloud monitor and its electronic devices are able to extrapolate the electron dose which develops during the multipacting. The study of the cumulative dose received by the surfaces of the liner during long lasting tests is of primary importance in studying the electron conditioning of a surface.

5.7 Multipacting data acquisition

Once the resonance frequency has been chosen, the VNA is used to develop power ramps into the systems.
The amplifier enhances the signal of the VNA toward the wire, the resulting field increases during the power ramp up to a threshold level above which either the primary and secondary electrons are energetic enough to start the multipacting.
Once the elctron-cloud builds up into the resonator chamber, several mechanisms are activated.
In the SPS dipole test-bench no e-cloud monitor is available.
The evidences of the multipacting are the ESD and the "detuning" of the resonator.
The ESD is the consequence of the energetic electrons impingement on the resonator walls, the adsorbates receive enough energy to desorb and the pressure of the system increases.
The pressure rise is dependent on the surface status either in terms of adsorbates composition and conditioning.
If the surface is rich of adsorbates, once the e-cloud develops, it is easier to free a larger amount molecules.
On the other hand, the conditioning state of the surface determines the efficiency

of a primary electron in extracting secondaries, it means that a conditioned surface reduces the generated secondaries during the multipacting and less electrons are available to remove the remaining adsorbates.
So, during long lasting consecutive multipacting tests the maximum pressure rise decreases because of the combined effects of the surface cleaning and surface conditioning.
Even the "detuning" of the resonator is a consequence of the elctron-cloud.
The formation of a space charge modifies the distribution of the electric field inside the resonator, the result is a variation in the coupling conditions of the RF resonator.
It means that the same frequency can stand inside the system in absence of the e-cloud, but once the charges fill the resonator they modify the electric field in such a way to operate a sort of shift in the coupling frequency of the system.
Practically, it is the result of a first energy feeding of all the electrons inside the resonator, which start the multipacting.
Then, the electron cloud develops up to a level of space charge limit unable to receive further energy from the system.
As a consequence, the RF signal transmission is modified as the amount of transmitted power.
In the MDHW bending dipole test-bench is installed even the e-cloud monitor. As the multipacting starts, the electrons developed in the chamber escape the liner through its holes, figure 5.20, and reach the strip detector on which develop a current that produces a voltage signal on the DAQ.
To control the behavior of the multipacting, it is necessary to keep track of all these reactions.
Firstly, the "detuning" of the RF resonator is recorded by the VNA embedded software.
The VNA records and shows the track of the power output on power input ratio, figure 5.23.
As long as the parameters of the resonator aren't affected by the e-cloud, the maximum power transmission is fixed in the system. So, increasing the output power of VNA will increase proportionally the reflected power and as a consequence the power ratio is constant.
As the multipacting develops and the resonator frequency shifts, the maximum power transmission changes as the ratio read by the VNA.
The figure 5.23 shows an example of the typical real-time plot that builds on the VNA screen during a multipacting test.
The signals of either the gauge and the DAQ are acquired by a computer.
The computer is provided of the National Instruments LabVIEW® 9.
The software allows to write a block diagram for the real time acquisition and conversion of analog signals, the DAQ is connected via USB port and the gauge is firstly connected to its controller and then to the computer via an RS232 port.
The software is written even to trigger the power ramps of the VNA so to synchronize all the acquisition systems.
In its original version the user interface shows the total current development, the current distribution across the single channels and the pressure development during the power ramp, figure 5.24.

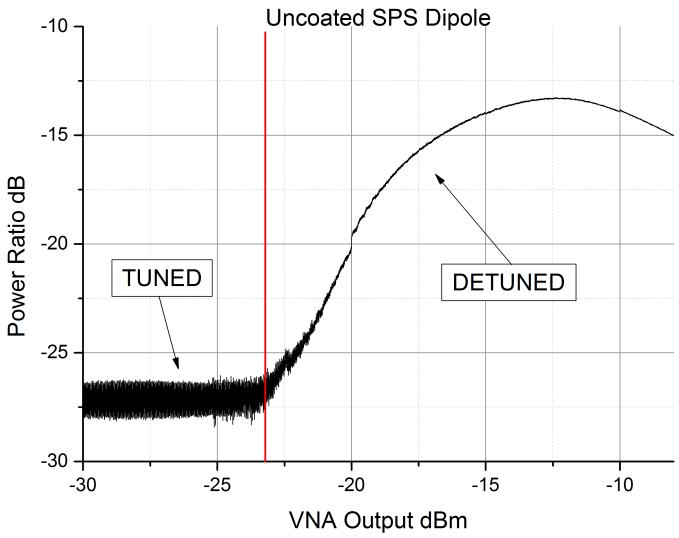

Figure 5.23: Example of the signal recorded by the VNA during a power ramp in the SPS dipole.

In the right-up corner the red box evidences the commands list to regulate the DAQ signal acquisition, the number of channels, the sampling rate and the measurements length.
In the yellow box, down left corner, there are the controllers of the pressure gauge: the sampling rate and the measurement length boxes.
In the right corner, down, the green box contains the controllers for the VNA and the automation of the measurements.
From the commands in the green box, it is possible to set the number of iterations and the repeating rate, it means that the controller triggers the VNA power ramp and the acquisition from the DAQ and the gauge.
The LabVIEW® program is written to perform automatically a user defined number of power ramps, or shots, which restart after an interval of time defined by the command "seconds".
In practice, every n seconds the program triggers the VNA to start a shot that lasts m seconds, in the meanwhile the acquisitions from the DAQ and the gauge start and lasts an interval of time j defined by their respective controllers, usually $j = 30s$ and $n = 120s$.
So, the power ramp increases the input power along the interval of time j trying to develop the multipacting. During the time $x = n - j$ the systems recovers before the program triggers again the VNA and the acquisition systems.
The LabVIEW® program is extremely useful for the studies on conditioning since it is able to provide a series of consecutive shots along extended periods of time, with a frequency defined by the user and saving automatically the results.
The main limit of the set-up is that the VNA isn't able to save automatically its results. So, only the gauge and the DAQ data can be saved without the intervention of an operator.

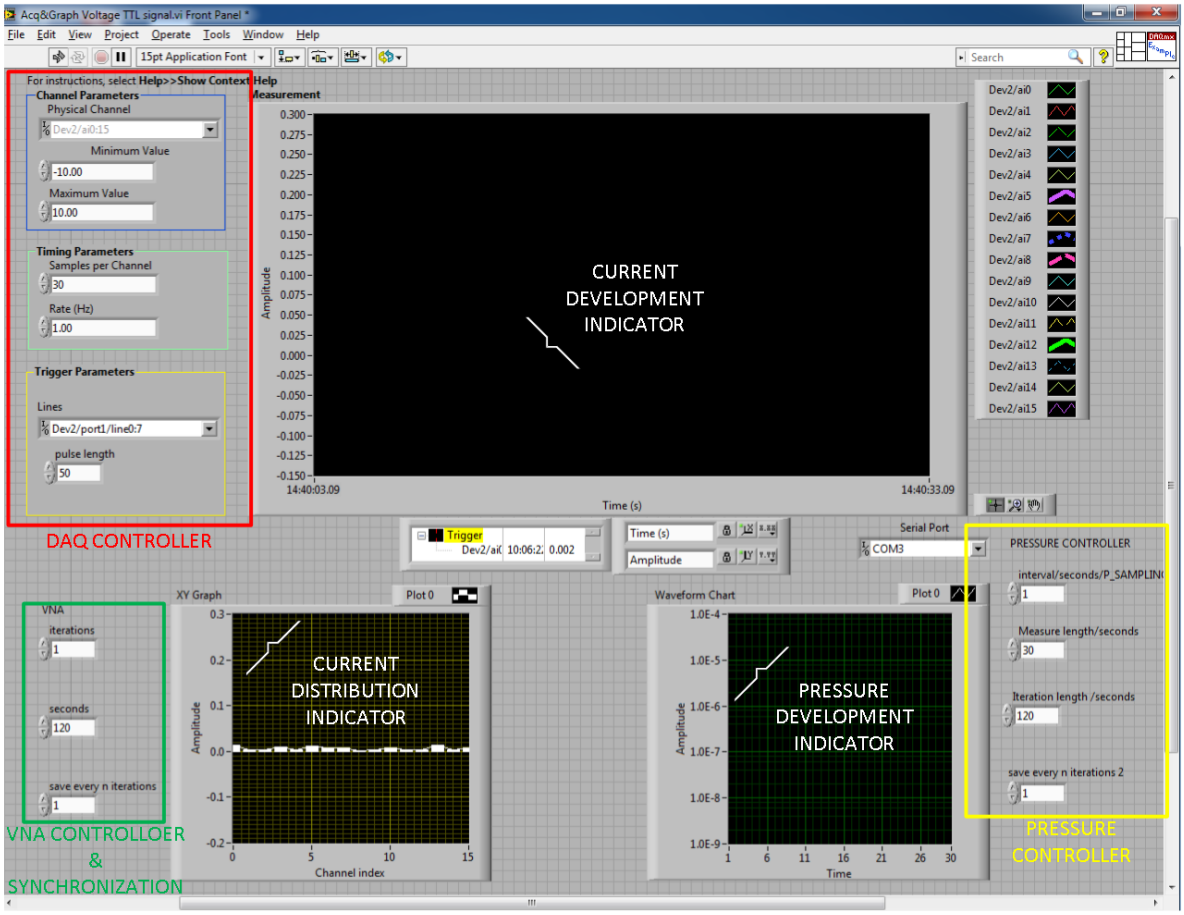

Figure 5.24: Labview multipacting acquisition program interface.

During the work a new gauss-meter has been bought: the Hirst Magnetic GM08. It can be connected to the computer to acquire the magnetic field value during the power shots.
A further version of the multipacting acquisition program inserted a block for the control of the gauss-meter via an RS232 port.
All the data are collected in ASCII files.
The data acquisition was performed by Matlab® codes, specifically written for the multipacting tests.

5.8 The XPS and the SEY analysis

The XPS, X-ray photoelectron spectroscopy, and SEY measurements are performed in order to study the chemical composition of a surface and its SEY.
In chapters 3, 2 were introduced the effects of the electron bombardment on a surface: the reduction of its δ_{max} as consequence of the modification of its status by ESD and surface graphitization.
Many conditioning tests have been performed along the present work and sometimes the experimental set-up was provided of samples which surfaces have been analyzed.
The XPS is based on the photoionization of a solid and uses the energy distribution of the out-coming electrons to define the composition and electronic state of a sample.
An X-ray source emits a monochromatic light of energy $E = h\nu$, the typical source is MgK_α with a radiation energy of $h\nu = 1253.6eV$, [35].
The photon hits and crosses the first atomic layers of the target, the energy of the radiation is high enough to ionize the core levels of the sample which emits electrons with a very short mean free path inside the material, equation 5.8 [21].

$$h\nu = E_K - BE - \phi \tag{5.8}$$

Where E_K is the kinetic energy of the escaping electron, BE the binding energy of the core level and ϕ the work function of the solid target.
Each element is provided of its specific core levels to which specific BE are associated, it means that any element has its own XPS energy peaks: its identification fingerprints.
In a complex system composed of more than one element, the intensity of the peaks is an indicator of the concentration of a specie.
A key-point of the XPS analysis is the sensitivity to chemical shifts.
A chemical shift is a core level energy modification. Oxidations and bonds shift the position of the peaks in a degree more or less pronounced according the effects on the electronic structure of an element.
This feature is relevant in the identification of the hybridization states of the carbonaceous layers which form on a target during the conditioning experiments.
The amorphous carbon is the most effective carbon structure in reducing the SEY of a surface, the XPS is able to identify the degree of amorphous carbon and generally the degree of sp^2 and sp^3 hybridized atoms, figure 5.26.

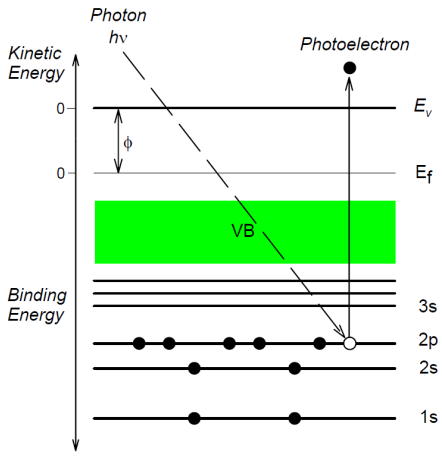

Figure 5.25: Photoelectron extraction [44].

The deconvolution of the $C1s$ peak highlights the presence of two distinct contributions separated by $0.7eV$.
The lower energy peak marks the sp^2 hybridization, the higher peak corresponds to the sp^3 one [27].
Such a distinction is possible knowing the spectra of the C peaks and even comparing the carbon peaks of the target with the spectra of an $HOPG$ sample.

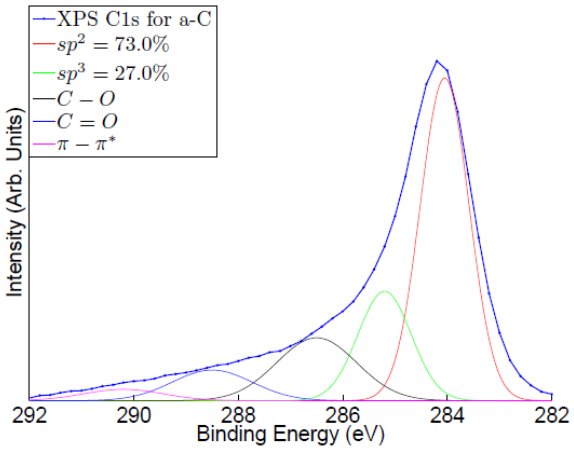

Figure 5.26: C1S XPS peak composition of an a-C coating [59].

A schematic view of an XPS is shown in figure 5.27, the vacuum firstly keeps the surface free from the contaminants that would modify its composition, then it improves the mean free path of the extracted electron which move toward the electronic energy analyzer where their energy is detected and used to characterize the surface.
In the CERN set-up the XPS is directly connected to the SEY test-bench.
The specimen is transferred from one to the other through a mechanic arm and is not necessary to break the vacuum to perform the analysis one after each other.

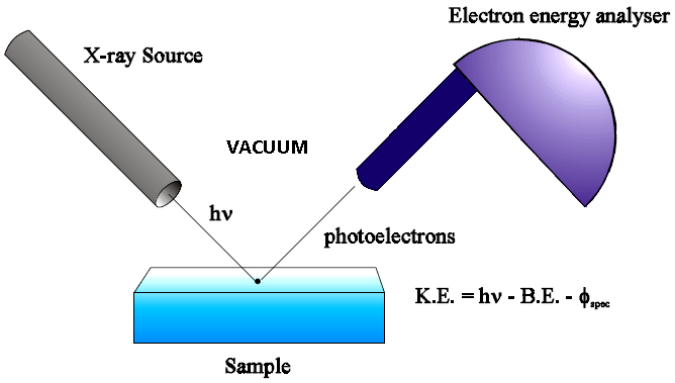

Figure 5.27: The picture shows the main components of an XPS, the orientation of the X-ray source and of the electron energy analyzer influence the sensitivity and resolution of the instrumentation [44].

The SEY measurements are performed by an electron gun that irradiates the target with a monochromatic beam.
The secondary electron yield curve of a sample determines the number of secondaries extracted per impinging primary.
The sample is negatively biased to repel the escaped electrons, while a collector is positively biased to attract the outcoming secondaries, figure 5.28.

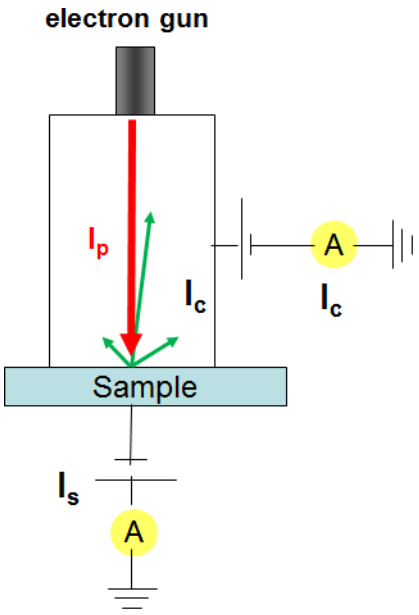

Figure 5.28: In the present picture is shown the basic functional mechanism of an SEY measurements test-bench, where $\delta = \frac{I_c}{I_c+I_s}$ [49].

In the conditioning tests it is extremely useful to measure the SEY of a sample and compare it to its uncoditioned value, it can show the real effects of the conditioing and the maximum reduction of the SEY of a surface in different conditions, such

as coated or uncoated.
The experimental set-up used at CERN for the analysis of the samples is shown in picture 5.29.

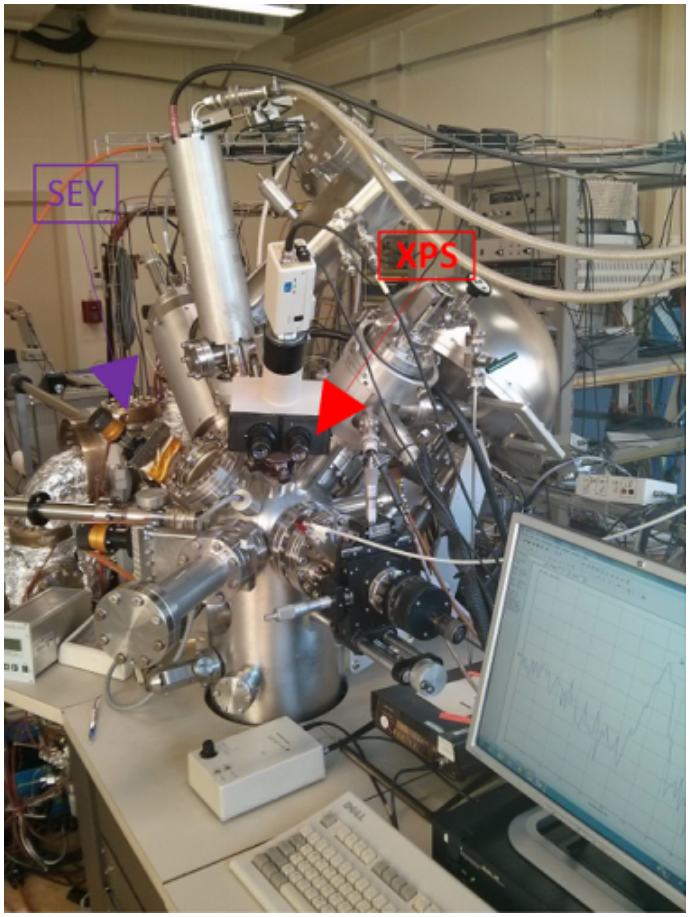

Figure 5.29: XPS and SEY test-bench at CERN.

The sample is inserted from a special port which connects both the benches. The SEY is measured first, to avoid any modification due to the photon irradiation by the XPS source.
It is important to underline how the exposure of the sample to the electron gun must be limited and controlled, otherwise there is the risk of electron conditioning the surface and grow a graphitic layer influencing the SEY of the sample.

Chapter 6

SPS Dipole Test-Bench: Experimental Results

6.1 Uncoated MBA dipole chamber

An MBA SPS dipole has been tested.
The first experiments have been performed on its $StSt$ uncoated chamber.
The set-up was assembled inserting a W wire of about $7m$ inside the MBA chamber, it was short-circuited to the dipole's terminal flange on one side.
The pre-chamber has been located to the other extremity of the dipole and connected to the W wire.
To develop the magnetic field an high-voltage DC power supply was connected to the SPS dipole.
The RF output of the pre-chamber has been linked to the RF set-up up to develop the AC electric field, figure 6.1.

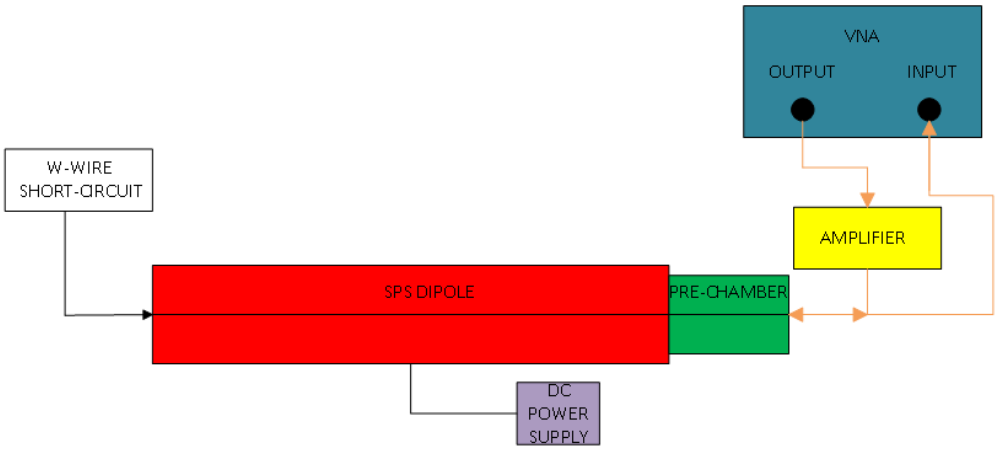

Figure 6.1: SPS experimental test-bench block scheme

The system has been pumped down to about $6.7 * 10^{-7} mbar$ in 48 hours.
The VNA scanned the resonance frequencies of the MBA chamber between $20MHz$ and $220MHz$, the chosen transmission valley lay between $148MHz$ and $151MHz$.

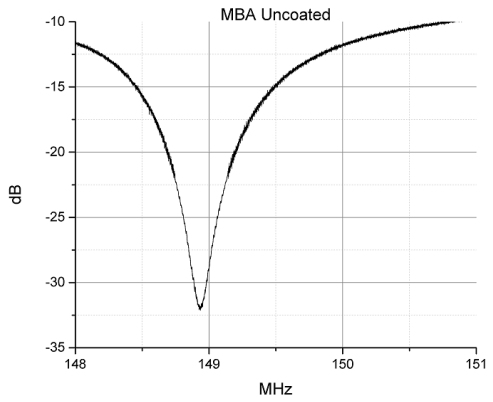

Figure 6.2: MBA uncoated transmission valley.

In picture 6.2 is shown one of the resonant peaks of the uncoated MBA resonator, the plot reports the value (VNA_{output}/VNA_{input}) expressed in dB.

$$VNA_{reading}(dB) = -20Log(\frac{VNA_{output}(W)}{VNA_{input}(W)}) \tag{6.1}$$

Since between the VNA and the RF input of the resonator is placed an operational amplifier, the power input at the chamber inlet is much higher than the VNA_{output} power.
The reflected power at the VNA_{input} is the amplified VNA_{output} less the transmitted component: the higher the coupling, the higher the transmission, figure 6.2.
Initially the working frequency has been chosen next to the resonance valley minimum at $149.0554MHz$, with the power coupling at $-25dB$.
It is worth to mention that, during the experiments, the transmission valley can slightly shift its position, this effect is due to the heating of the W, despite its highly stability the heat load can influence the W wire dimension and shifts the transmission modes.
The frequency shift, by the way, is extremely slight: it is in the order of $10^{-2}MHz$ to $10^{-3}MHz$.
Sometimes, to keep the the same power coupling during the tests, the chosen frequency is moved according the shifts of the resonant modes .
During the MBA dipole tests, in fact, the initial frequency has been set at $149.0554MHz$ and then moved to $149.0346MHz$ after few minutes from the beginning of the experiments.
The MBA experiments were performed to analyze the behavior of the multipacting with different magnetic field intensities.
Inside the SPS dipole is not possible to insert a gauss-meter, only the current provided by the DC power supply can be kept as reference for the magnetic field intensity.
After the frequency scan, the VNA is used to stimulate the multipacting inside the dipole through an RF power ramp (or shot).
Inside the MBA dipole, the VNA_{output} spanned from $-30dBm$ to $-8dBm$, so from

about $2W$ to $20W$.
The power ramp has been set along 10^4 points in $10s$.
The magnetic field intensity was varied controlling the DC power supply current output, from $0A$ to $400A$.
During each shot the magnetic field was kept constant.
Three shots per each value of the magnetic field have been performed.
As introduced in chapter 3, the MBA geometry is less prone to develop multipacting with respected an MBB chamber, it means that for the same conditions it is required more energy to induce the e-cloud development in the dipole section.
At $0A$ the magnetic field is far from the cyclotron resonance condition with the AC electric field.

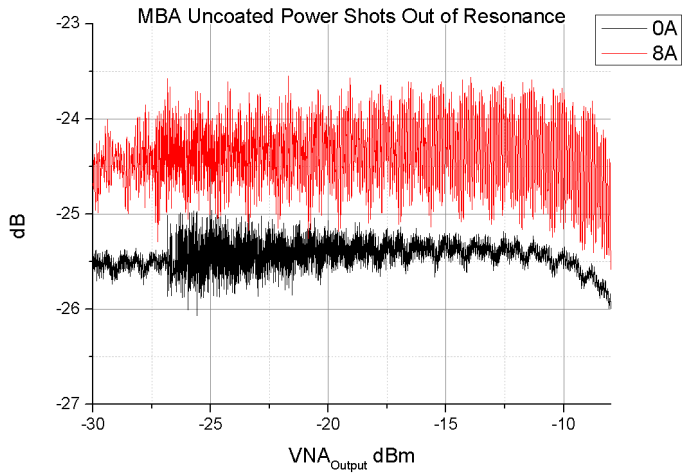

Figure 6.3: MBA power ramps out of cyclotron resonance. It makes the electric field ineffective in stimulating the multipacting inside the chamber.

Up to $8A$ the multipacting doesn't start, this effect is clear either from the VNA power ratio and the pressure gauge readings.
The lack of the multipacting keeps the power ratio tuned at the same value across the whole power shot, figure 6.3.
Even the gauge controller shows no pressure increase, it means no ESD phenomena.
It is worth to mention the plotted power ratio doesn't appear as a perfect line, this effect is due to small RF fluctuations which affect the instant position of the the transmission valleys.
Further, the final parts of the curves appear to bend downward, such a fluctuation in the power ratio is ascribed to the compression effect of the amplifier.
At high power the amplifier looses of linearity causing the deflection in the plot.
Increasing the current from the DC power supply, the magnetic field intensity gets closer to the cyclotron resonance condition.
As a result, the multipacting develops and the effects on the system are the detuning of the RF coupling with a huge variation of the power ratio and further is recorded an high pressure increase ascribed to the ESD.

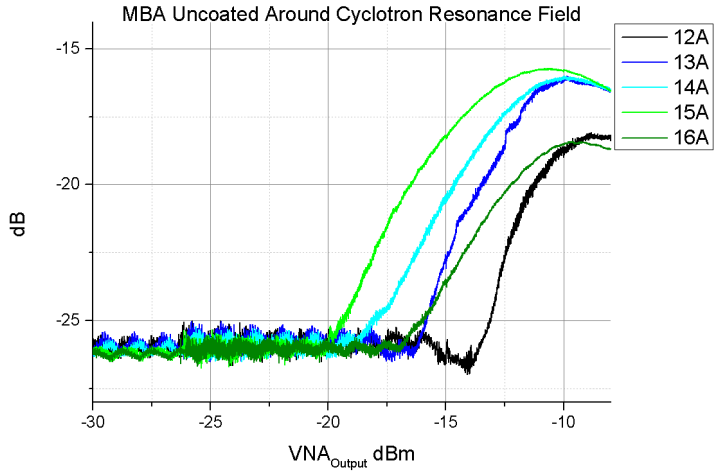

Figure 6.4: MBA power ramps around the cyclotron resonance. Once the VNA_{Output} provides enough power to start the multipacting, the RF detunes from its initial coupling level.

$\vec{B}$ field (A)	12A	13A	14A	15A	16A
P_{max} (mbar)	$3.5 * 10^{-6}$	$7.9 * 10^{-6}$	$1.0 * 10^{-5}$	$6.4 * 10^{-6}$	$4.2 * 10^{-6}$

Table 6.1: MBA uncoated ESD induced pressure peaks.

The VNA readings suggest the resonance conditions are achieved at $15A$, since the multipacting develops at the lowest value of VNA_{output} power, figure 6.4.
Increasing further the magnetic field intensity, the resonance condition is lost again and the energy required to develop the multipacting increases.
Above $16A$ the effect of the magnetic field gets less and less effective.

$\vec{B}$ field (A)	20A	50A	100A
P_{max} (mbar)	$1.6 * 10^{-6}$	$3.7 * 10^{-6}$	$7.7 * 10^{-6}$

Table 6.2: MBA uncoated ESD induced pressure peaks.

A further weak coupling between the magnetic and electric fields is evident again around $100A$.
That value of field is thought to be an integer multiple of the cyclotron resonant intensity, unluckily it isn't possible a direct measurement of the field value inside the dipole.
Increasing the current above $100A$, once again the multipacting gets weaker.

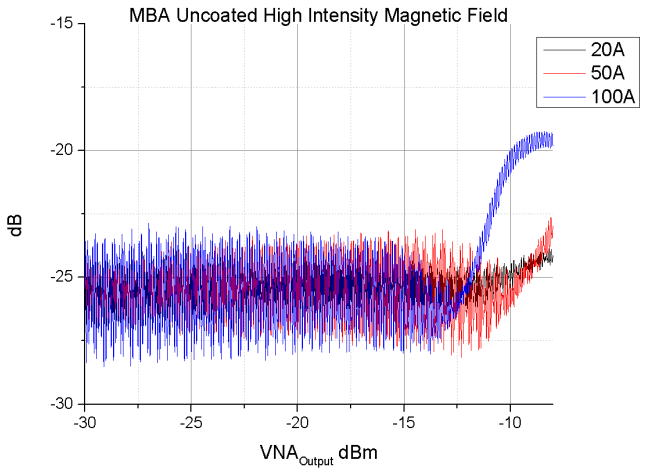

Figure 6.5: MBA power ramps out of cyclotron resonance. Higher field will require more energy to develop the multipacting.

6.2 Coated MBA dipole chamber

Amorphous carbon has been applied as low SEY coating on the *StSt* surfaces of the MBA dipole's chamber.
It works to suppress the multipacting development.
The coating is applied by means of Direct Current Hollow Cathode Sputtering (DCHCS), along two stripes on both the upper and lower surfaces orthogonal to the direction of the dipole's magnetic field, figure 6.6.

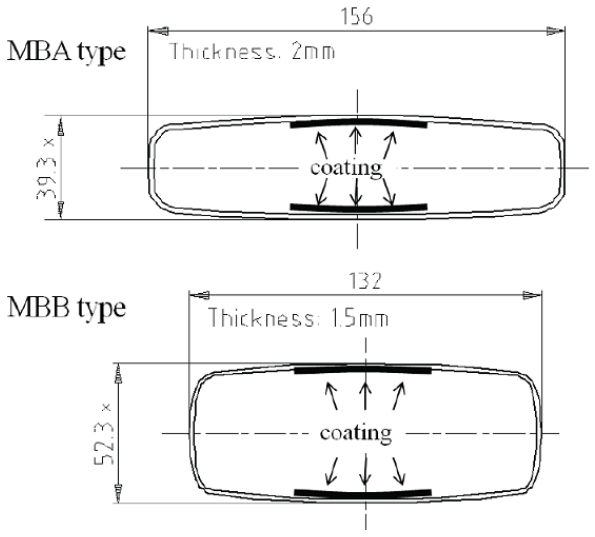

Figure 6.6: Carbon coating profile of the SPS dipoles chambers [13].

The test-bench has been installed again after the coating of the MBA chamber.
It has been prepared with the same set-up of the uncoated chamber.

The tests aim to verify the efficiency of the carbon coating in suppressing the multipacting.
Before the power shots the system has been pumped to $4.3*10^{-7}mbar$, the working frequency has been set at $148.6MHz$ and then moved to $148.255MHz$ to keep the initial coupling at $-25dB$.
For this reason the efficiency of the coating is clearer around the cyclotron resonance conditions.
It is worth to say that any shift in the working frequency implies a variation in the cyclotron field intensity, as $B \propto \nu$.

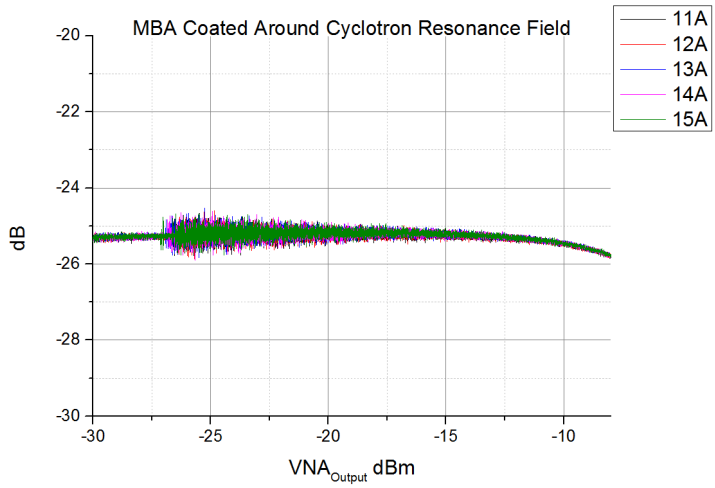

Figure 6.7: MBA coated power ramps in cyclotron resonance conditions.

$\vec{B}$ field (A)	11A	12A	13A	14A	15A
P_{max} (mbar)	$5.1 * 10^{-7}$	$5.1 * 10^{-7}$	$5.0 * 10^{-7}$	$5.0 * 10^{-7}$	$5.0 * 10^{-7}$

Table 6.3: MBA coated ESD induced pressure peaks.

From picture 6.7 it is evident how the carbon stripes suppress the multipacting development in such conditions where the bare $StSt$ surface is more prone to emit secondary electrons.
The plot shows a downward bend for the highest power input range. The operational amplifier used on these tests was the same installed for the MBA uncoated test-bench, its loss of linearity at high power causes the deflection.

6.3 Uncoated MBB dipole chamber

An MBB SPS dipole has been installed on the test-bench.
The set-up was the same of the previous experiments with MBA dipoles, but in this case the operational amplifier was different.
To maintain the same power parameters, it required to modify the VNA output range.
The power ramps ranged from $-30dB$ to $-11.5dB$ to keep the input power between $2W$ and $20W$, along $30s$ shots.
The short-circuit at the end of the system has been handled to move the resonance frequencies of the MBB chamber in the same range of the ones used in the MBA, it allowed to compare the behavior of the two systems in the same field conditions, figure 6.8.

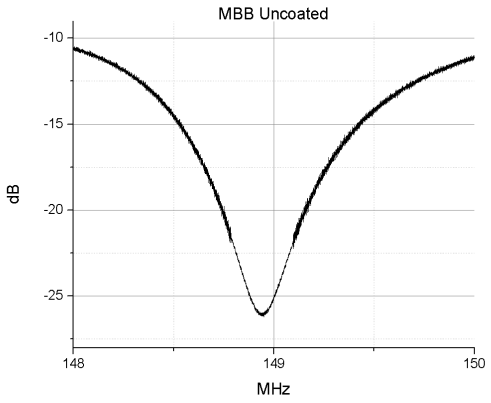

Figure 6.8: MBB uncoated transmission valley.

The working frequency has been initially set to $148.8646MHz$ and soon moved to $148.9362MHz$.
The system has been pumped to $8.1 * 10^{-7}mbar$.

$\vec{B}$ field (A)	0A	8A
P_{max} (mbar)	$8.9 * 10^{-7}$	$9.0 * 10^{-7}$

Table 6.4: MBB uncoated ESD induced pressure peaks.

Since the MBB geometry is more prone to develop multipacting even far from cyclotron resonance, the results of the experiments were expected to show the e-cloud build up in almost every conditions.
As figure 6.9 illustrates, the tendency to develop multipacting is low at low DC currents. The pressure peaks table confirms the tendency, with weak ESD pressure peaks.
Close to cyclotron conditions the multipacting develops at higher input power than what expected.

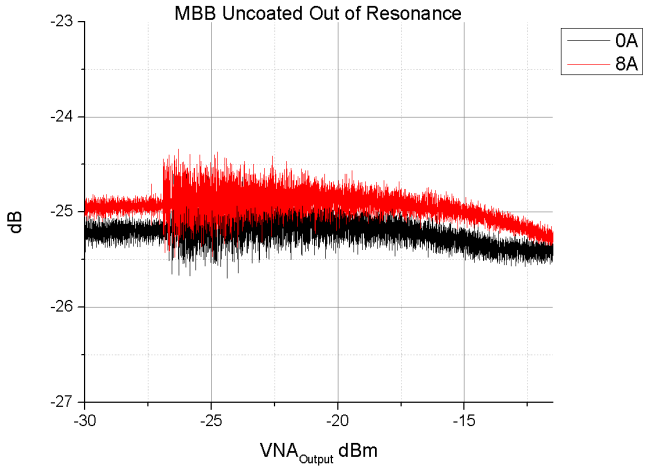

Figure 6.9: MBB power ramps out of cyclotron resonance. The results are in disagreement with the expectations.

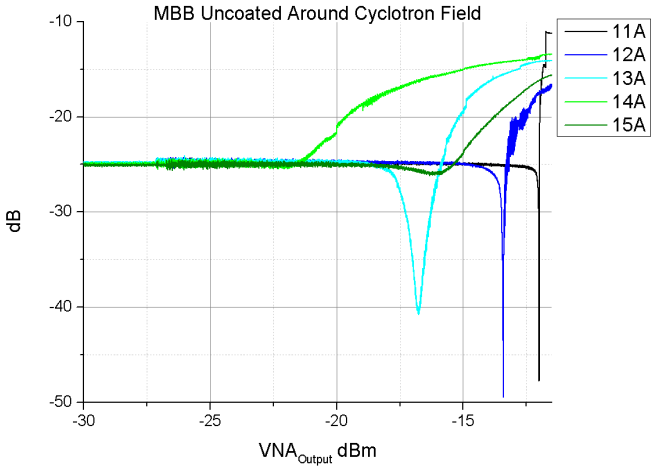

Figure 6.10: MBB power ramps close to cyclotron resonance. At such field intensities the chamber develops the multipacting.

$\vec{B}$ field (A)	11A	12A	13A	14A	15A
P_{max} (mbar)	$1.37 * 10^{-6}$	$7.77 * 10^{-5}$	$8.97 * 10^{-5}$	$1.23 * 10^{-4}$	$7.75 * 10^{-5}$

Table 6.5: MBB uncoated ESD induced pressure peaks.

Picture 6.11 shows the comparison between a previous experiment with an MBB chamber and the one performed during this work.
It is possible to observe how the MBB chamber adopted for the present work results less prone to multipacting.

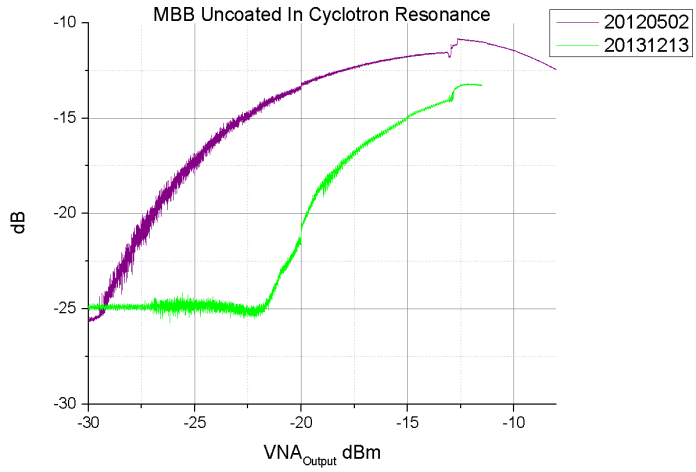

Figure 6.11: MBB chamber comparison. The purple line represents a spare MBB dipole used in 2012. The green one is the MBB used in the present work and coming from the SPS.

Date	20120502	20131213
P_{max} (mbar)	$1.1 * 10^{-4}$	$1.23 * 10^{-4}$

Table 6.6: MBB uncoated ESD induced pressure peaks. Both in cyclotron resonance conditions.

The 2012 MBB chamber shows a lower power threshold for the activation of the multipacting which seems to start almost immediately at the beginning of the power ramp.
The previous chamber, moreover, confirmed the expected high tendency to multipacting, showing the e-cloud build up even out of cyclotron conditions, figure 6.12.
The reasons for this unexpected behavior of the MBB chamber during the present experiments is not fully clear.
The main differences with the previous system lay in the history of the dipole.

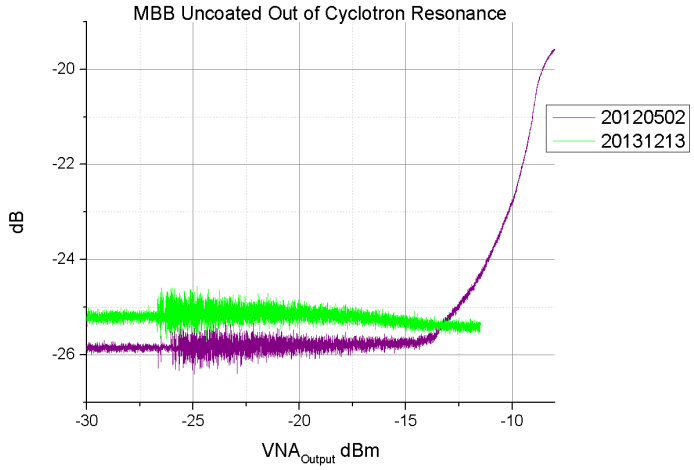

Figure 6.12: MBB uncoated chambers comparison out of resonance conditions.Both at 0A.

Date	20120502	20131213
P_{max} (mbar)	1.4^{-5}	$8.88 * 10^{-7}$

Table 6.7: MBB uncoated chambers comparison: ESD pressure peaks. Both at $0A$ magnetic field.

The MBB tested in 2012 was a spare dipole never used inside the SPS machine.
The dipole used in 2013, instead, has been installed inside the SPS accelerator and has been exposed to the particles beam, it means that it experienced the conditioning induced by the beam.
It showed strong traces of C, these are ascribed to the surface graphitization associated to the conditioning inside the accelerator.
For this reason, the dipole has been chemically cleaned before being used in the experiment, nevertheless it showed some C traces at the very beginning of the chamber, figure 6.13.
Actually it is unknown if these traces are enough to inhibit so strongly the multipacting.
Furthermore, the power amplifier has been substituted between the tests on the two MBB chambers, nevertheless the power ramps were kept at the same minimum and maximum values, which should have suggested similar behaviors.
In the upcoming months a new MBB chamber will be tested trying to clarify these discrepancies. The next chamber will be again a spare one unexposed to any particles beam.

Figure 6.13: Residual traces of C on the MBB chamber after cleaning, induced by the beam exposure.

Chapter 7

MDHW Dipole Test-Bench: Experimental Results

The MDHW test-bench has been prepared in several configurations.
It was used for the studies on the conditioning rates, the hydrocarbon enhanced conditioning and the pressure effects on the multipacting behavior.
The core of the set-up is the MBB profiled $StSt$ liner.
As introduced in chapter 5 the liner is inserted inside a cylindrical vacuum chamber to obtain an MBB shaped RF resonator.
The liner is provided of holes on one side with an electron transmission efficiency of the 7%, it means that only such percentage of the electrons can escape from the electron cloud through the liner's holes.

7.1 The liner effect on the multipacting

Before starting acquiring any signal from the multipacting, it was necessary to evaluate the perturbation effects of the liner on the electron cloud development.
The presence of the holes distributed on such a wide surface could have been a disturbance element in the behavior of the multipacting.
In the first step, the liner has been installed alone, without the e-cloud monitor, inside the vacuum chamber.
The aim was to record the multipacting behavior of the set-up across several magnetic field intensities.
The chosen working frequency was $142.338MHz$, the heating of the W wire caused no relevant frequency shifts and the working frequency has been kept constant along all the power shots.
For this set-up it was possible to insert a Gauss-meter to measure the magnetic field intensity, unfortunately its value was approximative.
The read values changed of few Gauss according the distance from the dipole's walls.
Nevertheless, using the cyclotron resonance equation it was possible to estimate a cyclotron field around $51G$.
It allowed reduce the candidate currents range of the DC power supply to provide the cyclotron conditions.

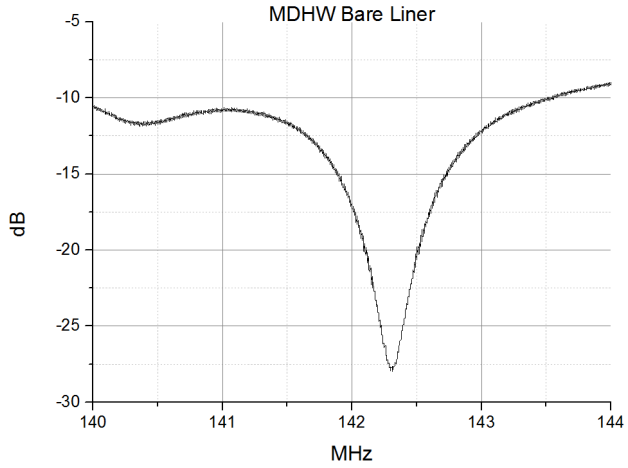

Figure 7.1: MDHW dipole transmission valley.

The shots were performed in currents ranges between $0.9A$ and $1.3A$, even few shots at $0A$ and at $I_{DC} > 1.3A$ were performed to control the correct reduction of the multipacting strength out of the cyclotron field intensity.
The system was pumped to $7.2 * 10^{-8} mbar$.

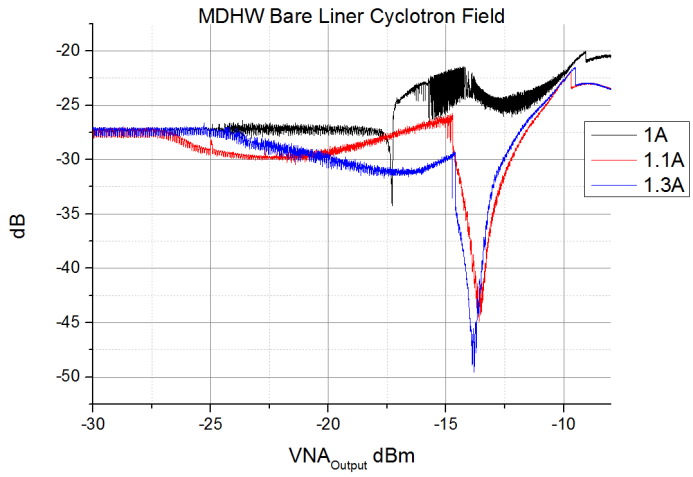

Figure 7.2: MDHW bare liner.

The sensitivity to the magnetic field is evident in the VNA readings, the activation threshold for the multipacting is highly affected by small shifts of the DC current value.
This phenomenon is less clear by the pressure peak readings, which lay in the same range across all the shots.
Afterwards, the same tests have been performed with a shutter installed on the liner's holes, to verify that the effect of the 7% holes transparency was negligible.

$\vec{B}field(A)$	1.0A	1.1A	1.3A
P_{max} (mbar)	$1.3 * 10^{-5}$	$1.3 * 10^{-5}$	$1.3 * 10^{-5}$

Table 7.1: MDHW bare liner ESD induced pressure peaks.

In this case the working frequency was shifted to $142.906 MHz$ and the system was pumped to $5.9 * 10^{-8} mbar$.

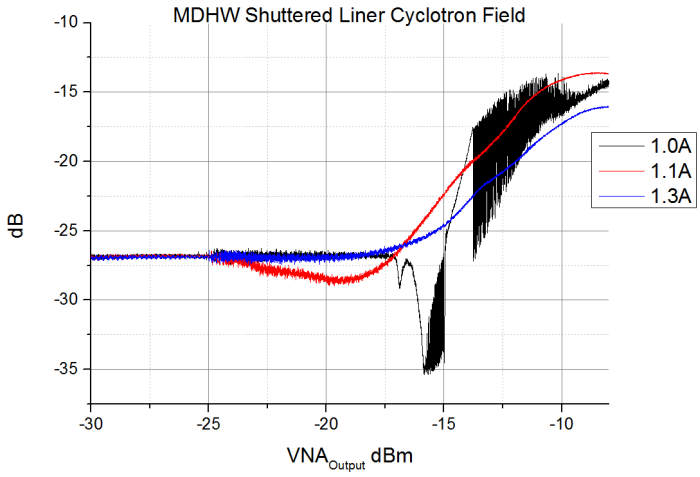

Figure 7.3: MDHW shuttered liner.

$\vec{B}field(A)$	1.0A	1.1A	1.3A
P_{max} (mbar)	$8.6 * 10^{-6}$	$1.5 * 10^{-5}$	$1.0 * 10^{-5}$

Table 7.2: MDHW shuttered liner ESD induced pressure peaks.

Comparing pictures 7.2 and 7.3, it is possible to observe a slight difference between the bare and shuttered configurations, especially according to the threshold power for the activation of the multipacting.
Even the maximum reflected power difference lays in the order of few dB variation, such a difference can be related either to the shutter or to the experimental conditions.
Nevertheless, it was concluded that the influence of the liner holes on the multipacting development is negligible.

7.2 The influence of the magnetic field

The further step has been the installation of the e-cloud monitor. Before, the liner has been previously chemically cleaned to restore its surface properties.

The bench has been provided of $R_{DAQ} = 1k\Omega$ resistors, and $9V$ batteries at the battery box.
The channel disposition on the strip-detector allows to measure the current distribution across the surface of the liner and orthogonally to the Cu strips, figure 7.4.

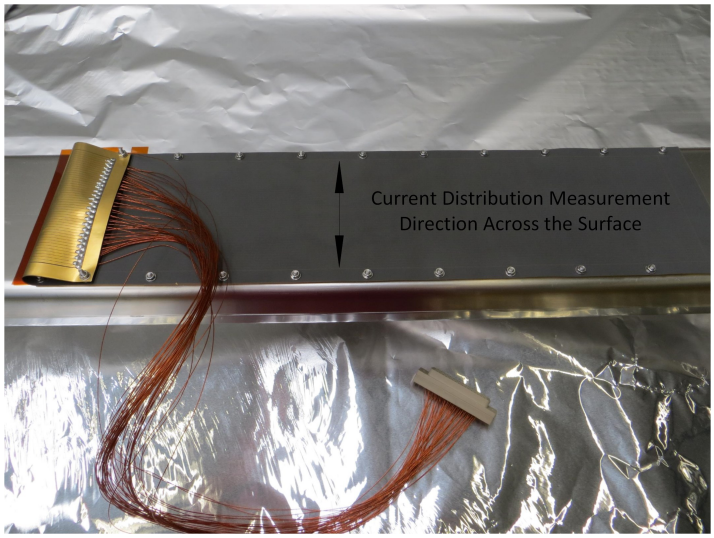

Figure 7.4: The current is measured along the chamber axis, its distribution can be resolved in transverse direction.

The first tests aimed analyzing the effect of the magnetic field intensity on the current behavior.
In chapters 6 and 7 it was shown the influence of the magnetic field on the multipacting via the cyclotron resonance coupling between the RF electric field and the magnetic one.
Approaching the resonance, the power threshold for the activation of the multipacting reduces.
Another effect revealed to be the difference in the current distributions along the channels in magnetic regions which intensities lay below and above the cyclotron field.
For these shots the VNA was set-up to work at $142.1343MHz$, the cyclotron magnetic field intensity at this frequency is about $50.7G$.
Figure 7.5 shows the current distribution in a magnetic field intensity just below the cyclotron conditions.
The electron-cloud current develops its maxima widespread on side channels as 5 and 12.
Increasing the magnetic field intensity by $\Delta(|B|) \simeq 1G$ the cyclotron condition is overcome, the electron cloud focuses on the central channel, it means on the central region of the liner, figure 7.6.
The magnetic field acts on the e-cloud shape inside the liner: below the cyclotron intensity the electrons widespread on the surface of the liner. Above the cylotron magnetic field, the electron cloud narrows around the central region of the liner surface.

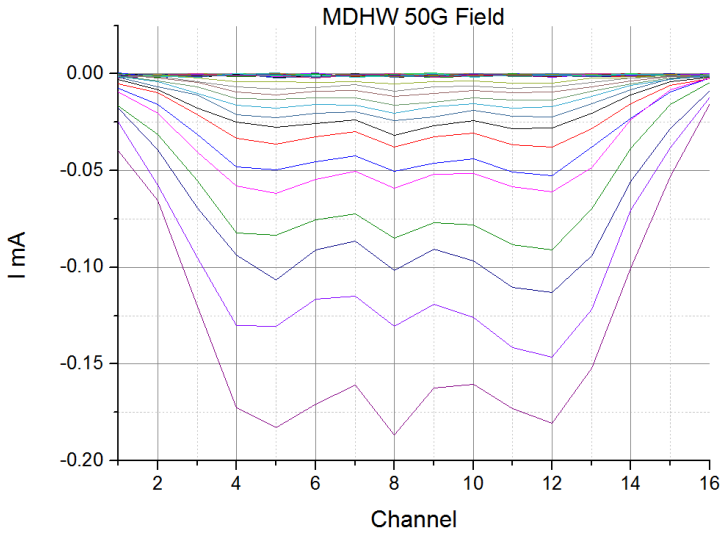

Figure 7.5: Below the cyclotron magnetic field intensity, the current is widespread aside of the central channel.

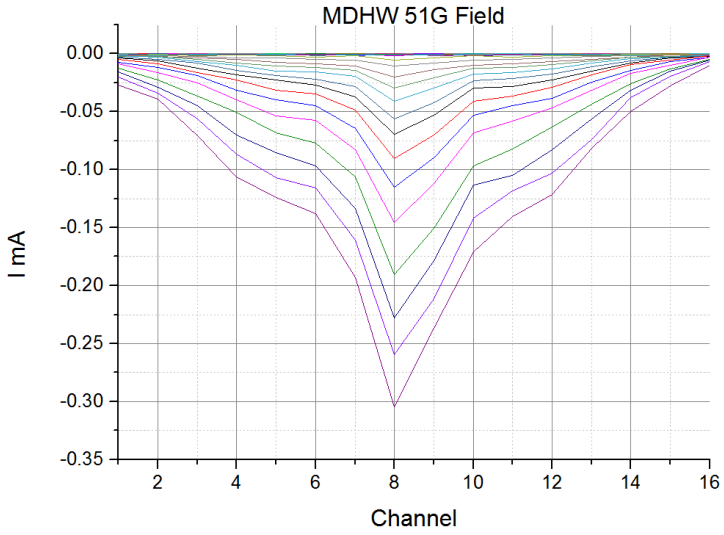

Figure 7.6: Above the cyclotron magnetic field intensity the current is focused on the central channel.

A similar behavior, as a function of the magnetic field, is observed in the pattern of the e-cloud induced by the SPS beam on the e-cloud monitors (figure 3.18) [28]. The lack of a real resonance condition in the SPS results is the main difference with the present experimental set-up .
It is worth to add that the liner's electrons transmittivity varies with the field intensity.
The electrons cyclotron orbits get smaller increasing the magnetic field intensity, up to the liner's holes dimensions. It results in a reduction of the transmitted electrons and a lower sensibility of the electron cloud monitor at high magnetic field intensities [56].

7.3 Conditioning tests

The test-bench can be programmed to work automatically, it allowed long lasting campaigns of power shots.
As long as the multipacting is continuously stimulated on a surface, the latter one gets conditioned. It reduces its tendency in developing the electron cloud.
It implies a reduction of the SEY, as a consequence of the surface cleaning from high yield contaminants (ESD), and further induces the surface graphitization.
Up to date it is unknown the efficiency of the multipacting electrons bombardment in reducing the SEY of a material, or better is not defined up to which level it is able to reduce the yield and how long it requires.
To fulfill the high luminosity task, the SPS will require an SEY at least below $1,3$ on the $StSt$ surfaces inside the unbaked SPS dipole bending sections.
During the present work the test-bench was prepared to simulate a conditioning campaign on that kind of $StSt$ liner.
The data reported below will show the results of the first campaign conduced.
Actually more than one campaign has been performed showing a very good reproducibility of the results.
The test-bench has been pumped in vacuum up to $7.7 * 10^{-7} mbar$, the VNA was prepared for $30s$ power shots with an output between $-40dBm$ and $-10dBm$; each power shot is separated from the next one by $120s$, it means a sweep every two minutes, with an initial RF coupling set at $-27dB$.
The working frequency has been set at $142.567MHz$ during the first campaign and always around this frequency on the others, the cyclotron field is around $51G$.
To avoid any variation induced by field instabilities, the magnetic field has been set at $49G$, it implies the DC power supply output set just below $1.1A$.
Figure 7.7 shows the first evidence of the conditioning.
The plot contains the values of the maximum current registered on the e-cloud monitor as a function of the cumulative dose.
The cumulative dose is the sum of the electron doses across all the shots 7.8. A smaller SEY results in a lower tendency of the surface in emitting secondary electrons, it weakens the electron cloud.
As a consequence it reduces the number of electrons collected by the monitor.
Concerning the current reduction, it is interesting the study of the principal channels behavior, figure 7.10.

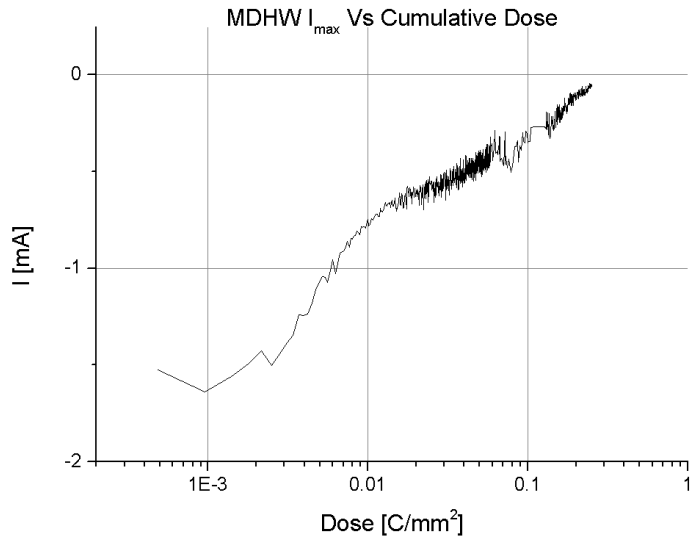

Figure 7.7: The electron cloud current reduces as a consequence of the conditioning, the value is expressed as a function of the cumulative dose.

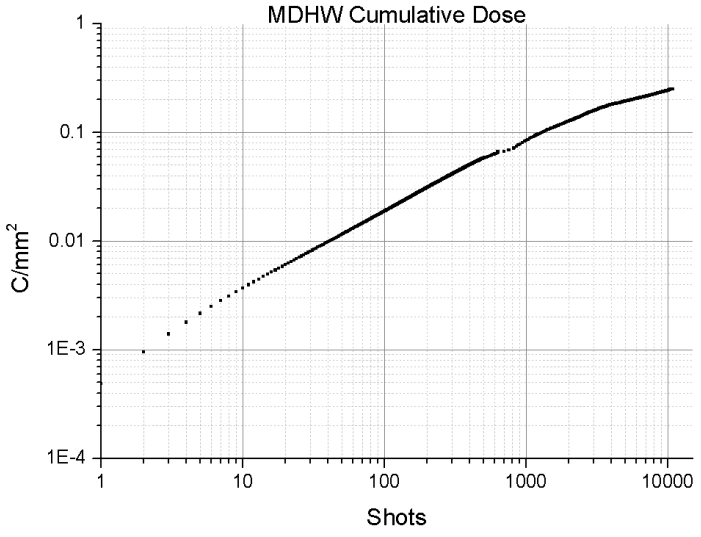

Figure 7.8: MDHW Dipole cumulative dose along the shots. The dose is calculated over the area of the $47Cu$ stripes: $2mm$ width, $378mm$ length.

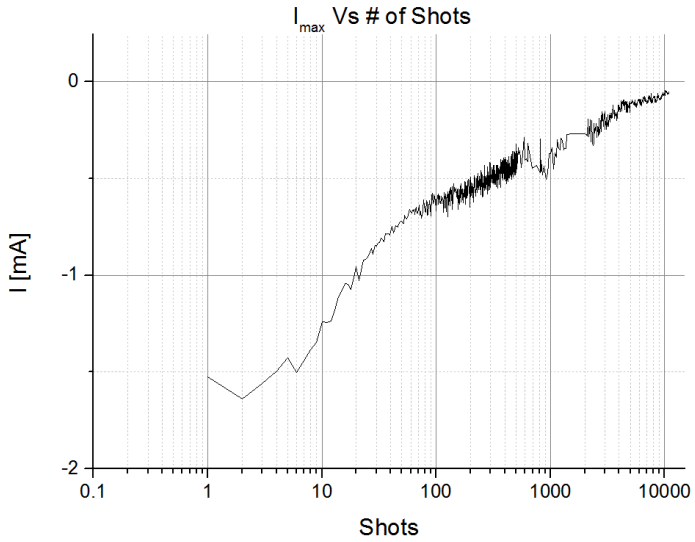

Figure 7.9: The electron cloud current reduces as a consequence of the conditioning, the value is expressed as a function of the number of shots.

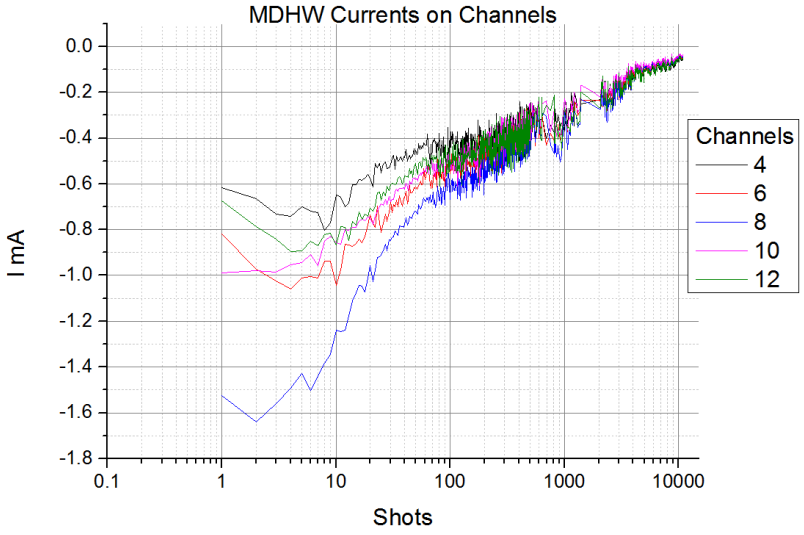

Figure 7.10: The electron cloud current reduces faster on those channels exposed to a stronger multipacting electron bombardment.

The magnetic field intensity has been set below the cyclotron value, it means a widespread current distribution on the first channels around the central one.
During the conditioning experiments these channels are exposed to higher currents with respect their neighbors, the corresponding surface sections are exposed to a stronger electron bombardment.
It results in a faster conditioning of these channels, as shown in picture 7.10.
Figures 7.7, 7.10 and 7.9 underline a first important evidence of this set-up: the current reduction along the cumulative dose (and consequently the shots) has a logarithmic-like behavior.
It is extremely fast in the first part of the curve and reaches a plateaux along which the rate of conditioning slows down and the current values tend to get almost constant.
It means that, if the requested SEY has not been reached before the plateau, the conditioning will require an unacceptable time to reduce further the surface yield.
The XPS and SEY analysis showed that beyond the extreme current reduction and the high cumulative dose, the surfaces of the samples inside the test-bench had still an high SEY: above 1.8 (measured after air exposure), higher than the one required by the SPS applications, figure 7.11-a.
Nevertheless, the XPS analysis after a conditioning campaign underline a carbon content around 60%, figure 7.11-b.
The carbon signal is above the average but is much lower than the content attained with the electron-gun, around 90%.
It means the samples haven't been fully scrubbed. Moreover, their high SEY value can be ascribed either to the air exposure and to a non graphitic-like carbon deposition on their surfaces.
Unluckily the air induced contamination erased any possibility of distinguishing the carbon hybridizations.
These results imply, firstly, the inefficiency of the set-up in completely suppressing the multipacting.
This can be ascribed to the electrons energy inside the test-bench, since the conditioning efficiency against the dose is a function of their energy, as shown in chapter 2.
This option has not been confirmed along the experiments as the energy distribution inside the chamber was unknown.
On the other hand it is possible to affirm that the beam conditioning will have the same logarithmic behavior even inside an accelerator, it remains to clarify if it is fast enough in reducing enough the SEY before its plateau.
The second evidence of the conditioning is the ESD reduction.
During the first shots the pressure increase is extremely high, that is a consequence of the high amount of species desorbed from the surface.
Proceeding with the power shots, the surface is cleaned and the pressure peaks decrease their intensity, figure 7.12.
As the electron cloud gets weaker: less and less electrons are available to desorb the adsorbates from the surface.
The residual gas pressure and composition are further points of interest for the comparison with the SPS behavior.
The experimental system is pumped down in the order of $10^{-7} mbar$, which is more

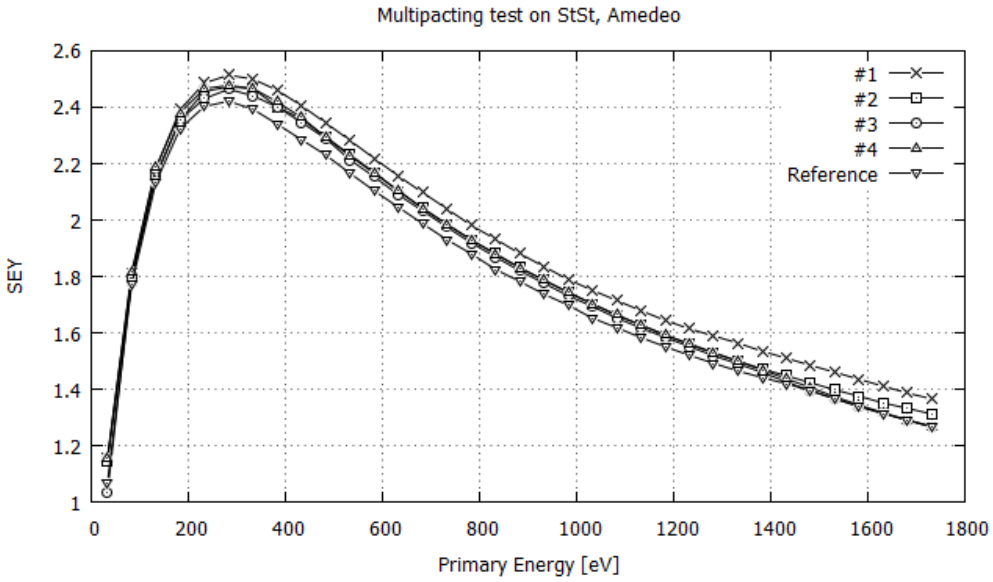

(a) SEY

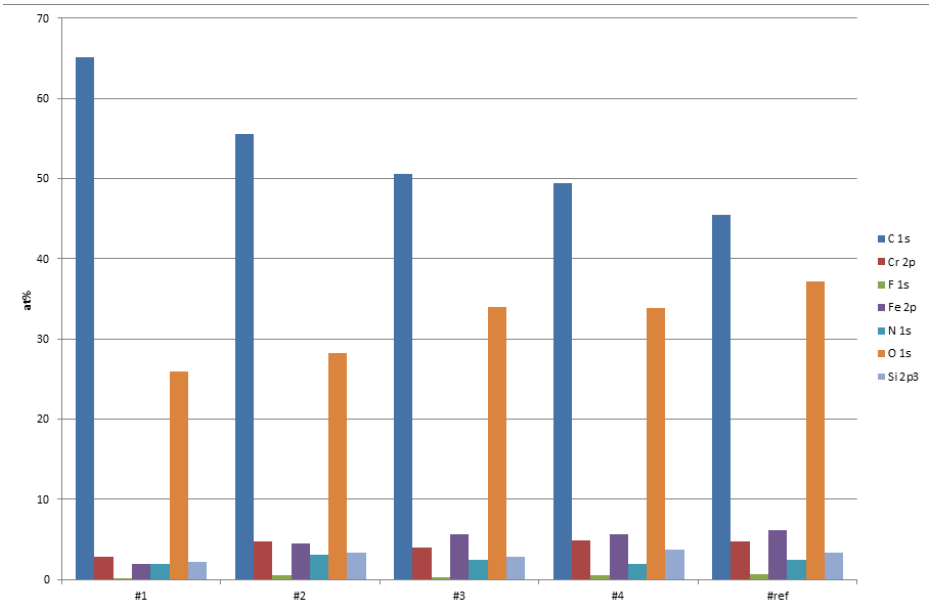

(b) XPS

Figure 7.11: MDHW Dipole sample SEY and XPS results.The sample has been cut firstly in two parts and further divided in four sections. Section 1 was placed at middle height of the liner, increasing the number the section position moves toward the liner's edge.

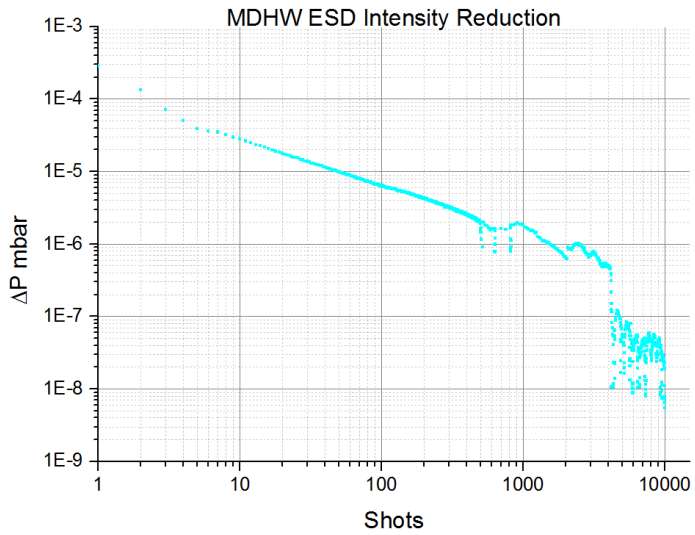

Figure 7.12: ESD reduction along the conditioning trials. The plot is expressed in terms of $\Delta P = P_{max} - P_{base}$, where P_{max} represents the maximum pressure reached along a multipacting shot and P_{base} is the pressure of the system before the multipacting development and after the recovering time from the previous shot.

than one order of magnitude higher than the SPS environment.
The gas composition, moreover, plays an important role in defining the adsorbates and their effect on the surface SEY.
Figure 7.13 shows an RGA scan of the system.
The residual gas shows the dominance of the water peaks and the presence of heavy contaminations.
The gas species with an high sticky coefficient can stimulate the surface contamination along the time-interval between two consecutive shots.
It would modify the surface SEY and can be a justification for the inability of the system in reaching a low SEY upon an high cumulative dose.
Lastly, the set-up records the RF behavior of the multipacting.
The higher the SEY of the surface, the lower the power threshold to start the multipacting, figure 7.14.
Figure 7.15 represents the conditioning of the surface in terms of the power threshold increase to develop the multipacting.
As the yield of the surface reduces, it requires more power to accelerate the primary electrons and induce the cascade generation of secondaries.
A conditioning campaign lasted usually between 1 and 2 weeks, according the requested level of conditioning.
It's clear that the multipacting isn't suppressed, after 2 weeks of continuous tests are still evident the traces of the electron cloud development.
The tendency to multipacting is strongly decreased, as the typical correlated phenomena like the pressure increase, but the system appears unable to suppress completely the multipacting by scrubbing.

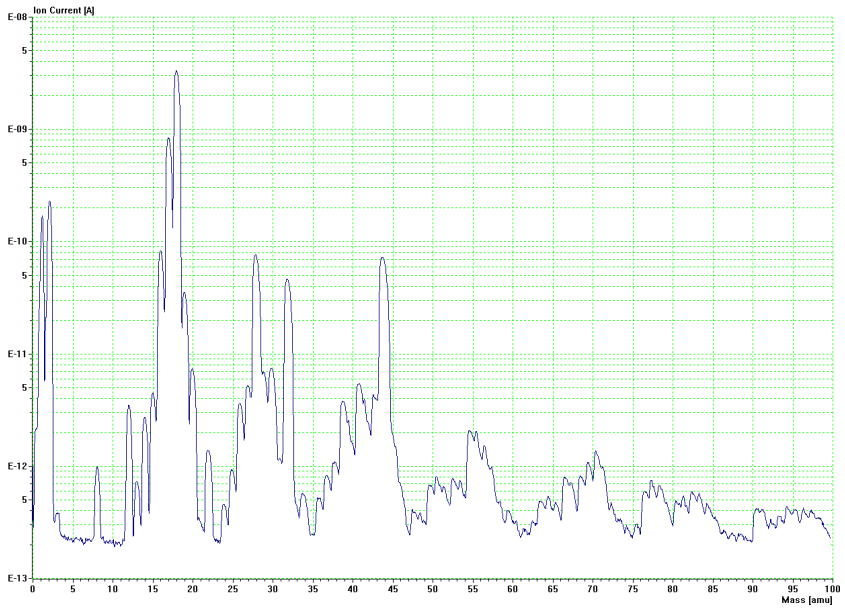

Figure 7.13: MDHW Dipole RGA scan of an unconditioned *StSt* liner.

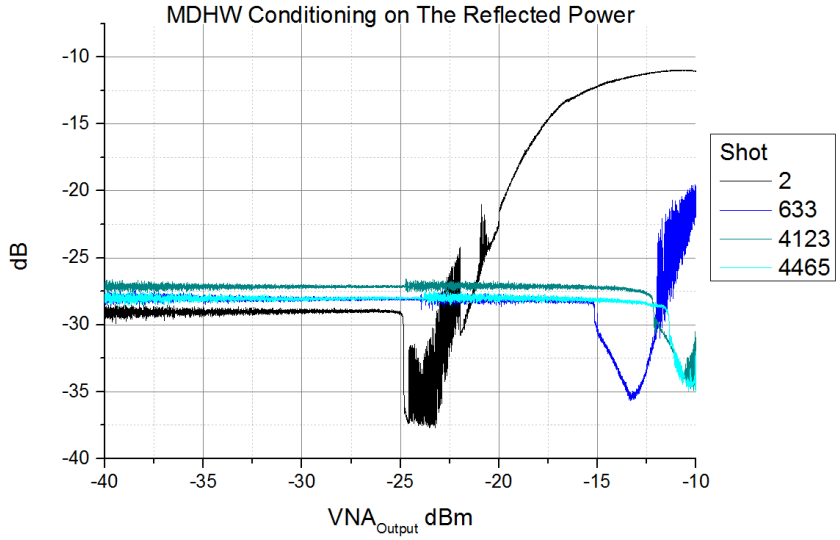

Figure 7.14: The surface conditioning increases the power threshold for the activation of the multipacting.

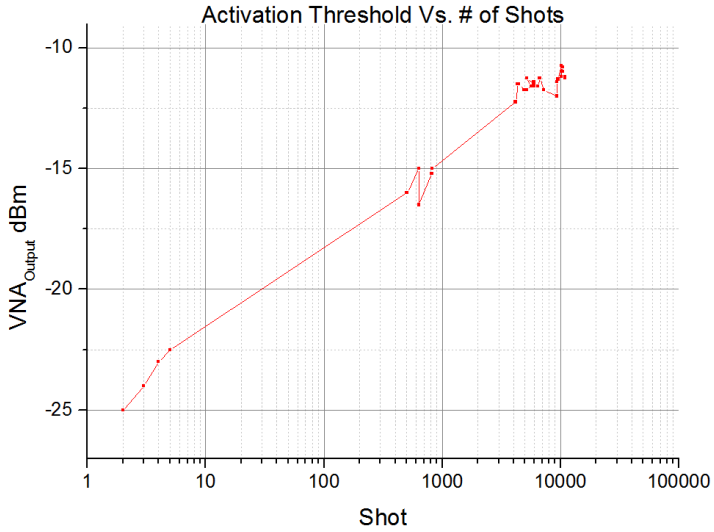

Figure 7.15: The threshold power for the activation of the multipacting increases during the conditioning.

7.4 Accelerated conditioning tests

When the *StSt* liner conditioning reaches the plateau, it becomes hard to push further the reduction of the SEY.
The surface graphitization is a key point in the conditioning, for this reason the test-bench has been provided of an injection line for hydrocarbon gases.
As explained in chapter 4 the idea is the injection of an hydrocarbon gas which electron induced dissociation would lead to an increased surface graphitization.
Therefore, the aim of the test is an acceleration of the conditioning process to get rid of the logarithmic behavior of the *StSt* in vacuum or at least to change its slope.
The tests were performed injecting acetylene, C_2H_2 or dodecane, $C_{12}H_{26}$.
Since the long sojourn time allowed to think in an high probability of electron induced dissociation, the dodecane behavior is extremely significant
In that case, the system was firstly pumped down to $1.6 * 10^{-8} mbar$, then the injection valve has been opened to let the dodecane flow inside the vacuum chamber.
The RGA was used to check the efficient injection of the hydrocarbon gas inside the system, picture 7.16. The most probable heavy cracking patterns are $57amu$, $71amu$ and $85amu$ [34].
Figure 7.16-red line shows the RGA evidences of the dodecane injection: heavy hydrocarbon peaks increase their intensities.
The dodecane, as the acetylene, has been injected at three different pressure to study its effects on the multipacting.
Firstly it has been injected at $10^{-6} mbar$, the conditioning tests proceeded for more than one day showing no accelerations in the conditioning rate, instead it showed a tendency toward a current increase.

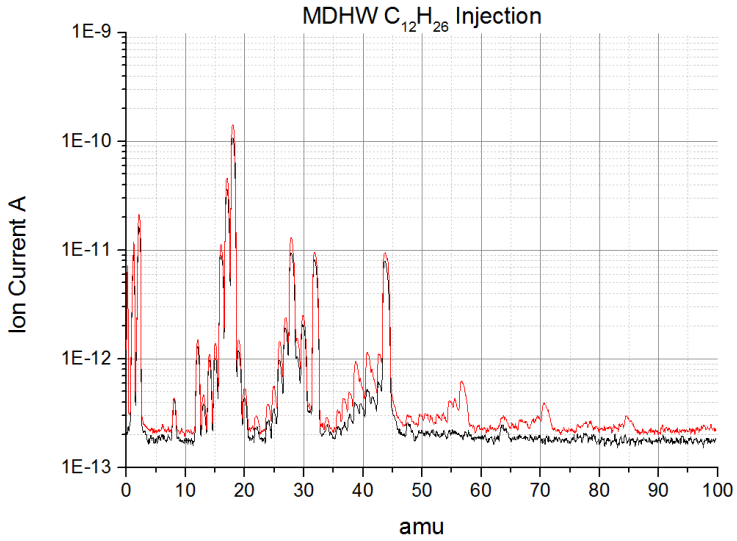

Figure 7.16: The black line represents the RGA spectrum before the dodecane injection, system pressure at $10^{-7}mbar$. The red one is just after the opening of the leak valve, system pressure at $10^{-6}mbar$.

It was decided firstly to reduce the leak pressure to $10^{-7}mbar$, which corresponded to a recover of the conditioning trend toward lower current values.
Finally the valve was opened to increase the pressure system up to $10^{-5}mbar$.
The main effects are an increased maximum current and pressure peaks for the pressures above $10^{-7}mbar$, figure 7.17.
These two phenomena are ascribed even to the plasma formation which affects the system exposed to high pressure gases, it increases either the current and pressure readings, as well as the RF behavior of the system.
The leak valve has been closed after the hydrocarbons tests, nevertheless the conditioning rate appeared not to be influenced by the gas injection.

7.5 C-coated liner

A C coated liner was prepared to compare the multipacting behavior of a surface which $\delta_{max} \simeq 1$ with the $StSt$ liners.
The C has been applied as a central coating strip on the opposite faces of the liner along its whole length, figures 7.18-a and 7.18-b.
The set-up has been prepared in the same manner as before: the VNA ranged between $-40dBm$ and $-10dBm$ and the initial coupling set at $-27dB$.
The working frequency was set at $142.5808MHz$ and the magnetic field at $49G$, below the cyclotron field.
Since the first shots, the liner presented evidences of multipacting either according the pressure and the RF, despite the C strip was supposed to suppress the electron cloud development.

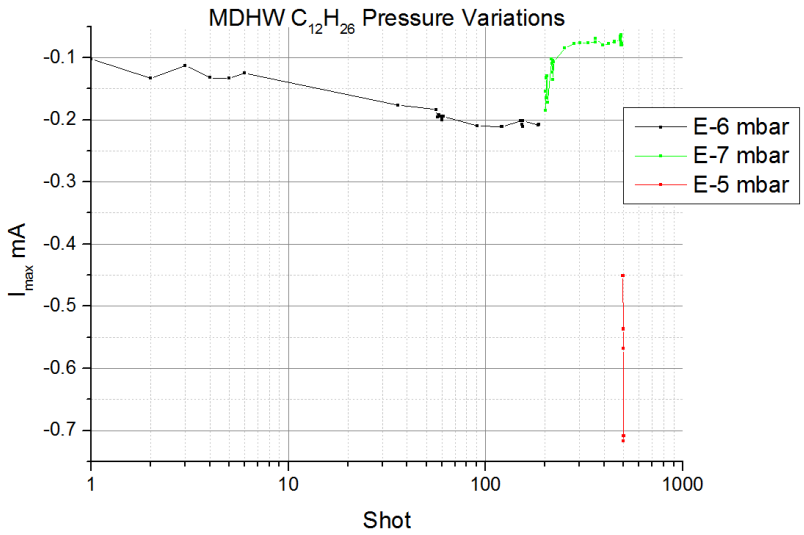

Figure 7.17: The injection of dodecane increases the collected current with its pressure, no evidence of conditioning accelerations have been noticed.

It was taken the decision to start a conditioning campaign of the coated liner, the power shots frequency was set as usual 1 shot every 2 minutes.
Figures 7.19 shows a huge decrease in the multipacting tendency.
The results were compared to what obtained with the *StSt* liner introduced in the sections above: the increase of the power threshold for the activation of the multipacting is faster during the first shots, figure 7.21.
The conditioning of the *C*-coated liner appears stronger than the ultimate conditioning obtained on the *StSt* one, moreover this level is reached much faster, figure 7.22
Along the first part of the experiments on the *C*-coated liner, the system behaved surprisingly showing multipacting when was unexpected.
The conditioning tests showed a faster conditioning trend for the coated liner, but an extremely interesting point is the complete lack of current readings since the beginning of the measurements.
The electron cloud monitor has been tested and showed no short-circuits or reasons for not being able of acquiring the multipacting current.
The lack of current was firstly ascribed to a weak electron cloud, so weak to be not detectable.
The sensitivity of the DAQ is directly proportional to the value of its resistors, it was decided to increase their value up to $R_{DAQ} = 100k\Omega$.
On one hand it increases the sensitivity of the DAQ, on the other increases the noise which can cover the weakest signals.
Nevertheless no currents signals were detected after the resistors value increase 7.23.
Since no currents were registered at higher sensitivity, it was wondered whether the multipacting developed out of the electron cloud monitor window.

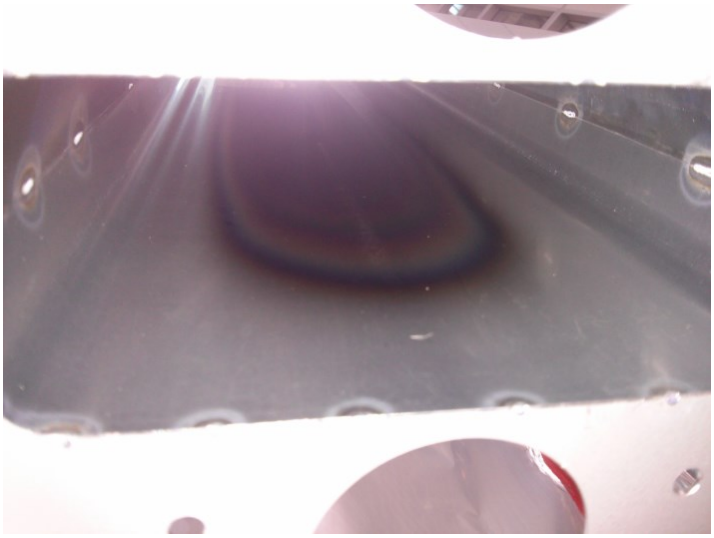

(a) MDHW Dipole C coated liner inside

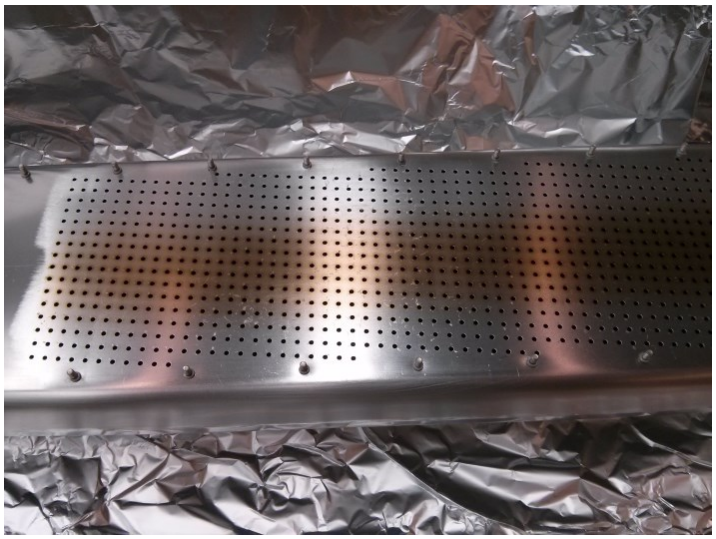

(b) MDHW Dipole C coated liner outside

Figure 7.18: a:Inside view of the liner C coating. b:External prospective of the coated liner.

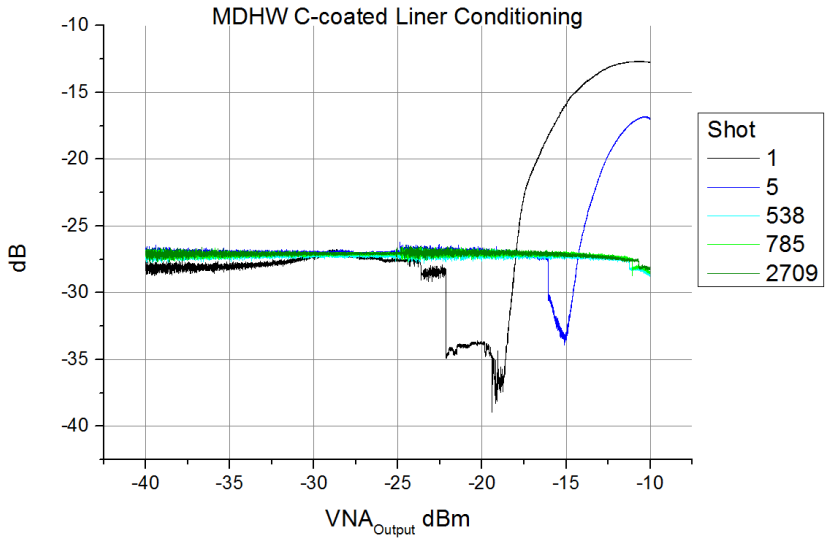

Figure 7.19: The C coated liner conditioning campaign: RF behavior.

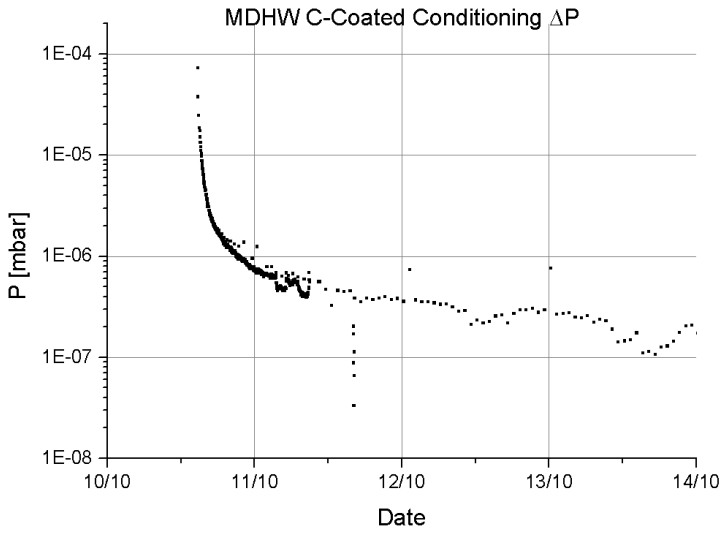

Figure 7.20: The C coated liner conditioning campaign: ΔP behavior, before leak valve opening.

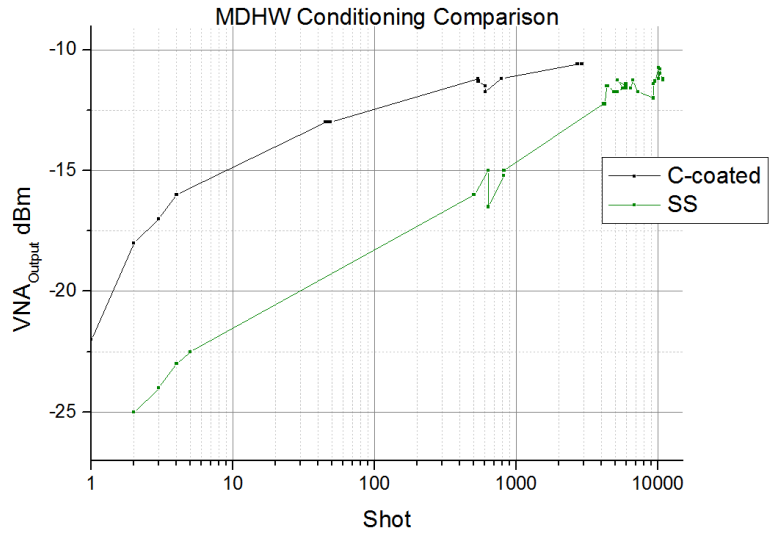

Figure 7.21: Comparison on the conditioning behavior according the power threshold for the activation of multipacting. The black line is the C liner. The red line the $StSt$ one.

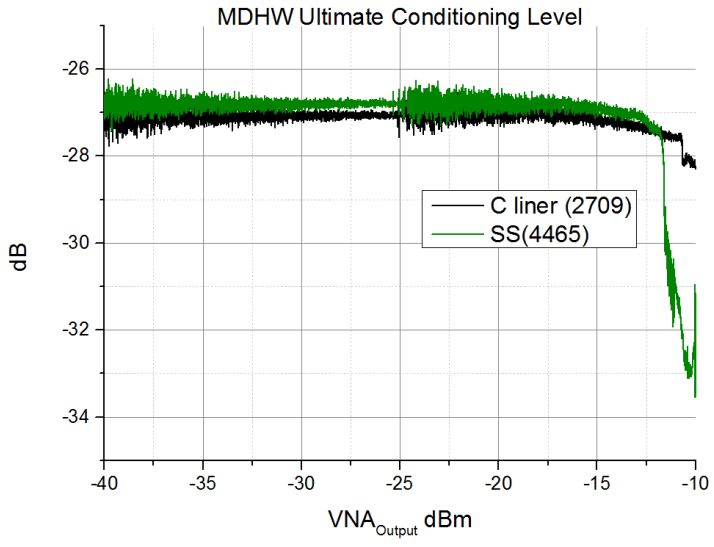

Figure 7.22: The numbers withing brackets are the number of cycles necessary to reach the present conditioning level.

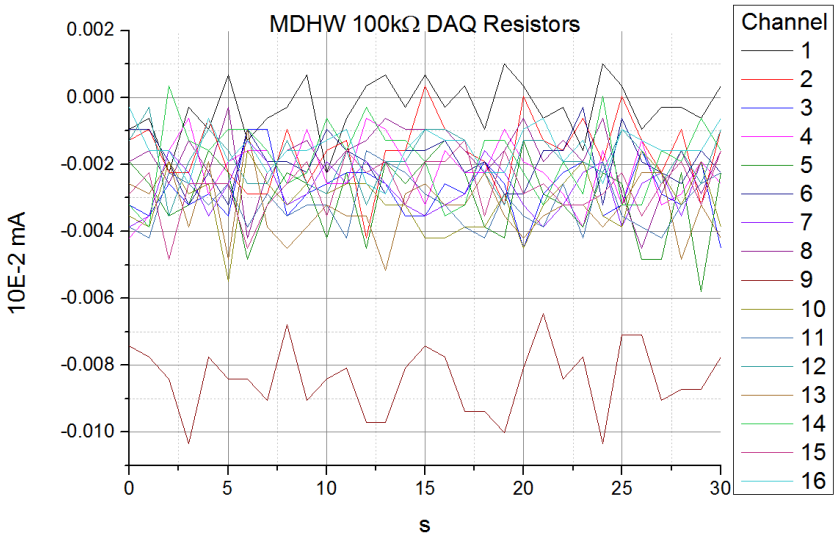

Figure 7.23: The current readings are null even after the resistors value increase.The offset of channel 8 is due to its background noise.

The RF and pressure readings were able to detect the system variations linked to electron cloud, but no electrons escaped through the holes of the liner and no currents were detected.
So, it was wondered whether it was happening outside the magnetic field region, so outside the test-bench main chamber.
Some tests at different magnetic field were performed to clarify these hypotheses.
Figure 7.24 presents the ineffectiveness of the magnetic field variations on the multipacting behavior inside the system.
Such behavior supports the second thesis: the multipacting develops outside the magnetic field region.
To go deeper in this suppositions, the leak valve was opened and the system was filled with dodecane.
In the sections above it was shown that the multipacting strength appears to increase with the gas pressure, in fact the current readings are highly increased after the leak valve opening.
In this case, the VNA reading appear to be highly influenced by the $C_{12}H_{26}$, figure 7.25, but still no current readings are detected.
The leak valve has been initially set to reach a gas pressure in the order of $10^{-7}mbar$, after one night the overall pressure of the system increased up to $10^{-6}mbar$, without any further opening of the leak valve.
This behavior is thought to be ascribed to a saturation of the monitor's kapton sheet.
At the beginning the the pumping speed of the system,S_{TOT}, was $S_{TOT} = S_{pump} + S_{kapton}$, as the monitor sheet got saturated, the pumping speed of the system became $S_{TOT} = S_{pump} + 0$.
As the pumping speed reduced, the gas pressure rose, figure 7.26.

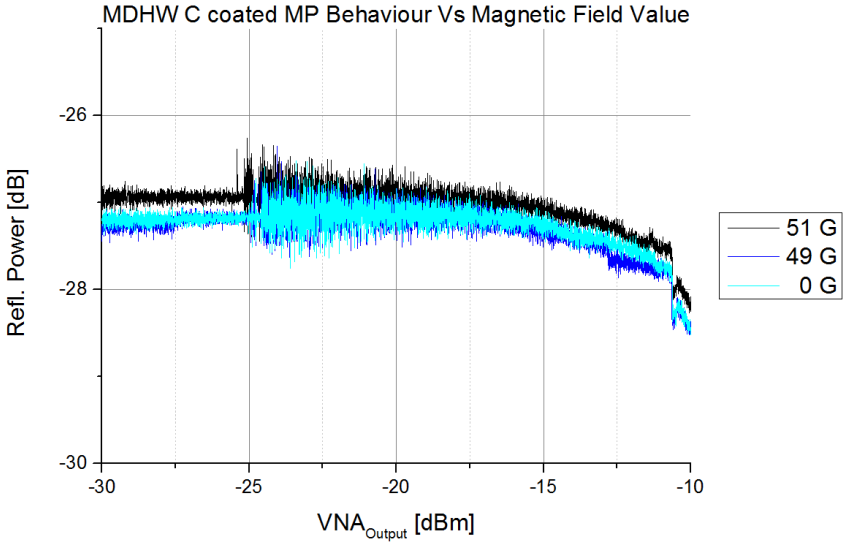

Figure 7.24: The magnetic field has no influence on the multipacting.

Since the multipacting manifested clearly as in the previous experiments on the $StSt$, but no currents were recorded, the maximum power output of the VNA was increased step by step up to $VNA_{Output} = +10dBm$.
The aim was to reach the plasma ignition.
The area where the plasma generates should represent a section of the system where a surface is more prone to electron emission.
The plasma was generated inside the pre-chamber, so outside the electron cloud monitor window and the magnetic field region.
The aim of this experiment was the comparison of the multipacting behavior of a liner which $\delta_{max} \simeq 1$ with the results obtained on the $StSt$ liners to have a clue about the SEY reached on a $StSt$ liner after a conditioning campaign.
This means that, with the present setup and the present power available, we can only conclude that the SEY threshold for multipacting is somewhere above 1, but cannot be better identified.
As a consequence, the conditioning experiment on the uncoated liner, which showed multipacting even after prolonged conditioning, only demonstrates that the SEY was still above 1. As a consequence of the electron cloud development of the liner, figure 7.27, the pressure readings and the VNA data couldn't have been used as comparison terms.
In the previous tests the influence of the surfaces outside of the liner was neglected since the pre-chamber surface is much less prone to develop the multipacting, because of its geometry and the lack of the magnetic field.
Nevertheless, for the future experiments it is foreseen to C coat the pre-chamber, to avoid any influence whenever the liner surface would be conditioned enough to completely suppress the multipacting.

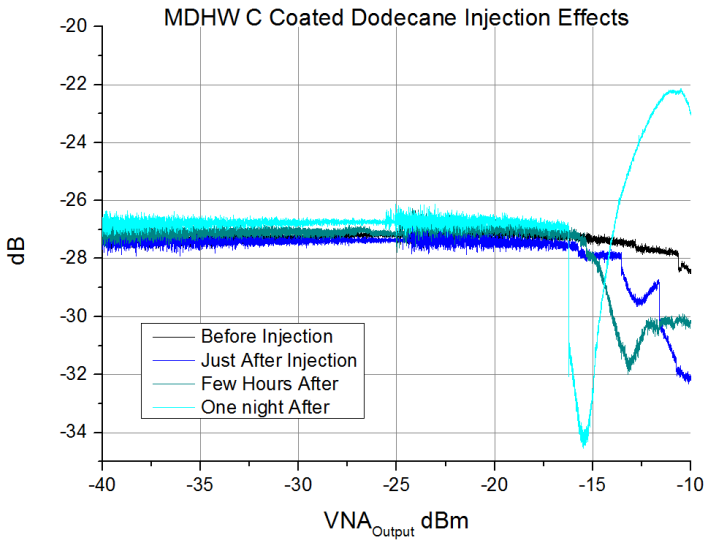

Figure 7.25: The RF behavior shows an increase of the multipacting strength along time after the $C_{12}H_{26}$s injection.

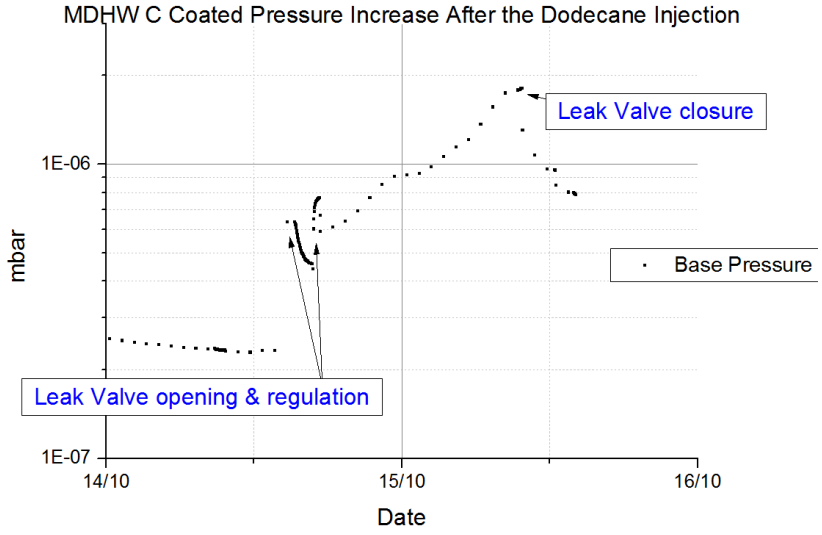

Figure 7.26: The system pressure increased along time because of the saturation of the kapton sheet.

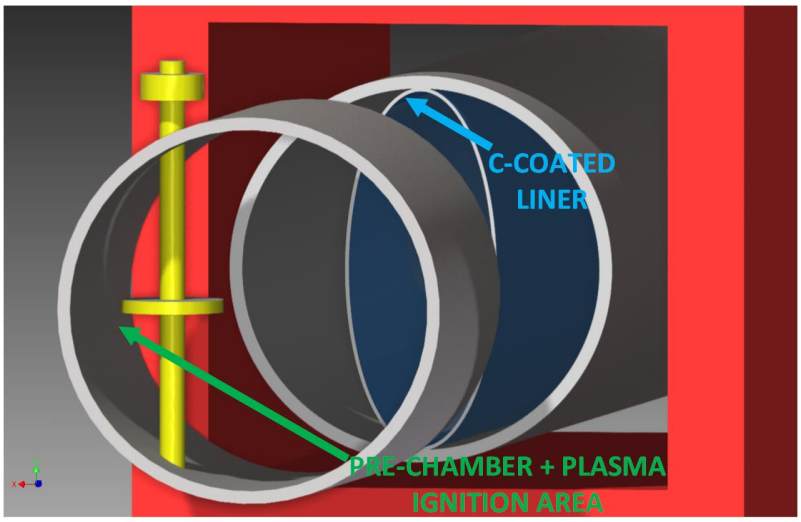

Figure 7.27: The schematic drawing illustrates the zone of plasma generation: outside the C coated liner and so either outside of the magnetic field region and the electron cloud monitor window.

7.6 The influence of the pressure

The test-bench injection line has been connected to an Ar source.
The aim of injecting an inert gas is the study of the pressure effect on the multipacting.
More in detail, to clarify the influence of a plasma generation on the RF behavior of the resonator.
In any conditioning campaign the system showed the tendency to ignite a plasma during the first power shots, when the ESD pressure peaks where high enough, in a range above high $10^{-6}mbar$.
The plasma ignition affects the RF behavior of the multipacting in the VNA readings, furthermore the ionization processes involved in the plasma generation can affect the current readings on the electron cloud monitor.
A $StSt$ liner has been installed in the MDHW dipole test-bench and a conditioning campaign started to reduce the liner SEY before the Ar injection.
The inert gas should not bind to the liner surface, it means that the δ_{max} is not affected by the injection.
During the conditioning, the base pressure of the system reduced from high $10^{-7}mbar$ to low $10^{-8}mbar$ thanks to ESD cleaning of the surface.
A cleaned surface with a low SEY doesn't develop a plasma inside the system.
This condition was attained to compare the RF and current behaviors of a surface in absence (after the conditioning campaign) and in presence of a plasma.
So, only after one week conditioning the Ar valve has been opened.
The Ar injection followed three steps: a first injection at $10^{-7}mbar$, a second increase to 10^{-6} mbar and a final trial at $10^{-5}mbar$.
Only starting from the injection at $10^{-}5mbar$, the multipacting appeared to be influenced by the higher pressure with a relevant increase in the electron cloud

current and a very slight reduction of the VNA_{Output} power threshold for the activation of the multipacting, pictures 7.29 and 7.28.

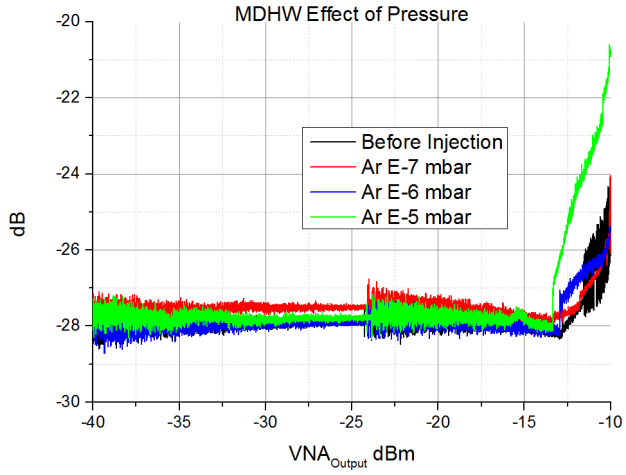

Figure 7.28: The plots illustrate the effect of the injection of an inert gas on the RF behavior of the test bench. Above $10^{-5}mbar$ the pressure is high enough to stimulate a plasma and strongly affect the VNA reading.

On the other hand no strong increase in the ESD pressure peaks has been registered, as the surface has been unaffected by the inert gas, figure 7.30.
When the Ar pressure was at $10^{-5}mbar$, it was visible the plasma ignition.
Trough the figures 7.31 and 7.29 is possible to compare the RF behavior of the $StSt$ liner before conditioning, where the plasma is induced by the release of the dsorbates, and response of the conditioned liner at different Ar pressures.
The goal is to observe whether the degassed residues can have an influence on the initial measurement on the fresh liner.
The unconditioned surface, rich of adsorbants, has an high SEY.
The plasma develops a space charge which affects the RF behavior of the VNA.
Comparing the power threshold for the detuning, its clear how to ignite a plasma with a conditioned liner in high pressure Ar requires more power than the plasma ignition and the multipacting activation with an unconditioned liner in vacuum.
This difference is ascribed to the δ_{max} value of the surface.
It is possible to conclude that the most relevant RF quantity for the detection of the multipacting is the power threshold to its activation.
These statements appears very sensible as they means that once the SEY of a surface is reduced, for the same pressure, it is required more energy to ignite a plasma.

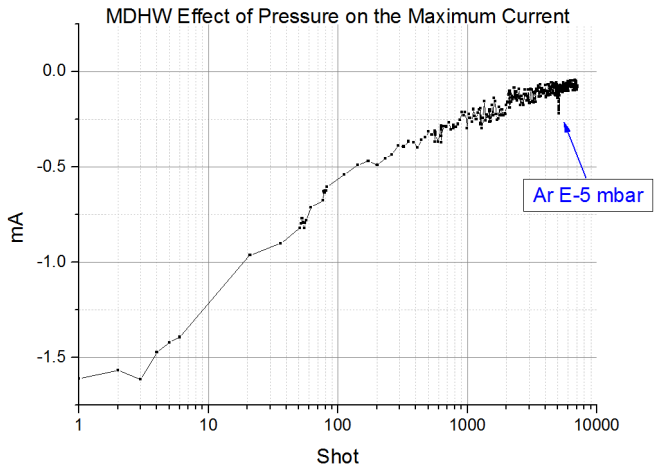

Figure 7.29: The current readings are strongly affected by the Ar injection at $10^{-5}mbar$. This current increase is due to the plasma formation. The ionization events contribute in generating electrons extracted from the liner.

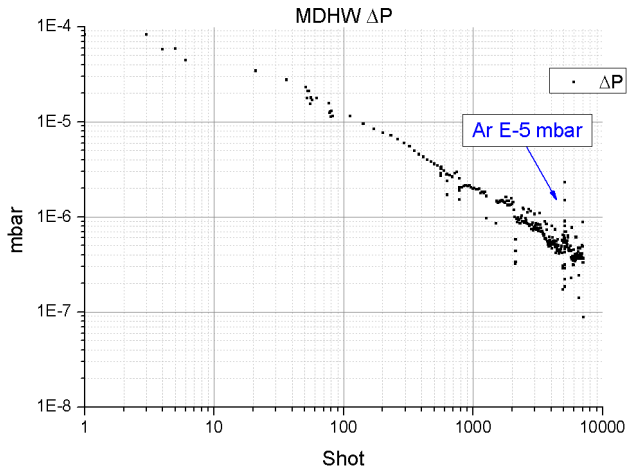

Figure 7.30: The figure introduces the trend of the ESD pressure peaks along conditioning and after the Ar injection. Going further with the surface conditioning the peaks decrease. The ESD is expressed as the difference between the maximum pressure reached during a shot minus the base pressure of the system, $\Delta P = P_{max} - P_{base}$.

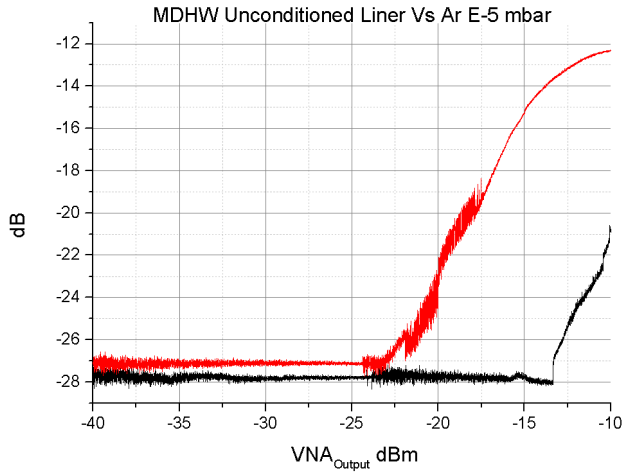

Figure 7.31: MDHW test-bench RF behavior of the unconditioned liner and in Ar. The red line is the RF detuning of an unconditioned liner, high SEY. The black line is the conditioned liner in Ar at $10^{-5}mbar$, lower SEY.

Chapter 8

Conclusions and Outlooks

The present work focused on the problematics concerning the multipacting and the electron cloud development inside vacuum chambers.
The experimental set-up has been updated along the experiments to investigate the different aspects correlated to the cascade generation of secondary electrons: the RF detuning, the electron cloud monitor current and the ESD.
Especially, it was studied the surface conditioning as a possible solution against the e-cloud development inside accelerators.
Conditioning campaigns have been performed on $StSt$ and C coated vacuum chambers.
The results remark a reduction of the tendency toward multipacting on conditioned surfaces.
It means an increase of the power to start the multipacting, a reduction of the electron cloud current and of the ESD pressure peaks.
More in detail, the $StSt$ surfaces conditioning showed a logarithmic-like behavior in the reduction of the electron cloud current.
It allows to conclude the multipacting conditioning would require an unacceptable time to reduce the SEY of its surfaces below the minimum value required to completely suppress it.
Consequently, the RF, the electron cloud monitor and the pressure gauge revealed the presence of multipacting even upon the high electron dose received from the surface along the conditioning: above $10^{-1}C\ mm^2$.
This behavior appears strange if compared to the results obtained with the electron gun conditioning test, which is able to obtain a value $\delta_{max} < 1,3$ for the same dose.
The main difference between the present set-up and the electron gun lays in the electrons current: the gun shots a constant electron flux, which conditioning ability remains constant in time.
Along the conditioning, instead, the electrons extracted from the multipacting decrease as the electron flux on the surface.
On the other hand, the trials performed on the C coated liner confirmed the thin film efficiency.
The experiments concerning the accelerated conditioning showed the inefficiency of this method with both the acetylene, C_2H_2 , and the dodecane, $C_{12}H_{26}$.
This result is not in contrast with the principle behind these tests: the hydrocarbon

decomposition on the surface.
The data acquired don't show any acceleration of the conditioning rate, on the other hand is not possible to argue that nothing has been deposited.
It is sensible that a polymer or an H-rich carbon film deposited on the surface, which SEY is usually higher than the graphite.
As a consequence, the RF and the current readings could not mark any conditioning acceleration.
The present set-up has three main limitations in order to draw conclusions from the experiments that adapt on the SPS accelerator.
First, it is unknown the energy distribution of the electrons inside the chamber.
It is not possible to say whether it is the same produced by the beam induced multipacting.
So, for the same conditions, it is unknown whether it is required the same electrons dose to suppress the multipacting.
The same hypothesis can be applied on the accelerated conditioning efficiency: the electron dissociation cross section is a narrow bell curve, it is not sufficient to have a huge number of adsorbates to induce the graphitization. It is even necessary to have the right electrons energy.
Second, the vacuum level and quality.
The presence of a different residual gas composition modifies the surface adsorbates species, which influence the SEY.
Moreover, the conditioning tests have been performed with a rate of $1shot/120s$, with a system pressure usually one order of magnitude higher than the vacuum level inside the SPS.
These conditions would lead to the formation of an adsorption layer between two consecutive shots, inducing a modification of the surface SEY dependent on the dominant species of the residual gas.
The beam conditioning would develop the multipacting with a much higher rate at lower pressure, limiting the formation of an adsorbate layer.
Lastly, The impossibility of knowing in real time the SEY value of the surface limits the knowledge about the reached conditioning level.
Particularly critic is the lack of knowledge about the SEY limit to suppress the multipacting in the experimental system.
The MBB geometry allows to assume the same $\delta_{max} = 1,3$ limit as for the SPS, but the different working conditions concerning quantities as the power input inside the system can modify this value.
To overcome the last limiting factor, it is necessary to compare the present results with a liner of $\delta_{max} \simeq 1.3$, only in this case it would be possible to have an approximative estimation of the conditioning level reached along the experiments.
In the next future the test-bench will be updated further.
The first trials will involve a Cu coated liner.
Then, a new coating system will be implemented to try a C coating with the injection of H during the sputtering process.
It is known the H affects the properties of a graphite coating, the presence of hydrogen shifts the percentage of sp^3 hybridization atoms toward an higher level.
It will result in a more "diamond-like" carbon coating, since $\delta_{max,DLC} > \delta_{max,graphite}$ it is possible to study the feasibility of a C coating of a priori defined $SEY > 1$

and its effects on the multipacting.
Lastly, it is imminent the introduction of a liner with an electron energy detector. The project foresees the cutting of a small grid on the surface opposite to the holes for the electron cloud monitor.
Since the addition of another electrons extraction area could locally kill the multipacting, it is necessary to balance on the opposite side closing some of the holes which face the e-cloud monitor, figure 8.1.

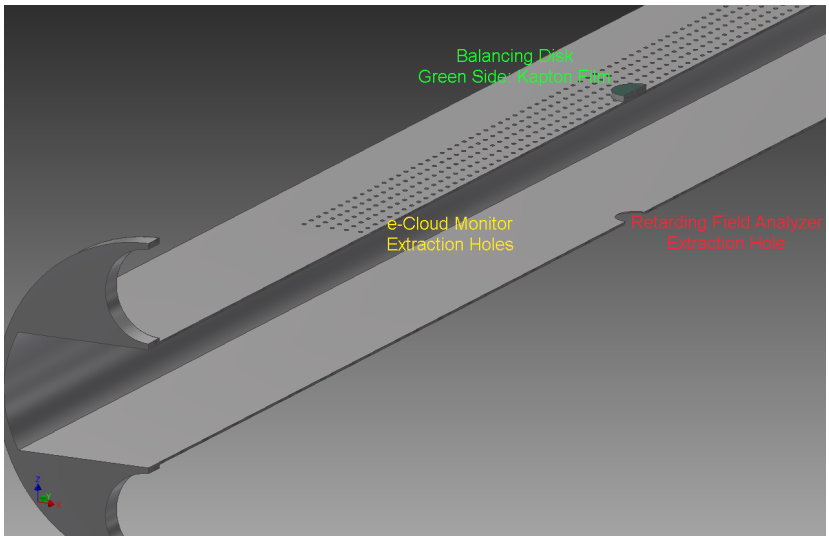

Figure 8.1: The drawing illustrates the project of the liner provided of the electron energy analyzer.

This task will be accomplished by a disk installed on the electron-cloud monitor holes.
It will be made of $StSt$ and installed on the side exposed to the electron cloud, it will be covered by an insulating material on the side exposed to the Cu stripes of the monitor, for example a Kapton film.
The aim of the $StSt$ side is to provide a material with the same SEY of the liner exposed to the multipacting.
The insulating coating, instead, is necessary to prevent any short-circuit between the monitor strips.
The energy detector will be a Semion® retarding field analyzer.
It is made by a small surface positively biased, it can collect the electrons and return their energy and flux.
It would allow to measure the curve of the secondaries energy distribution.
The knowledge of this factor could improve the forecasts on the times required for the surface conditioning and to find the gas with the best electron impact ionization cross section for the accelerated conditioning.
A further update of the set-up will include the addition of a negative DC potential to the W wire.
The goal is providing a fundamental energy to the electrons impinging on the surface to study its effects on the conditioning rate.

Bibliography

[1] Gianluigi Arduini, J M Jimnez, and K Weiss. The sps as a vacuum test bench for the electron cloud studies with lhc type beams. (LHC-Project-Report-490):4 p, Aug 2001.

[2] Phaedon Avouris and Robert E. Walkup. Fundamental mechanisms of desorption and fragmentation induced by electronic transitions at surfaces. 1989.

[3] V Baglin, J Bojko, Oswald Grbner, Bernard Henrist, Nol Hilleret, C Scheuerlein, and M Taborelli. The secondary electron yield of technical materials and its variation with surface treatments. (LHC-Project-Report-433. CERN-LHC-Project-Report-433):6 p, Sep 2000.

[4] E. M. BARODY. A theory of secondary electron emission from metals. In *PHYSICAL REV. VOL. 78, NUMBER 6, JUNE*, 1950.

[5] Matthias Batzill and Ulrike Diebold. The surface and materials science of tin oxide. *Progress in Surface Science*, 79(24):47 – 154, 2005.

[6] C Benvenuti. Non-evaporable getters : from pumping strips to thin film coatings. 1998.

[7] Bruining. *Physics and applications of secondary electron emission*. New York : McGraw-Hill Book Co., 1954, 1954.

[8] R.F. Bunney. Review of literature: Secondary electron emission. 1964.

[9] Friedhelm Caspers, G Rumolo, Walter Scandale, and F Zimmermann. Beam-induced multipactoring and electron-cloud effects in particle accelerators. Technical Report CERN-BE-2009-005, CERN, Geneva, Jan 2009.

[10] A.D. Chew. Mechanical vacuum pumps. May 2006.

[11] P. Chiggiato and P. Costa Pinto. Tizrv non-evaporable getter films: From development to large scale production for the large hadron collider. *Thin Solid Films*, 515(2):382 – 388, 2006.

[12] R. Cimino, M. Commisso, D. R. Grosso, T. Demma, V. Baglin, R. Flammini, and R. Larciprete. Nature of the decrease of the secondary-electron yield by electron bombardment and its energy dependence. *Phys. Rev. Lett.*, 109:064801, Aug 2012.

[13] P Costa Pinto, S Calatroni, P Chiggiato, P Edwards, M Mensi, H Neupert, M Taborelli, and C Yin-Vallgren. Carbon coating of the sps dipole chambers. *CERN Yellow Report CERN-2013-002, pp.141-148*, (arXiv:1308.1305):7 p, Aug 2013. Comments: 7 pages, contribution to the Joint INFN-CERN-EuCARD-AccNet Workshop on Electron-Cloud Effects: ECLOUD'12; 5-9 Jun 2012, La Biodola, Isola d'Elba, Italy; CERN Yellow Report CERN-2013-002, pp.141-148.

[14] P Costa Pinto, S Calatroni, P Chiggiato, H Neupert, E N Shaposhnikova, M Taborelli, W Vollenberg, and C Yin Vallgren. Thin film coatings for suppressing electron multipacting in particle accelerators. 2011.

[15] A.J. Dekker. Secondary electron emission. In Frederick Seitz and David Turnbull, editors, *Advances in Research and Applications*, volume 6 of *Solid State Physics*, pages 251 – 311. Academic Press, 1958.

[16] Matthew P Dewar. Characterization and evaluation of aged stainless steels, Jan 28, 2013.

[17] Andrew J. Gellman and Kris R. Paserba. Kinetics and mechanism of oligomer desorption from surfaces: n-alkanes on graphite. *The Journal of Physical Chemistry B*, 106(51):13231–13241, 2002.

[18] Oswald Grbner. Beam induced multipacting. (LHC-Project-Report-127. CERN-LHC-Project-Report-127):4 p, Jul 1997.

[19] Hasan. New stopping power formula for intermediate energy electrons. *Applied Radiation and Isotopes*, 66(12):1886 – 1890, 2008.

[20] Bernard Henrist, Noel Hilleret, C Scheuerlein, M Taborelli, and G Vorlaufer. The variation of the secondary electron yield and of the desorption yield of copper under electron bombardment: Origin and impact on the conditioning of the lhc. (LHC-Project-Report-583. CERN-LHC-Project-Report-583):4 p, Jul 2002.

[21] Siegfried Hofmann. *Auger- and X-ray photoelectron spectroscopy in materials science: a user-oriented guide*. Springer series in surface sciences. Springer, Heidelberg, 2013.

[22] Jeromy Hollenshead and Leonard Klebanoff. Modeling radiation-induced carbon contamination of extreme ultraviolet optics. *Journal of Vacuum Science & Technology B*, 24(1):64–82, 2006.

[23] Michael Holz and Friedhelm Caspers. Experimental investigation of multipacting suppression by amorphous carbon coatings, 2012.

[24] http://physics.nist.gov/cgi bin/Ionization/graph$_n$ew.pl?element=C2H2.0.

[25] G Iadarola, G Arduini, V Baglin, H Bartosik, JE Esteban Muller, G Rumolo, E Shaposhnikova, L Tavian, F Zimmermann, O Dominguez, and GHI Maury Cuna. Electron cloud and scrubbing studies for the lhc. Technical Report CERN-ACC-2013-0054, CERN, Geneva, May 2013.

[26] G Iadarola, H Bartosik, M Driss Mensi, H Neupert, G Rumolo, and M Taborelli. Recent electron cloud studies in the sps. Technical Report CERN-ACC-2013-0115, CERN, Geneva, May 2013.

[27] Stuart T. Jackson and Ralph G. Nuzzo. Determining hybridization differences for amorphous carbon from the {XPS} c 1s envelope. *Applied Surface Science*, 90(2):195 – 203, 1995.

[28] J M Jimenez, Gianluigi Arduini, Paul Collier, G Ferioli, Bernard Henrist, Nol Hilleret, L Jensen, Jean Michel Laurent, K Weiss, and Frank Zimmermann. Electron cloud studies and beam scrubbing effect in the sps. Technical Report LHC-Project-Report-634. CERN-LHC-Project-Report-634, CERN, Geneva, Apr 2003.

[29] K W Kolasinski. *Surface science: foundations of catalysis and nanoscience*. Wiley, New York, NY, 2001.

[30] R Larciprete, D R Grosso, M Commisso, R Flammini, and R Cimino. The chemical origin of sey at technical surfaces. (arXiv:1308.1290):6 p, Aug 2013. Comments: 6 pages, contribution to the Joint INFN-CERN-EuCARD-AccNet Workshop on Electron-Cloud Effects: ECLOUD'12; 5-9 Jun 2012, La Biodola, Isola d'Elba, Italy.

[31] Richard I Masel. *Principles of adsorption and reaction on solid surfaces*. Wiley series in chemical engineering. Wiley, New York, NY, 1996.

[32] I Montero, L Aguilera, F Caspers, M Mensi, and M Taborelli. Reduction of secondary electron yied (sey) figures on smooth metallic surfaces by means of magnetic roughness. Technical Report CERN-ACC-2013-0105, CERN, Geneva, Jul 2013.

[33] A. Mozumder and Y. Hatano. *Charged Particle and Photon Interactions with Matter: Chemical, Physicochemical, and Biological Consequences with Applications*. Taylor & Francis, 2003.

[34] NIST. Nist http://webbook.nist.gov/cgi/cbook.cgi?id=c112403&mask=1eff#thermo-react.

[35] Roger Nix. An introduction to surface chemistry, queen mary university, http://www.chem.qmul.ac.uk/surfaces/scc/. 2013.

[36] Luca Nobili. Course of physical chemical treatments of surfaces, politecnico di milano. 2012.

[37] Luigi Palumbo. *Cern Accelerator School 2005: Space Charge*. 2005.

[38] Kris R. Paserba and Andrew J. Gellman. Kinetics and energetics of oligomer desorption from surfaces. *Phys. Rev. Lett.*, 86:4338–4341, May 2001.

[39] M Pivi. *Beam Induced Electron Multipacting in the CERN Large Hadron Collider Accelerator LHC*. PhD thesis, Turin U., Geneva, 2000. Presented on 23 Jun 2000.

[40] M. Pivi, F. K. King, R. E. Kirby, T. O. Raubenheimer, G. Stupakov, and F. Le Pimpec. Sharp reduction of the secondary electron emission yield from grooved surfaces. *Journal of Applied Physics*, 104(10):–, 2008.

[41] Paul A Redhead, John P Hobson, and Ernest V Kornelsen. *The physical basis of ultrahigh vacuum*. High vacuum series. Chapman and Hall, London, 1968.

[42] J. M. Ripalda, I. Montero, L. Vzquez, D. Raboso, and L. Galn. Secondary electron emission and photoemission studies on surface films of carbon nitride. *Journal of Applied Physics*, 99(4):–, 2006.

[43] J. Robertson. Diamond-like amorphous carbon. *Materials Science and Engineering: R: Reports*, 37(46):129 – 281, 2002.

[44] Mike Bancroft Igor Bello Roger Smart, Stewart McIntyre. X-ray photoelectron spectroscopy, http://mmrc.caltech.edu/ss$_x$ps/xps$_p$pt/xps$_s$lides.pdf.

[45] A Rossi. Sey and electron cloud build-up with neg materials. 2005.

[46] G. Rumolo. Which parts of the sps do we need to coat? http://indico.cern.ch/event/62873/material/slides/0?contribid=2&sessionid=0. 2009.

[47] C Scheuerlein, Nol Hilleret, and M Taborelli. The secondary electron yield of air exposed metal surfaces at the example of niobium. Technical Report CERN-EST-2002-003-SM, CERN, Geneva, Jun 2002.

[48] H Seiler. Secondary electron emission in the scanning electron microscope. *Journal of Applied Physics*, 54(11):R1–R18, 1983.

[49] Pedro Costa Pinto Mauro Taborelli Sergio Calatroni, Paolo Chiggiato. Lhc machine advisory committee meeting no. 23,. 2008.

[50] M Taborelli, J Colaux, P Costa Pinto, S Calatroni, P Chiggiato, P Edwards, D Letant-Delrieux, S Lucas, H Neupert, W Vollenberg, and C Yin-Vallgren. Carbon coatings with low secondary electron yield. Technical Report CERN-ATS-2012-287, CERN, Geneva, Nov 2012.

[51] M Taborelli, J Colaux, P Costa Pinto, S Calatroni, P Chiggiato, P Edwards, D Letant-Delrieux, S Lucas, H Neupert, W Vollenberg, and C Yin-Vallgren. Carbon coatings with low secondary electron yield. Technical Report CERN-ATS-2012-287, CERN, Geneva, Nov 2012.

[52] Thomas Thuillier. Electron cyclotron resonance ion sources - i. 2012.

[53] O. GROBNER B. HENRIST N.HILLERET G. VORLAUFER V. BAGLIN, I. COLLINS. Secondary electron emission : Experimental results and their implications, http://conference.kek.jp/two-stream/hillet.pdf. 2011.

[54] Pfeiffer Vacuum. *Pfeiffer Vacuum Gauge Manual*.

[55] Pfeiffer Vacuum. *Vacuum Technology Know How*.

[56] Yin Vallgren. *Low Secondary Electron Yield Carbon Coatings for Electron Cloud Mitigation in Modern Particle Accelerators*. PhD thesis, Chalmers U. Tech., Goteborg, 2011. Presented 13 Sep 2011.

[57] L Vos. Analysis of electron cloud. Technical Report CERN-AB-2003-074-ABP, CERN, Geneva, Jun 2003.

[58] L Wang, T O Raubenheimer, and G Stupakov. Suppression of secondary emission in a magnetic field using triangular and rectangular surfaces. *Nucl. Instrum. Methods Phys. Res., A*, 571(SLAC-PUB-12001):588–598, Feb 2007.

[59] C Yin Vallgren, G Arduini, J Bauche, S Calatroni, P Chiggiato, K Cornelis, P Costa Pinto, B Henrist, E Metral, H Neupert, G Rumolo, E Shaposhnikova, and M Taborelli. Amorphous carbon coatings for the mitigation of electron cloud in the cern super proton synchrotron. *Phys. Rev. Spec. Top. Accel. Beams*, 14(CERN-OPEN-2011-040):071001. 11 p, Jul 2011.